Remote sounding of atmospheric layer motions for site testing and photon propagation properties

Stefano Cavazzani
stefano.cavazzani@unipd.it

Department of Physics and Astronomy
Padova University, Italy

Supervisor: Sergio Ortolani
Advisors: Valentina Zitelli; Cesare Barbieri

Referee: Marc Sarazin

01-01-2014

Contents

INTRODUCTION

This thesis is divided into two main arguments: the first is a satellite study of a planetary atmosphere and the second is a study of the propagation properties of photons in the atmosphere. The study of the atmosphere is made through the analysis of satellite data. The satellites are divided into two main groups: polar satellites and geostationary satellites. Polar satellites have an orbit around the Earth at an altitude of about $800km$, they pass over the same site twice every 24 hours and have a field of view that looks at the entire globe of the Earth. Geostationary satellites orbit above a fixed point at an altitude of about 35000km, they have a temporal resolution of the order of minutes, and they have a field of view of a single hemisphere. For this reason the geostationary systems are composed of a pair of satellites so as to cover the entire globe.
In this thesis the satellite data analysis of Earth's atmosphere has the main purpose of the site testing. We base the analysis on the study of data from the geostationary satellite GOES12. In particular, we describe a new model for a complete study of the Earth's atmosphere. This model studies the cloud cover, but for some selected sites it includes also some indications on atmospheric phenomena such as winds, fog, dust and high humidity. It also allows a short and long term statistical forecast of the observing conditions of the site and a qualitative analysis of the seeing. We correlate the cloud cover data with the data from the MODIS polar satellite. This allows a mutual assessment of the results obtained from the two satellites belonging to the two main satellite groups. The combined analysis of a geostationary satellite and a polar satellite allows us to fill the respective limits of the two satellite groups. In the second part we analyze the photon propagation properties in the free atmosphere: we see in detail how the photon propagation time changes in a medium. We also analyze the geometrical and physical distortions of these photon paths. In particular, we describe a new model for the photon delay time in the atmosphere and to derive the seeing from this delay time fluctuations. Finally, we describe the design of a new tool for the ground layer seeing analysis.

Part I

Remote sounding of atmospheric layer motions

Chapter 1

Satellite model for the cloud cover study

In this chapter we describe the main model on which is based our work. This model has some limitations and fixed assumptions provided by the used satellite characteristics. In the following chapters we will overcome these limitations with integrative models and we will give an experimental verification of the assumptions provided by the satellite characteristics.

Comparing the number of clear nights (cloud free) available for astronomical observations is a critical task because it should be based on homogeneous methodologies. Current data are mainly based on different judgements based on observer logbooks or on different instruments. In this thesis we present a new homogeneous methodology on very different astronomical sites for modern optical astronomy, in order to quantify the available night time fraction. The data are extracted from night time GOES12 satellite infrared images and compared with ground based conditions when available. In this analysis we introduce a wider average matrix and 3-Bands correlation in order to reduce the noise and to distinguish between clear and stable nights. Temporal data are used for the classification.

The efficiency of the astronomical telescopes is critically dependent on the cloud coverage. The knowledge of the clear night time fraction is then fundamental for the choice of a telescope site, and, on already existing facilities, its distribution during the year, as well as long term trends, are very important for planning the observations and the development of the instrumentation. In the last century the quantification of the night time clear fraction was based mainly on specific visual inspection of the sky conditions or on the observational logbooks of the telescopes. These methods are "internally" robust, but they are dependent on the experience of the observer and on the quality of the site. In short time tests there could be also some dependence on the

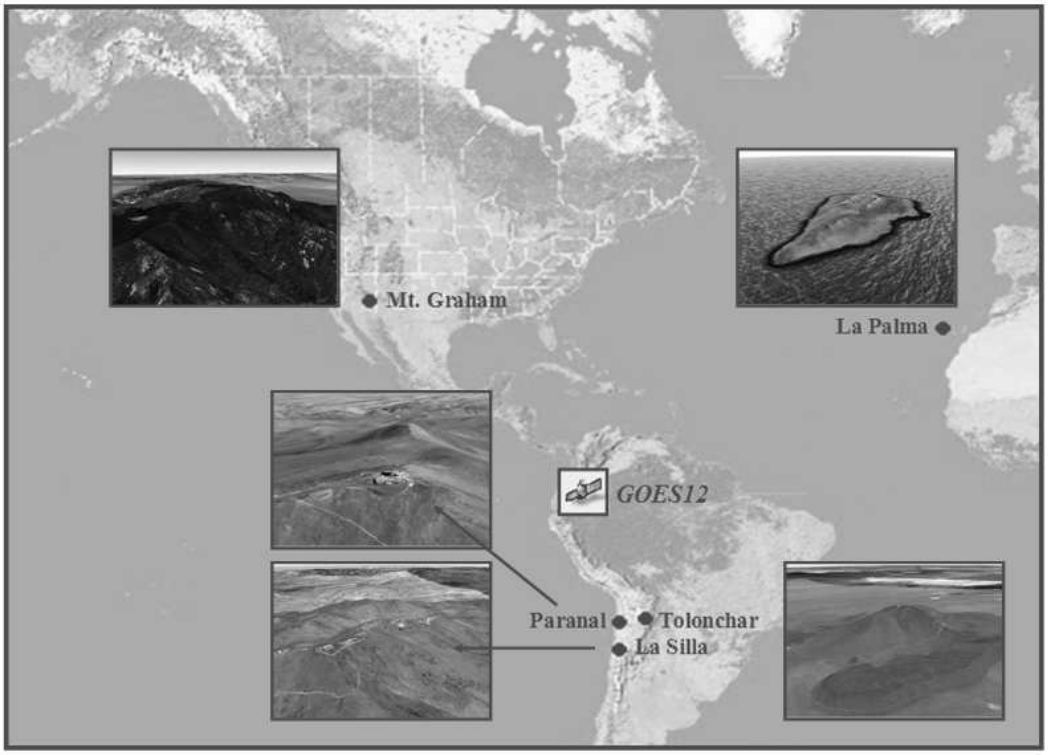

Figure 1.1: Location of the five sites involved in the analysis. As seen in the inserts the selected sites presents very different topographic conditions: La Palma is a sharp island, Mt. Graham a relatively wide plateau, Paranal, Tolonchar and La Silla are isolated peaks over a desertic altopiano. The position of GOES12 satellite projected on the map.

Moon phase. An adequate time coverage is time consuming and expensive when applied to several, new sites. The use of the archives of satellite images allows, instead, to investigate simultaneously several sites in a time base of several years. In this study night time satellite derived parameters are used to assess the clear-usable fraction from the Geostationary Operational Environmental Satellite 12 (GOES12) archive. The selected sites are chosen in order to test different climatic conditions and are located in Chile, USA and Spain (Canary Islands), (See Fig. 1.1).
Most of them are already well known, developed sites and host large, modern telescopes. The site of Tolonchar, instead, have been studied during the Thirty Meter Telescope (TMT) survey, but it is located in relatively little known area for the optical near-infrared astronomy. In this analysis we have a double goal: to check the reliability of our analysis method, to explore the characteristics of new regions and to compare them. The GOES satellite data have been studied with the goal to study environmental conditions, but they have been recently used also for the study of cloud coverage and water vapor content above some astronomical sites (Erasmus & van Rooyen ([2006]), della Valle et al. ([2010]) (PaperIII)). The advantage of GOES over other satellites is to have a very stable and very high orbit, allowing the collection of simultaneous images of almost half of the Earth hemisphere, still with a high resolution (4 km in the infrared (IR)). In this way site to site random biases, due to instrument instabilities are reduced. Furthermore the infrared channels allow the detection of the thermal radiation emitted during the night from different atmospheric layers and/or from the soil. An appropriate choice of the wavelength allows to choose the optimal layer emission height above the site. If it occurs well above the soil surface, the signal becomes independent of the specific soil properties and of low level conditions. Phenomena occurring below the selected site (fog, low clouds...) are also avoided. In some sites, for example at La Palma, this aspect is of crucial importance. The channels used in our analysis have been selected with the above discussed criteria and are summarized in Table 1.1. In a previous paper (Paper III) we studied the clear sky fraction at La Palma and Mt.Graham, from ground and satellite, using an approach similar to Erasmus & van Rooyen ([2006]), but we have used direct GOES12 satellite brightness temperature measurements. In this thesis the descriptions of the adopted definitions used to classify the nights are reported in Sections 4.3 and 4.4.
The new adopted method is validated using the database of La Palma and Paranal and, after the positive results, it is applied to the other sites under investigation.

Table 1.1: GOES12 bands and resolution at Nadir.

	Window	Passband $[\mu m]$	Resolution [km]
BAND1	Visible	$0,55 \div 0.75$	4
BAND2	Microwaves	$3.80 \div 4,00$	4
BAND3	H_2O	$6,50 \div 7.00$	4
BAND4	IR	$10,20 \div 11.20$	4
BAND6	CO_2	13.30	8

1.1 The used database

In this analysis we have used several sets of data collected from ground and satellite facilities partially available via web and partially obtained thanks to the courtesy of the observatory staff. The validation of satellite data are also performed via correlations among ground based and satellite data. In this thesis we have sampled the years 2007 and 2008. Table 1.2 shows the characteristics of the used databases.

1.1.1 Ground based data

Differences at La Palma microclimate have been discussed in the papers (Lombardi et al. ([2006]) (hereafter Paper I), Lombardi et al. ([2007]) (hereafter Paper II), and della Valle et al.([2010]) (Paper III)). Paper I shows a complete analysis of the vertical temperature gradients and their correlation with the astronomical seeing, Paper II shows an analysis of the correlation between wind and astronomical parameters as well as the overall long term weather conditions at La Palma. A statistical fraction of clear nights from satellite has been derived in Paper III using a basic approach to test the ability of the satellite to select clear nights. In order to have a reference for a classification of the nights at La Palma we used three different sources: the logbooks obtained from TNG (Telescopio Nazionale Galileo) and from the Liverpool telescope, and the data from the TNG meteorological station. The logbooks have been used merging the information, filling the gaps and checking the comments in case of contradictory classifications. The data from TNG meteorological station have been used to understand the status of ambiguous or unclassified nights in terms of humidity or wind speed limits. In general the agreement was good, but in winter time all the three sources were often needed in order to have a realistic view of the night weather evolution. The study of the telescope logbooks at Paranal was not needed because the

night status data are obtained from the web pages of the ESO (European Southern Observatory) Observatories Ambient Conditions Database[1]. They are very detailed pages containing the hourly humidity, temperature, atmospheric pressure, direction and wind speed. In addition there are measures of seeing through the DIMM (Differential Image Motion Monitor) and measures of the flux of a reference star. In particular the flux can trace the presence of clouds. The same website is also available for La Silla, but unfortunately in this case the web page is less detailed and often the data are missing. La Silla database is used as a further check. Both the sites of La Palma and Paranal are used to test and validate the new model applied in this thesis.

1.1.2 Satellite based data

In these last decades the site testing have been conducted adding to the traditional meteorological instruments the use of the satellite data. Satellite archives contain several parameters useful for astronomical observations, allowing to compare different sites in a suitable way. Varela et al. ([2008]) give an exhaustive presentation of the satellites used for site testing. In our analysis we have chosen among the other available satellites the GOES satellite because it detects the IR night time emitted radiation. A detailed discussion is presented in Sec. 1.1.2. GOES is an American geosynchronous weather facilities of the National Oceanic and Atmospheric Administration (NOAA), and it is able to observe the full Earth disk. It is designed to detect surface temperature and the cloud cover, in addition to other important meteorological parameters. GOES12 have on board an imager covering five wavelength channels, one in the visible bands and four in the infrared bands (see Table 1.1). The maximum temporal resolution of the full Earth-disk scans is 41 *sec* that is a very high temporal sampling. Moreover GOES have also a high spatial resolution. It should be noticed that GOES12 observed La Palma area at $64°10'$ from Nadir, near the edge of the field of view (Table 1.3).

Advantages of GOES12 Satellite

We preferred to use GOES among the other satellite for several reasons that are explained below:

- Because it is possible to observe, with a single image, several sites simultaneously.
- Because, thanks to the very high orbit ($35800km$), the satellite is extremely stable and not affected by phenomena of high exosphere.

[1]See http://archive.eso.org/asm/ambient-server

Table 1.2: Total amount of consecutive nights covered by each databases.

Site	Ground Data	Satellite Data
Paranal	730	700
La Silla	730	700
La Palma	730	700
Mt.Graham		700
Tolonchar		700

- Because, thanks to this set-up, it is possible to have the same instrumental configuration for each site and to compare them in a suitable way.
- Because GOES12 data have a high temporal resolution (41 sec as maximum value) and the complete day coverage.
- Because GOES12 observe the site at any time of the day. Instead polar satellites are bound to individual orbits. This allows to use an hourly analysis instead of a daily average of atmospheric conditions.
- Because GOES12 data have a high spatial resolution (1 km for visual to 4 km in IR bands).
- Because GOES12 provides five simultaneous images, one for each band, and it is the only satellite with the CO_2 band $(13, 30\mu m)$ very useful for the analysis of lower atmosphere phenomena.
- Because GOES12 have a long term database, useful for long time analysis.
- Because presents the same deterioration of images due to the inevitable degrade of the satellite. As a consequence the comparison between different sites is not influenced by the use of different instruments or different images.

1.2 Satellite data acquisition

For the purposes of this work, we used GOES12 equipped with the imager. Among the 5 available channels, as shown in Table 1.1, we have selected the water vapor channel (channel 3, hereafter called B3 band) centered at 6.7 μm, the cloud coverage channel (channel 4, hereafter called B4 band)

centered at 10.7 μm, and the CO_2 band (channel 6, hereafter called B6 band) centered at 13.3 μm. B3 band is sensitive between $6.5 - 7.0$ μm and is able to detect high altitude cirrus clouds, B4 band is sensitive between $10.2 - 11.2$ μm and is able to detect middle level clouds, while B6 band is able to sense small particle such as fog, ash and semi-transparent high clouds. Data are a measurements of thermal radiation emitted during the night. The selection of the IR channels was done in order to detect clouds at different heights, because water vapor absorbs electromagnetic radiation and then re-emits it in various wavelength bands, in particular in the infrared region at $6 - 7$ μm. If clouds are not present, the emissions at 10.7 μm reaching the satellite is largely not absorbed by the atmosphere so the measured radiance values are due to emission from surface. Instead when clouds are present, the emissivity drops. Data are prepared by the Comprehensive Large Array-data Stewardship System (CLASS), an electronic library of NOAA environmental data[2], and are stored as rectified full earth disk images in a format called AREA files. We processed them using McIDAS-V Version 1.0beta4, a free ware software package. First we extracted the GOES data on the telescope sites.
Table 1.3 shows the geographic coordinates of the analysed sites. For each site we have identified and extracted a sub-image of $1^\circ \times 1^\circ$ having the central pixel centered on (or near) the coordinates given in Table 1.3.
Due to the discrete grid of the available GOES data the distances from the central pixel for each site are: $5' \pm 1'$ at Paranal, $6' \pm 1'$ at La Silla, $5' \pm 1'$ at La Palma, $3' \pm 1'$ at Mt. Graham and $4' \pm 1'$ at Tolonchar. These distances are very small compared to the used matrix.
For each night we have extracted the observations at three different hours: at 02:45, 05:45, 8:45 because they are the local times in common for all sites under investigation available from GOES12 satellite. In case of not availability of the specific images, the nearest temporal image was used. The last column of Table 1.3 shows the satellite view angle. Figure 2.1 shows the two different projections obtained from each acquisition at La Palma and Tolonchar.

In Paper III the analysis of the amount of clear sky fraction at La Palma and Mt.Graham was based following the same approach of Erasmus & van Rooyen ([2006]). We have used the B3 and B4 bands separately to sense thick clouds, but the old procedure presented some limits in case of partial coverage or thin clouds. In this thesis we refine the analysis using a new and more sophisticated channel correlation analysis in order to detect more subtle effects due to atmospheric perturbations, including sudden changes

[2] www.class.ngdc.noaa.gov

Table 1.3: Geographic characteristics of the analyzed sites and GOES12 satellite. The view angle is obtained through the formula $\theta = \sqrt{(\Delta LAT)^2 + (\Delta LONG)^2}$.

site	LAT.	LONG.	Altitude Km	View Angle
Paranal	$-24°37'$	$-70°24'$	2.630	$25°00'$
La Silla	$-29°15'$	$-70°43'$	2.347	$29°30'$
La Palma	$+28°45'$	$-17°52'$	2.363	$64°10'$
Mt.Graham	$+32°42'$	$-109°52'$	3.267	$47°40'$
Tolonchar	$-23°56'$	$-67°58'$	4.480	$24°50'$
GOES12	$+0°00'$	$-75°00'$	35800	

in air masses, which imply changes in seeing, wind and relative humidity. We also included in the analysis the B6 band, see Section 3.3. We believe that these previous limits are overcame by correlating B4 with B3 and B6 bands. Another difference in this new analysis is that the flux is averaged on an area of $1° \times 1°$ instead the 1 pixel value obtaining significant decrease of the instrumental noise. A comparison of the two procedures is described in the following section. This matrix analysis is validated using the GOES 12 data of La Palma and Tolonchar because the two sites show very different geophysical conditions and different satellite angle of view. After the positive validation we decided to extend the same analysis to Paranal, La Silla, and Mt.Graham.

Chapter 2

Resolution correlation matrix

In this chapter we show the characteristics of the matrix used in the model and its advantages. The use of a matrix and consequently the large field of view does not imply a limitation in the spatial resolution. We show that for the astronomical study of the sites the use of matrix is not a limitation but it gives more information about atmospheric conditions. The use of a large field of view is also justified by the observation altitude of the satellite. In section 3.1 we analyze in detail this characteristic of the satellite observation bands. Finally, we were among the first to use a matrix $1^\circ \times 1^\circ$ for astronomical site testing (see Cavazzani et al. ([2010])). At present the use of a large field of view is adopted by major data archives for the testing site.
The histograms of Figures 2.2 and 2.3 show the correlation between the matrix $1^\circ \times 1^\circ$ vs the single pixel at La Palma and Tolonchar in the year 2008 for B4 band. Section 4.1 describes the selected threshold used in this classification.
The grey bar of each histogram represents the data with absolute value $\leq |1\sigma|$ level, black bars show data $> |1\sigma|$ level. Moreover the histogram represents the distribution of the B4 band in altitude. The peak of the histogram corresponds to about $4000m$ at La Palma, and greater than $4000m$ at Tolonchar, see Section 3.1.
The altitude was extrapolated from the B4 weighting function of GOES12 satellite. The peaks of these functions at high altitude and the use of matrix make the model suitable and sensitive for the study of atmospheric layers above the telescope sites. In particular, clouds below the level of the observing site do not affect the model as demonstrated by the high correlation percentage.
In fact the 92% of data at La Palma are within $|1\sigma|$ level, the 96% at Tolonchar. The inset plots of the Figures 2.2 and 2.3 represent the correlation of B4 flux computed as a mean value in a $1^\circ \times 1^\circ$ matrix (black line), and

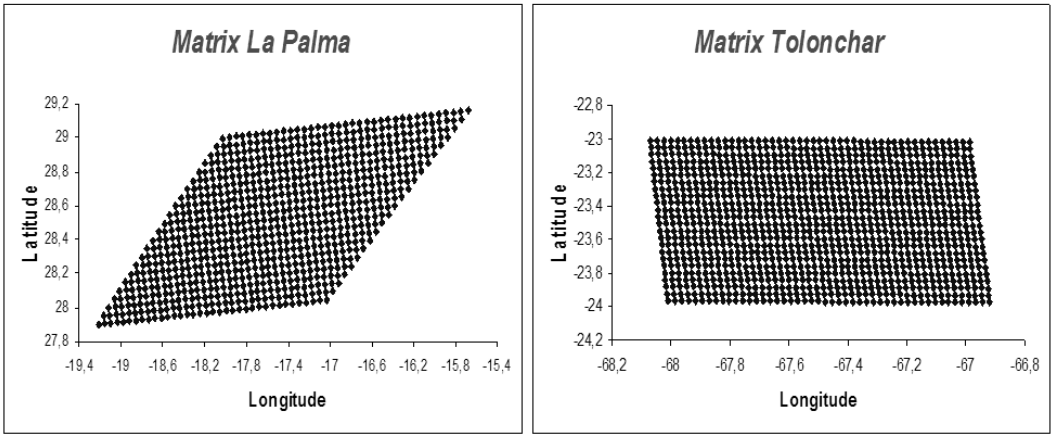

Figure 2.1: Comparison of one image matrix at La Palma and Tolonchar. The deformation is due to the satellite observation angle.

B4 flux obtained in a single pixel (grey line) for March 2008 at Tolonchar and February 2008 at La Palma. February is chosen as a typical perturbed month because of the wide count fluctuations. In each case we see that the mean matrix and 1 pixel values show a similar pattern, this means that we are looking at a high altitude compared to the height site. For the figures we have chosen critical months to show that the correlation is good for any atmospheric condition and then of the season.
We decide to use the matrix, instead the 1 pixel value, because the average of the flux gives more stable information reducing the fluctuations due to instrumental noise. A further advantage in the use of matrix is that we are looking at a wider field of view than in the one-pixel analysis.
We are confident that thanks to the high correlation we obtain statistical reliable data. As shown, the histogram is correlated with the altitude of the site, through the comparison between the matrix and the single pixel we can also extract information on the site analyzed.
La Palma histogram clearly shows an asymmetric distribution showing that perturbations are mainly due to low altitude. A check we done to confirm this point extracting the log comments of data located on the low side of the histogram queue. We found that the majority of the comments are "freezing fog" and data are from winter time.
At Tolonchar the distribution is symmetric and with an almost negligible queue.

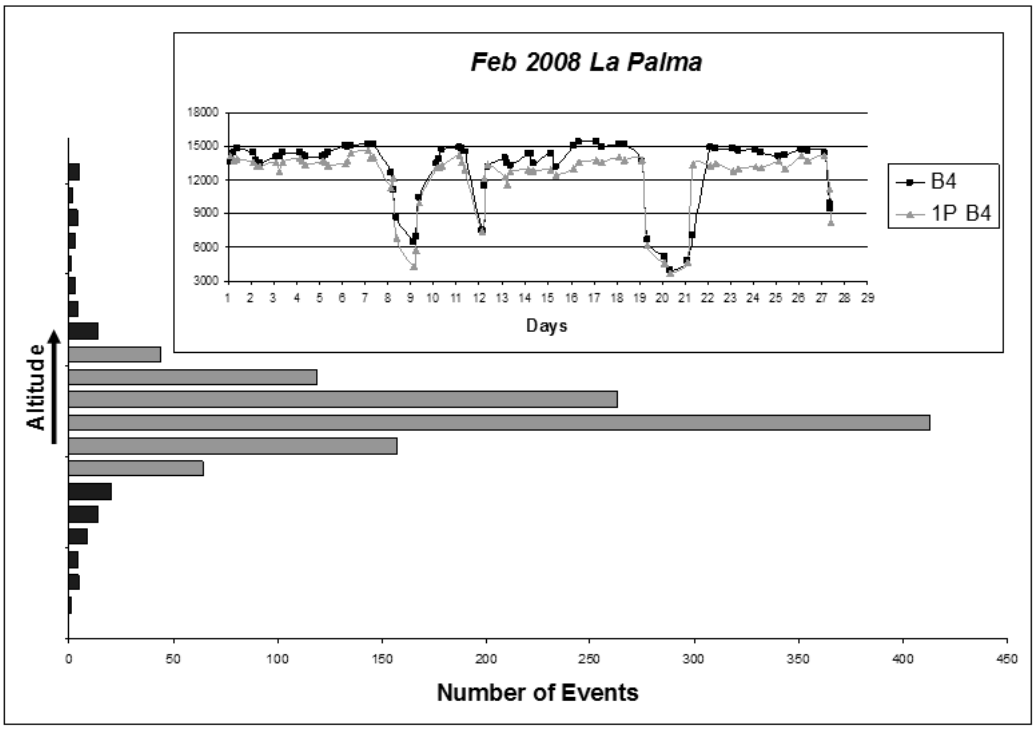

Figure 2.2: Correlation between the Matrix $1° \times 1°$ vs the single pixel. At La Palma in 2008 the histogram shows a correlation of 92%. The gray bars represent the data within the threshold $\leq |1\sigma|$, while black bars are the data with difference $> |1\sigma|$. The upper panel represents a pattern of $1° \times 1°$ matrix (black line) and the single pixel (gray line) in B4 band for a single month. The altitude corresponding to the peak of the histogram corresponds to about $4000m$ as indicated by the B4 weighting function of GOES12 satellite (Bin= $250m$). We note that the main differences arise from low-altitude phenomena.

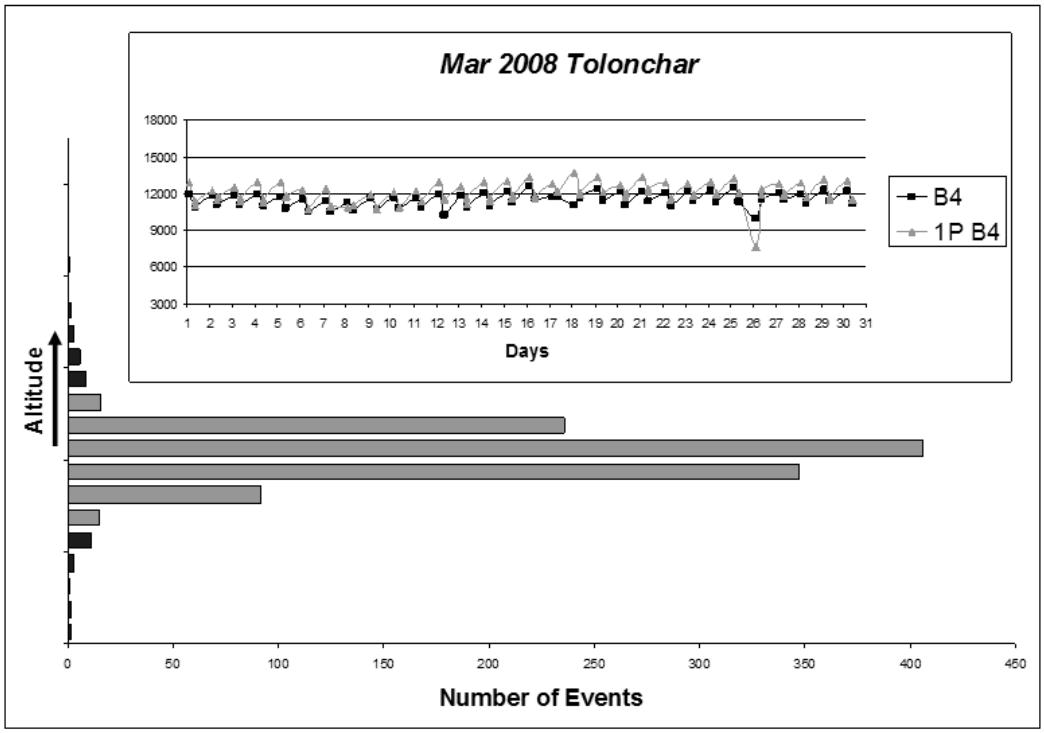

Figure 2.3: Correlation between the Matrix $1^\circ \times 1^\circ$ vs the single pixel. At Tolonchar in 2008 the histogram shows a correlation of 96%. The gray bars represent the data within the threshold $\leq |1\sigma|$, while black bars the data with difference $> |1\sigma|$ (Bin= $250m$). The upper panel represents a pattern of $1^\circ \times 1^\circ$ matrix (black line) and the single pixel (gray line) in B4 band for a single month.

2.1 Intrinsic increase of the spatial-time resolution with the matrix use

In this analysis we used for each site a $1° \times 1°$ matrix, which corresponds to a linear projection of about 100 km. We have shown in Cavazzani et al. ([2010]) that the trend of the mean matrix value is closely correlated with the trend of the single pixel value, with a correlation coefficient of $> 95\%$ for satellite angles of view $< 60°$. The use of the matrix mean value drastically reduces the noise of the images. Figure 2.4 shows that a single pixel (in the small rectangle), $4Km \times 4Km$ wide, does not cover a sufficiently wide sky area above the site because it corresponds to a small geometric field of view as seen from the ground. In fact, the B4 weighting function, obtained using the calibration page[1], observes an atmospheric layer at an altitude of about $4000m$ (see Table 9.2). We emphasize that the B4 band is not able to detect clouds below this altitude, because its weighting function reaches its maximum efficiency at 4 Km, and drops just below this altitude. Clouds below this limit do not directly affect the measurements in this band. This implies that our statistics match more closely on upper limit. The use of the matrix allows to observe the entire sky above the site. In addition, if we have clouds in motion, as in the case of partial cloud coverage, the use of the matrix allows us to observe them.
Furthermore, the use of the single pixel, does not show the temporal cloud evolution giving instantaneous clear time instead of mixed or cloudy time. Figure 2.5 shows the evolution of a partially covered night at Izaña taken on February 7 2008.
We see five images of the island in the B4 band taken at 20:45-23:45-2:45-5:45-8:45 (Local Time). The frame of 20:45 shows Izaña completely cloud free. The second image shows a thick cloud (dashed line) that enters in the matrix field of view moving in the direction of the arrow. The frame taken at 2:45 shows the movement of this cloud. We have estimated the displacement of the cloud to be about 100 km. It comes on top of the analysed site in the next three hours. With a simple calculation we estimated the velocity of this cloud of about $30km/h$.
In conclusion, the use of the matrix combined with the analysis of 5 images for each night gives us a good time resolution. The matrix allows an intrinsic increase of the spatial-time resolution: the matrix observes the temporal evolution of the entire sky above the site. Such temporal resolution and coverage can not, therefore, be reached by the models based on analysis of single pixel and the single image for each night.

[1] http://cimss.ssec.wisc.edu/

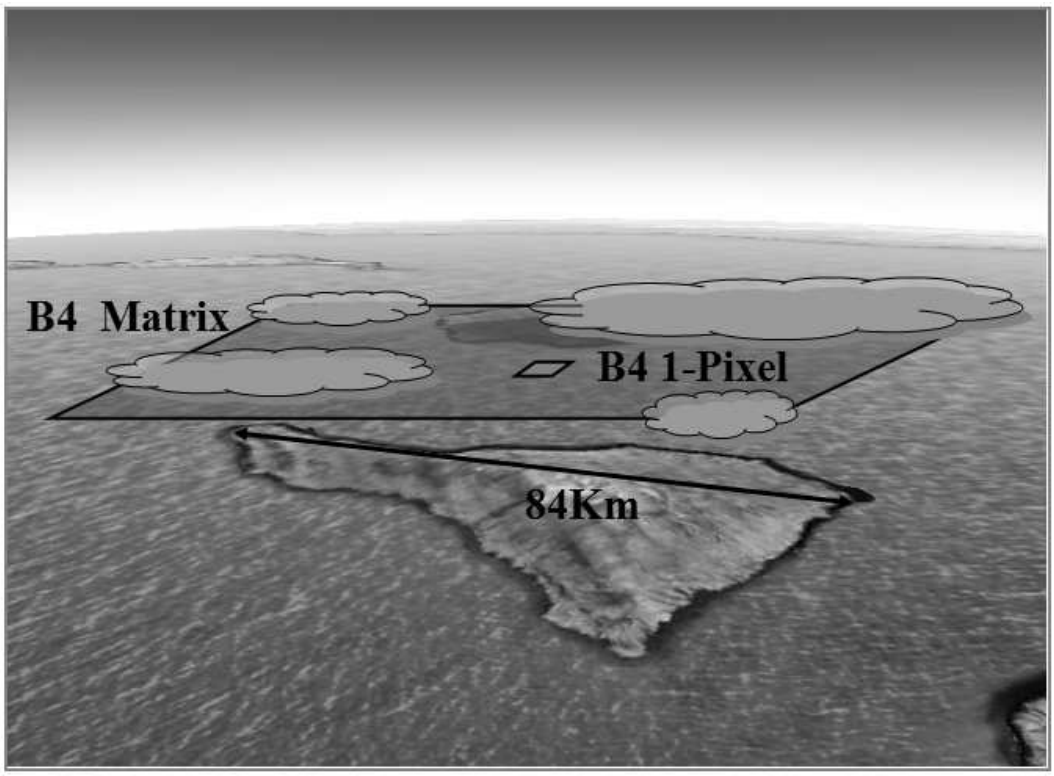

Figure 2.4: Single pixel (small rectangle $4Km \times 4Km$) vs. matrix (wide rectangle $100Km \times 100Km$) coverage comparison at Izaña. The length of the island is approximately $84km$. Figure shows that the use of the single pixel is not sufficient in the case of a partially covered sky to define the properties of the night.

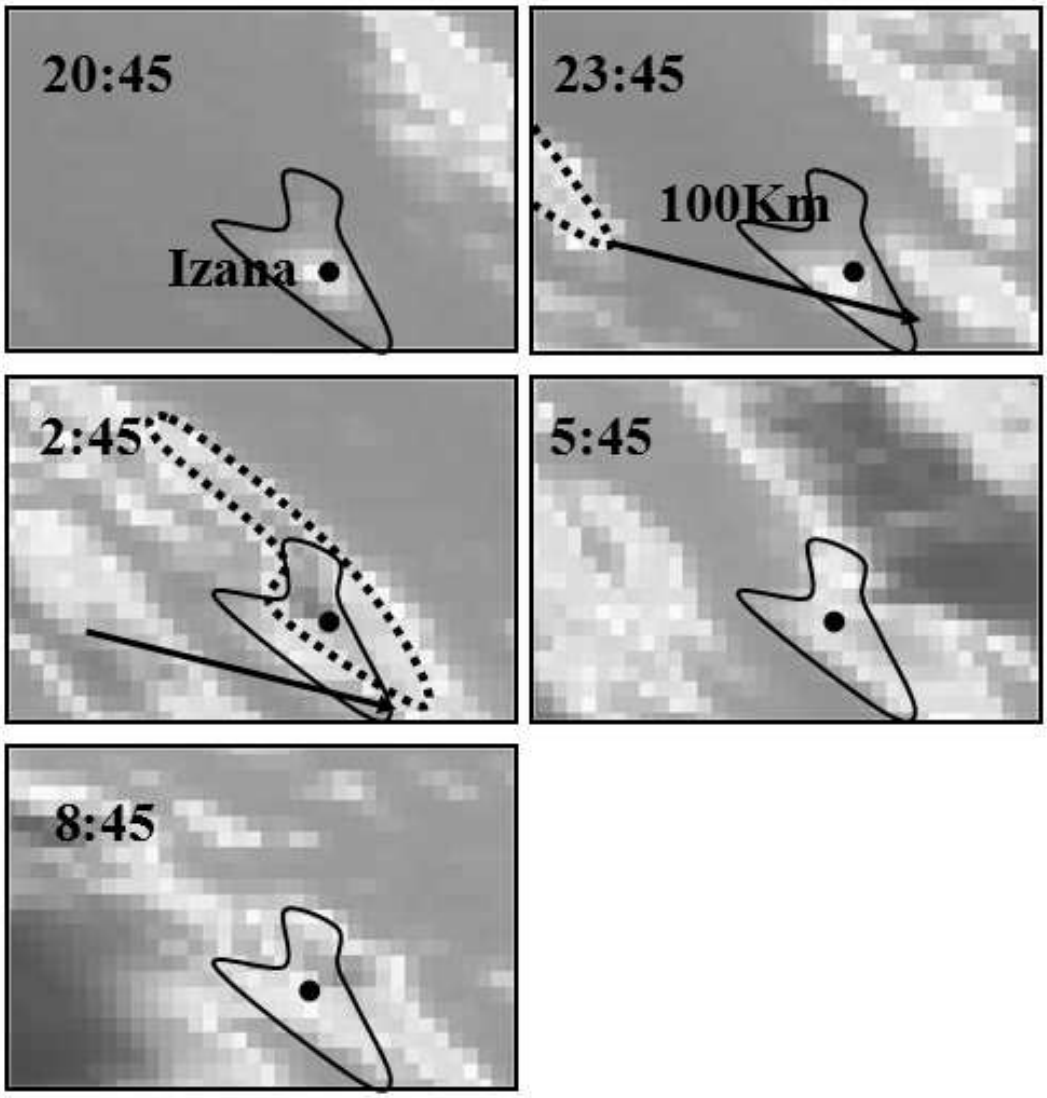

Figure 2.5: Clouds time evolution of a partially covered night (the dotted line represents a moving cloud) at Izaña.

Chapter 3

Remote sounding basic model

The mathematical model used in this analysis is here explained. The emitted monochromatic radiation intensity at a given λ and along a vertical path at the top of the atmosphere, incident at a satellite instrument is given by:

$$R_\lambda = (I_0)_\lambda \tau_\lambda(z_0) + \int_{z_0}^{\infty} B_\lambda T(z) K_\lambda(z) dz \tag{3.1}$$

where:

- $K_\lambda(z) = \frac{d\tau_\lambda(z)}{dz} \Rightarrow$ Weighting Function (WF)
- $B_\lambda T(z) \Rightarrow$ Planck function profile as function of vertical temperature profile T
- $(I_0)_\lambda \Rightarrow$ Emission from the earth surface at height z_0
- $\tau_\lambda(z) \Rightarrow$ Vertical transmittance from height z to space

This equation may also be extended to represent radiation emitted along a slant (non-vertical) path making the approximation of a plane-parallel atmosphere.
For a viewing path through the atmosphere at angle θ to the vertical, we have:

$$\tau_\lambda(z, \theta) = e^{-sec\theta \int_z^\infty \kappa_\lambda(z) c(z) \rho(z) dz} \tag{3.2}$$

where:

- $\rho(z) \Rightarrow$ Vertical Profiles of Atmospheric Density
- $\kappa_\lambda(z) \Rightarrow$ Absorption Coefficient

- $c(z) \Rightarrow$ Absorbing Gas Mixing Ratio

Changing from the notation of a continuous profiles, as in equation (3.1), to discrete profile, and considering the atmosphere as a composition of many thin layers, the corresponding equation becomes:

$$R_i = (I_0)_i \tau_i(z_0) + \sum_{j=1}^{j-1} B_{ij} K_{ij} \tag{3.3}$$

Making substitutions as below:

1. $B_j \Rightarrow I_0$
2. $K_{ij} \Rightarrow \tau_i(z_0)$

Hence equation is given by

$$R_i = \sum_{j=1}^{j} B_j K_{ij} \tag{3.4}$$

Representing the radiance in all channels and the Planck function profile by vectors we have:

$$\vec{R} = \vec{B} \cdot \vec{K} \tag{3.5}$$

where $\vec{K}$ is a matrix containing the discrete weighting function elements $i \times j$. Assuming the problem to be linear (i.e. $\vec{K}$ is $\vec{B}$ independent) the formula to find out the $\vec{B}$ function can be inverted.
The weighting function (WF) specifies the layer from which the radiation emitted to space originates, and hence it determines the region of the atmosphere which can be sensed from space at fixed λ. In such a way many atmospheric layers can be observed by selecting different λ values.
If a standard atmosphere is assumed, the two used WFs of the GOES satellite have the following median height values[1]:

- BAND3: $K_{\lambda_3}(z) = \frac{d\tau_{\lambda_3}(z)}{dz} \Rightarrow \approx 8000m$
- BAND4: $K_{\lambda_4}(z) = \frac{d\tau_{\lambda_4}(z)}{dz} \Rightarrow \approx 4000m$

[1] See http://cimss.ssec.wisc.edu/

These heights depend on the location of the selected earth region. For instance, if we have a site at an altitude $\geq 4000m$, B3 height is supposed to be fairly constant while B4 height are higher. In any case experimental observations confirm that GOES12 B3-B4 bands looks at high layers as regard to soil. In Section 3.2 we describe a new model for the experimental confirmation of the two WFs characteristics.
We now find an analytical expression for the weighting functions, as we will see in the following. We consider the absorption coefficient:

$$\kappa_\lambda(z) = \kappa_\lambda(0) \cdot n(z)$$

where $n(z)$ is the number density profile. It decreases exponentially with altitude as shown by the formula:

$$n(z) = n(0) \cdot e^{-\frac{z}{A}}$$

where A is the scale height and it has a typical value of about $7Km$. Finally, considering the expression of vertical transmittance from height z to space:

$$\tau_\lambda(z) = e^{-\kappa_\lambda(z) \cdot A}$$

the WF expression becomes:

$$K_\lambda(z) = \frac{d\tau_\lambda(z)}{dz} = \kappa_\lambda(z) \cdot e^{-\kappa_\lambda(z) \cdot A} \tag{3.6}$$

This function has its maximum and therefore its observation peak when:

$$\kappa_\lambda(z_{Max}) \cdot A = 1$$

and this corresponds to the altitude given by the formula:

$$z_{Max} = H \cdot ln\left[\kappa_\lambda(0) \cdot A\right] \tag{3.7}$$

Figure 3.1 shows examples of WF. We can see how the change of these functions allows us to observe at all altitudes. In fact, we have the best sensitivity where the function present its peak. The atmosphere becomes transparent to the satellite at altitudes far from it.

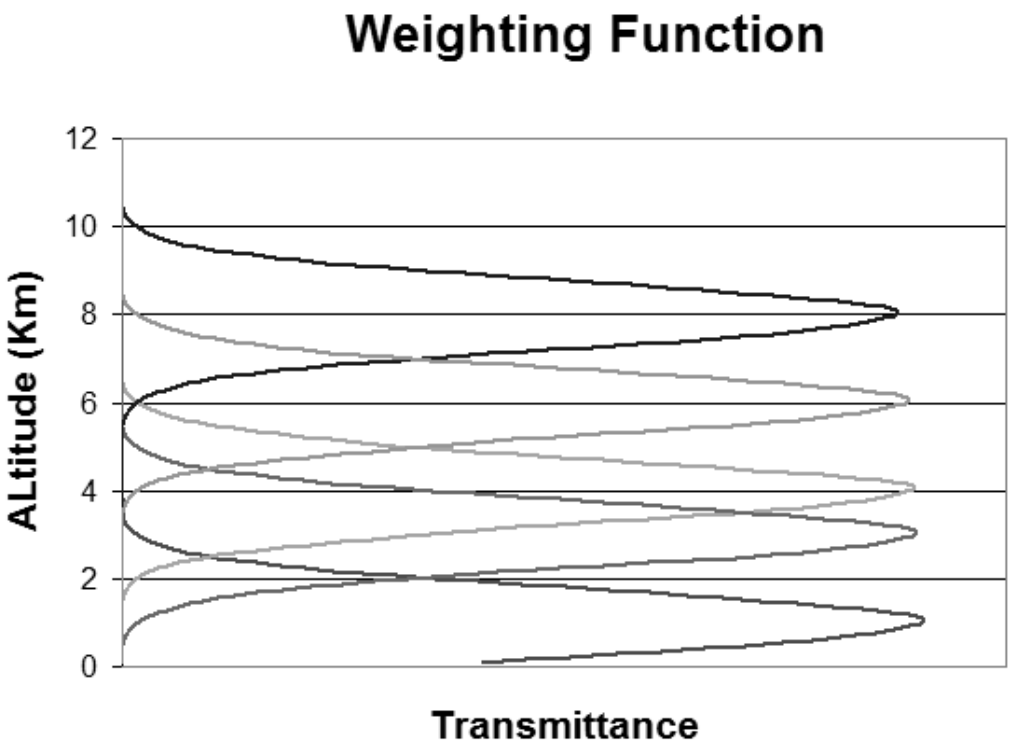

Figure 3.1: Figure shows some examples of WFs. We can see how the change of these functions allows us to observe at all altitudes. In fact, we have the best sensitivity where the function present its peak. The atmosphere becomes transparent to the satellite at altitudes far from it.

3.1 The weighting functions of GOES12

The weighting function (WF) specifies the layer from which the radiation emitted to space originates, and hence it determines the region of the atmosphere which can be sensed from space at fixed λ.
In such a way many atmospheric layers can be observed by selecting different λ values.
If a standard atmosphere is assumed GOES12 WFs have the following median height values[2]:

- BAND3: $K_{\lambda_3}(z) = \frac{d\tau_{\lambda_3}(z)}{dz} \Rightarrow \approx 8000m$
- BAND4: $K_{\lambda_4}(z) = \frac{d\tau_{\lambda_4}(z)}{dz} \Rightarrow \approx 4000m$
- BAND6: $K_{\lambda_6}(z) = \frac{d\tau_{\lambda_6}(z)}{dz} \Rightarrow \approx 3000m$

These heights depend on the location of the selected earth region. For instance Tolonchar B3 height is supposed to be fairly constant while B4 and B6 heights are higher because the site is $4480m$ height. In any case experimental observations confirm that GOES12 B3-B4-B6 bands looks at high layers as regard to soil.

We have seen that the matrix allows an intrinsic increase of the spatial-time resolution: the matrix observes the temporal evolution of the entire sky above the site. Such temporal resolution and coverage can not, therefore, be reached by the models based on analysis of single pixel and the single image for each night.

3.2 WF Day-Night

In this Section we show how to change the image detected by the satellite during the day compared to night. This occurs due to an intrinsic change of the WF. In Equation 3.1 we have seen that the WF depends on the temperature gradient, it changes between day and night due to the physics of the atmosphere. Figure 3.5 shows the difference of these temperature profiles. During the day, the WF observes almost down to the ground while during the night it observes to high atmospheric layers. Figure 3.3 shows in the top panel the topography of the Mt. Graham site. The bottom panel shows two 3D reconstructions of the matrix observed by satellite. We can see that during the day (14:45 local time, GOES B4) the satellite is able to reconstruct

[2]See http://cimss.ssec.wisc.edu/

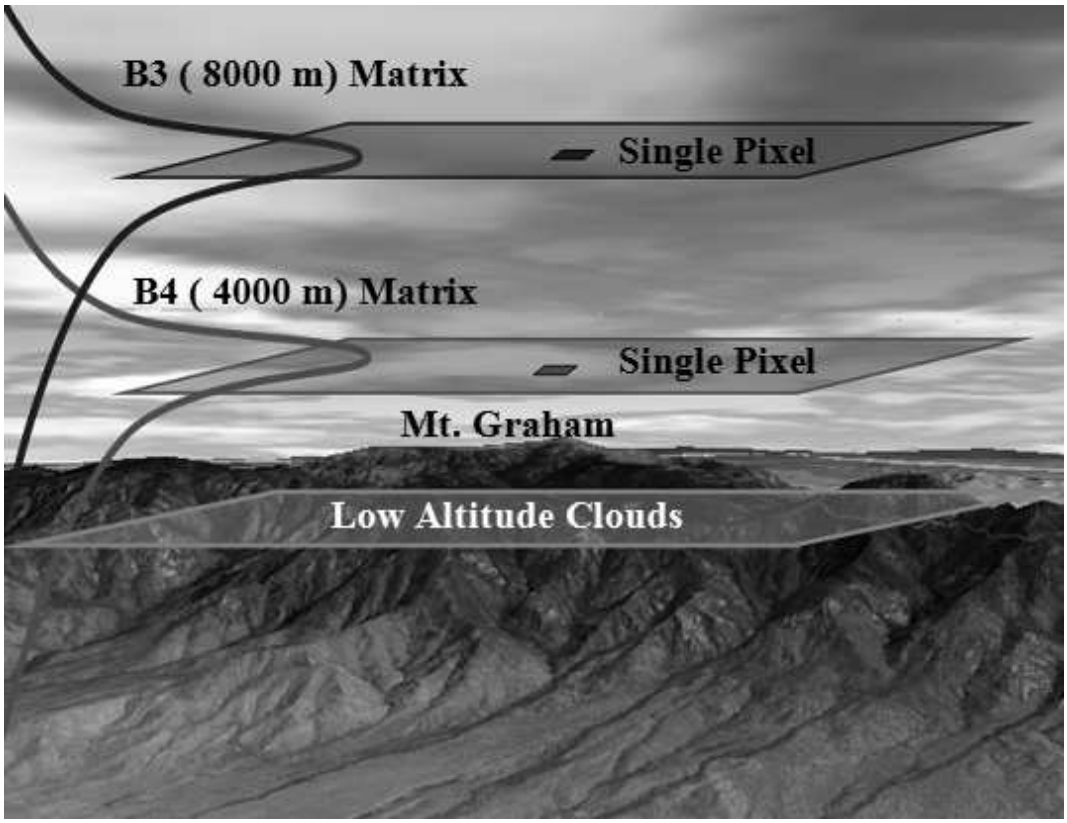

Figure 3.2: Figure shows the topography of the site of Mt Graham. We can see the difference in scale between the matrix and the single pixel. We can also notice the different altitudes of observation due to the GOES Wfs. Finally we can see how the phenomena below the altitude of the observatory are not detected. The matrix projected to altitude of the WF allows the observation of the entire sky above the site. Single pixel (small rectangle $4Km \times 4Km$) vs. matrix (wide rectangle $100Km \times 100Km$) coverage comparison at Mt.Graham. Figure shows that the use of the single pixel is not sufficient in the case of a partially covered sky to define the properties of the night.

the topography of the site and during the night (2:45 local time, GOES B4), however, it observes an homogeneous layer at high altitude. To highlight this result Figure 3.4 shows the two sections in longitude (top panel) and latitude (botton panel) of that image. Considering that Mt Graham is high about $3200m$ we can see how the B4 and B3 observed at high altitudes during the night. This is an experimental verification of the values provided for the GOES WFs and a further verification to justify the use of a large matrix.

3.3 The analysis of the infrared B3-B4-B6 GOES12 bands

A cloud cover analysis is possible by mean of Remote Sounding (RS) application to B3, B4 and B6: in the current models based mainly on B4 analysis only. This band fairly matches thick cloud observation, but it presents some limits in case of thin clouds or minor atmospheric events. These limits are mostly overcome by correlating this band with B3 and B6. Ground vs satellite data show that B3 is capable of detecting atmospheric events such as winds or relevant air displacements. Moreover different air mass changes (e.g. dry, wet, warm or cold wind) is detectable by comparing B4 to B3. Finally a correlation between B6 and B4 allows to gather information about fogs, dusts, thin clouds. In such a way remote sounding model applied to GOES12 bands provides the following atmospheric scheme:

- B3-B4 correlation: high atmospheric events and in particular air mass displacements.
- B4-B6 correlation: low atmospheric events, and in particular fogs, dusts, humidity.

On this base we can provide a sort of atmospheric tomography by satellite data extrapolation. Figure 3.6 shows the distribution of GOES12 emissivity in the three bands at Paranal (upper panel) and the distribution of correlation function $F_{C.A.}(t)$ (bottom left panel) for the month of September 2008. The corresponding atmospheric correlation function it is also shown in the right side of the panel. For each month we have obtained these distributions.

3.4 Atmospheric Correlation Function

As written in the previous sections the $F_{C.A.}(t)$ correlation function used in this analysis is based on three band correlation. Considering GOES 12 WFs the best Remote Sounding is:

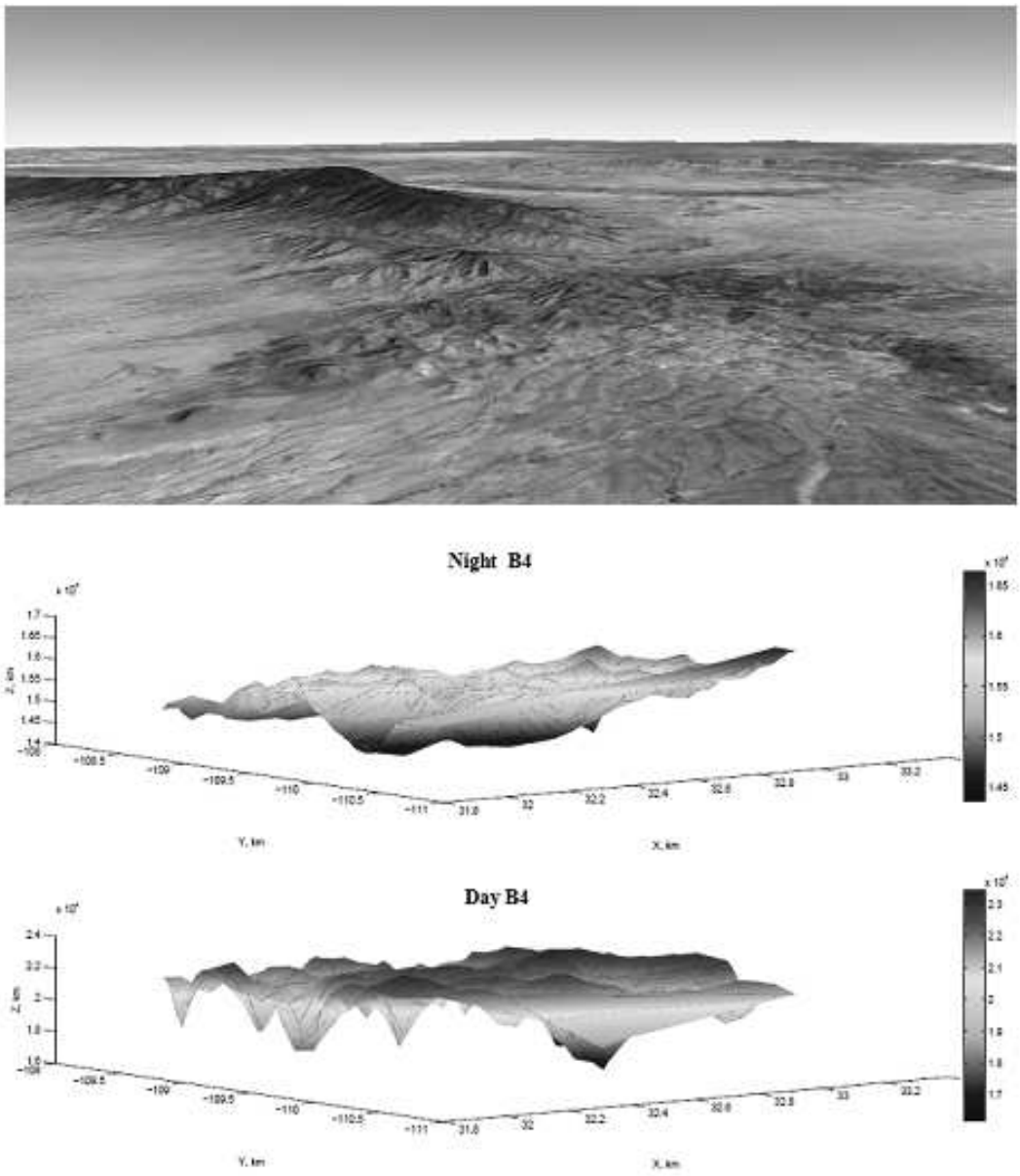

Figure 3.3: Figure shows (top panel) the topographical features of the site of Mt Graham ($2° \times 2°$). The bottom panel shows two 3D reconstructions of the matrix ($2° \times 2°$): the top matrix represents a nocturnal image (2:45 local time) while the bottom matrix a daytime image (14:45 local time). we can see the differences between the two images: the nocturnal image has a more flat trend and remains at a high altitude (we do not distinguish the topography of the site), instead we can see to the ground in the daytime image (we distinguish the overturned profile of the mountains).

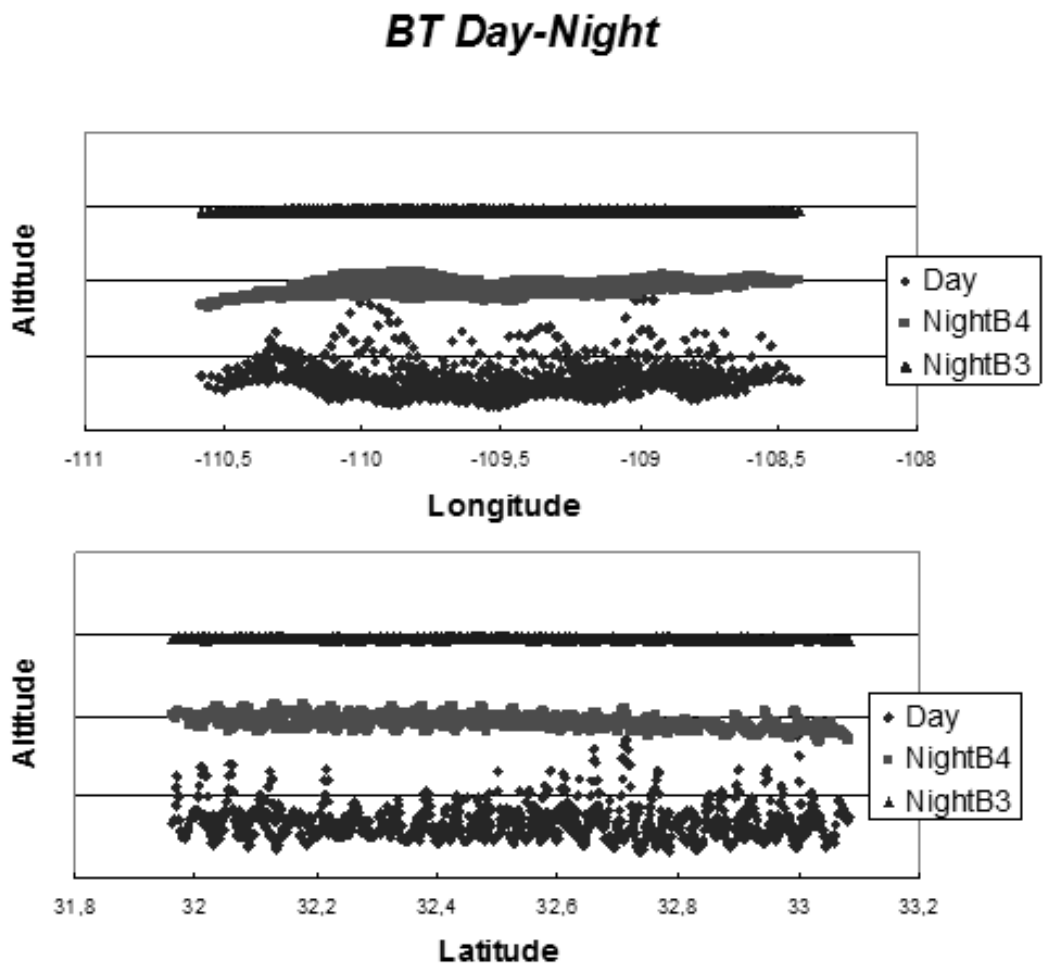

Figure 3.4: Figure shows the front (longitude) and side (latitude) geometric sections of three matrices. The bottom profile is a daytime picture of the band 4 (14:45 local time), the central profile represents a night-time picture of the band 4 (2:45 local time) and top profile is a night-time picture of the band 3 (2:45 local time). Top panel (longitude section) shows the profile of the various mountains that are present on the observed area: in particular the mountain on the left is Mt. Graham (about 3200m). We note that the profile of the band 4 during the night is at an altitude of about 4000m and the profile of the band 3 during the night is at an altitude of about 8000m. Bottom panel (latitude section) confirms these results.

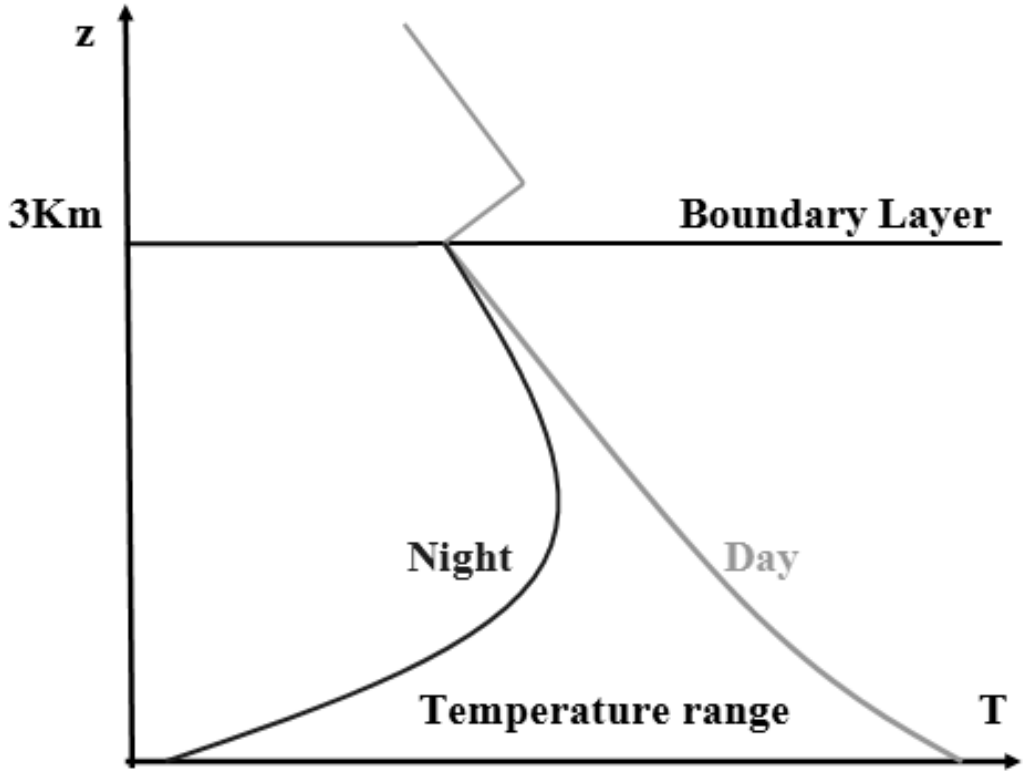

Figure 3.5: Figure shows the differences between the night-day temperature profile in the atmospheric boundary layer. We can understand that if a WF is calibrated to reach the ground during the day, we would need a different function during the night. This is due to the large difference between the two profiles shown and this difference decreases with increasing altitude (z).

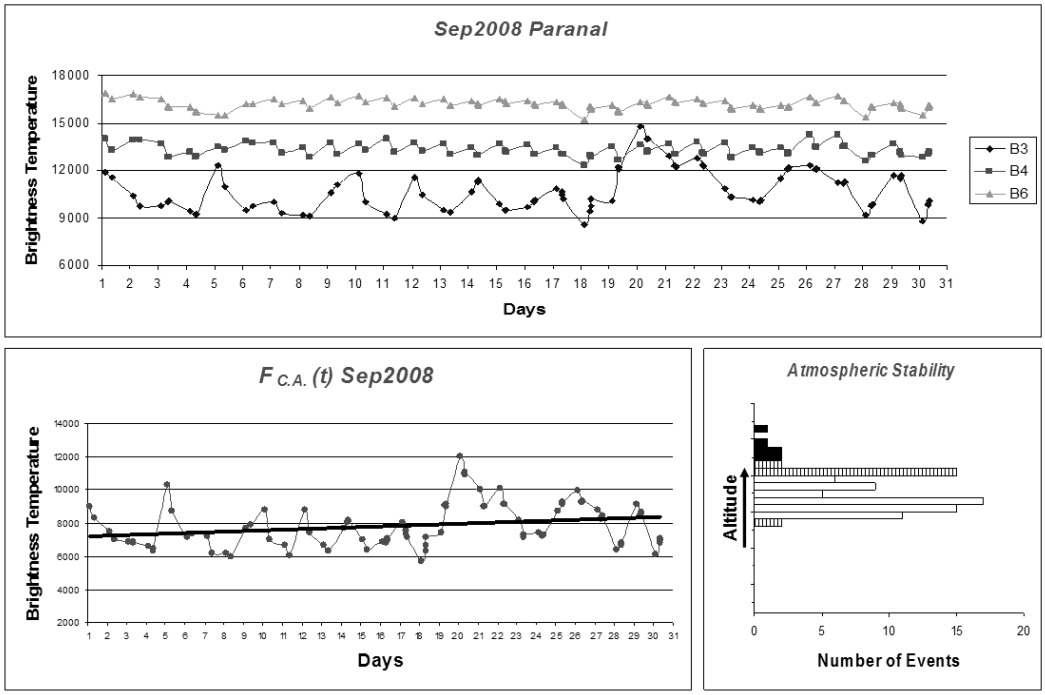

Figure 3.6: GOES 12 emissivity in B3, B4, B6 bands (upper panel) at Paranal for September 2008. Left panel shows the correlation function (the black straight line represents the $F_{C.A.}(t)$ trendline). The corresponding atmospheric stability histogram is shown in the right lower panel.

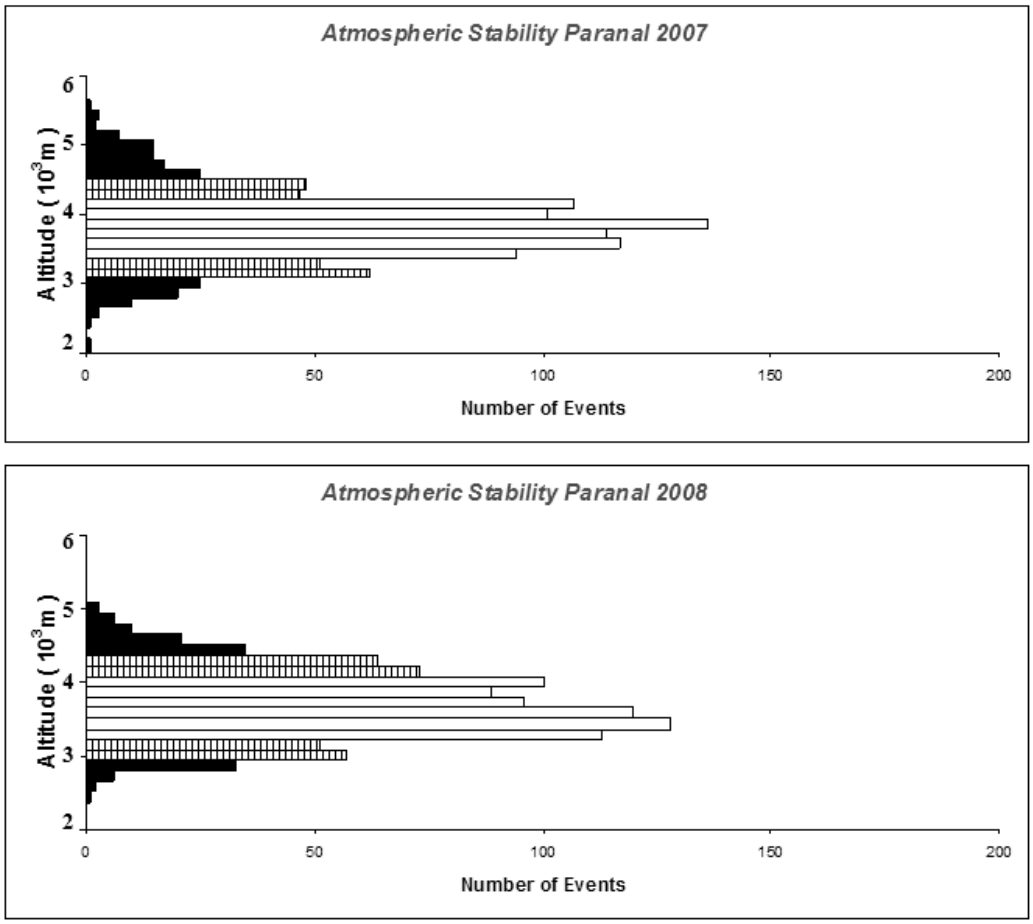

Figure 3.7: Histogram of annual atmospheric stability at Paranal. White bars represent the stable nights, gray bars clear but unstable nights, black bars the nights covered.

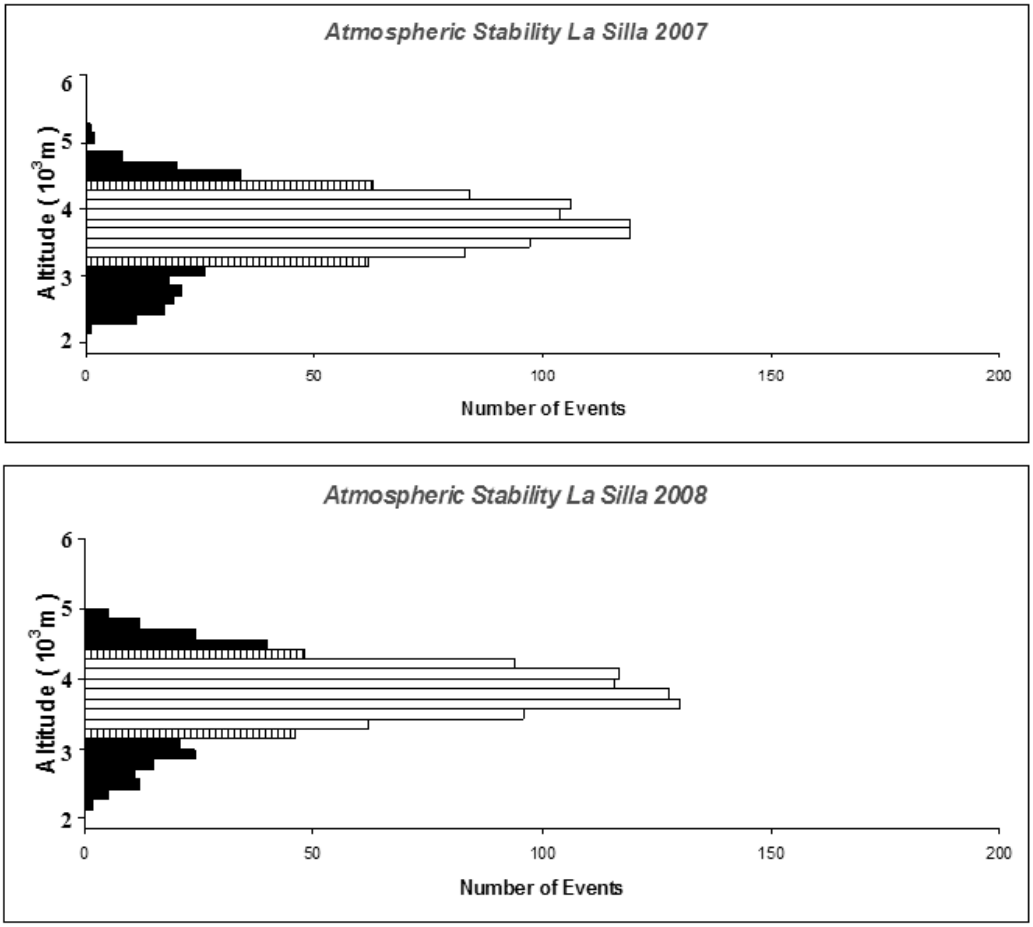

Figure 3.8: Histogram of annual atmospheric stability at La Silla. White bars represent the stable nights, gray bars clear nights but unstable, black bars the nights covered.

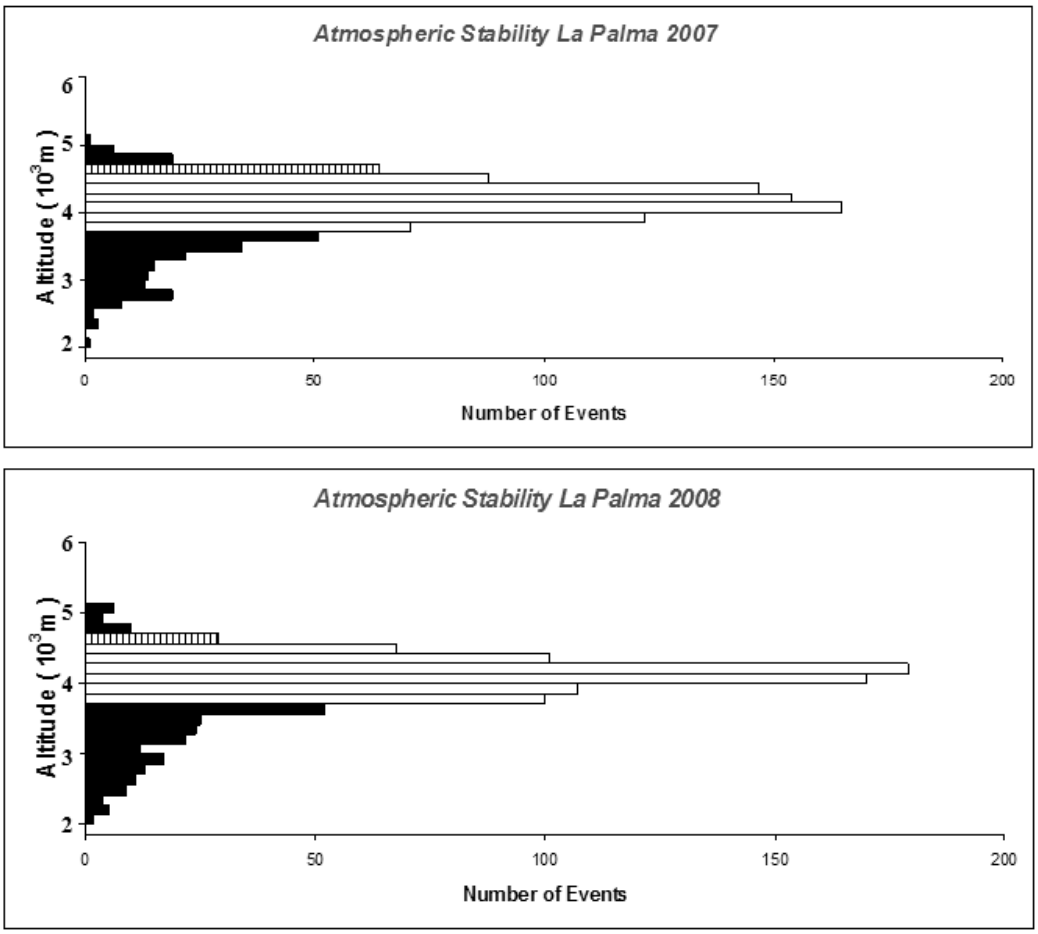

Figure 3.9: Histogram of annual atmospheric stability at La Palma. White bars represent the stable nights, gray bars clear nights but unstable, black bars the nights covered. We note that La Palma instability (black bars) is due mainly to low-altitude phenomena such as fog, dust, etc. as confirmed by log comments.

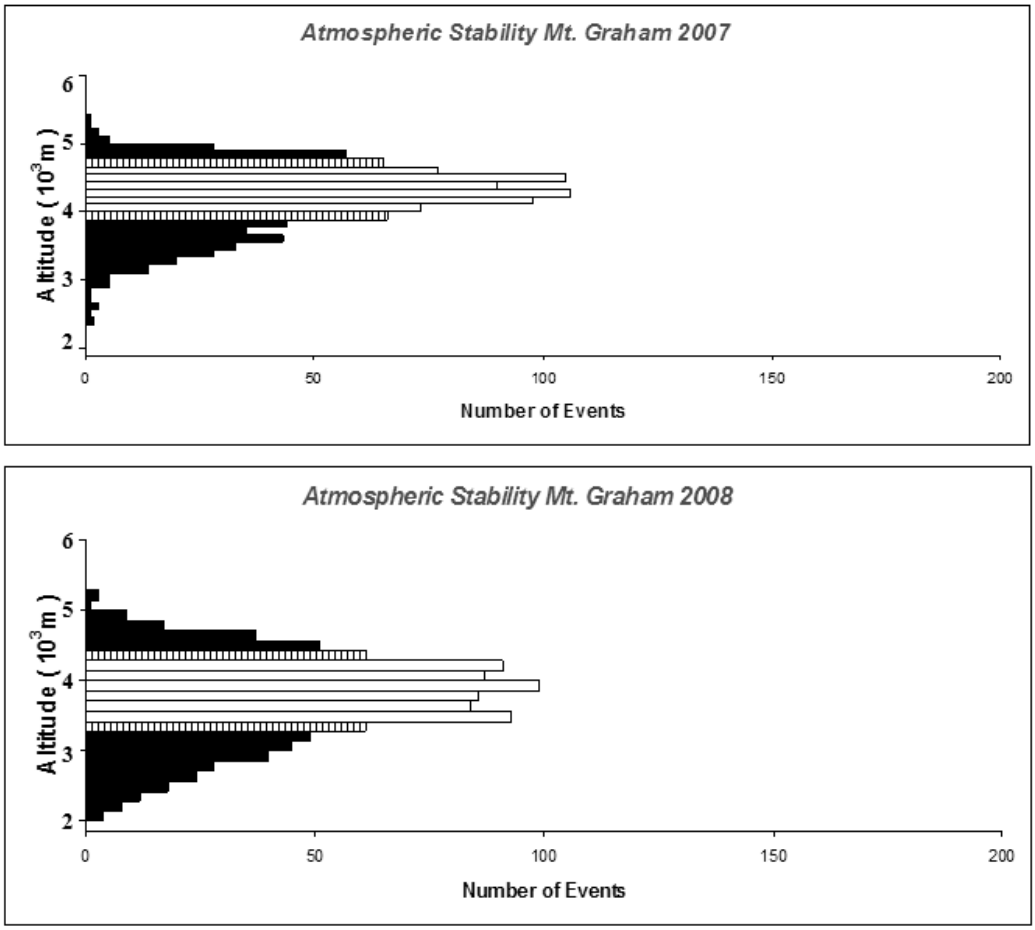

Figure 3.10: Histogram of annual atmospheric stability at Mt.Graham. White bars represent the stable nights, gray bars clear nights but unstable, black bars the nights covered.

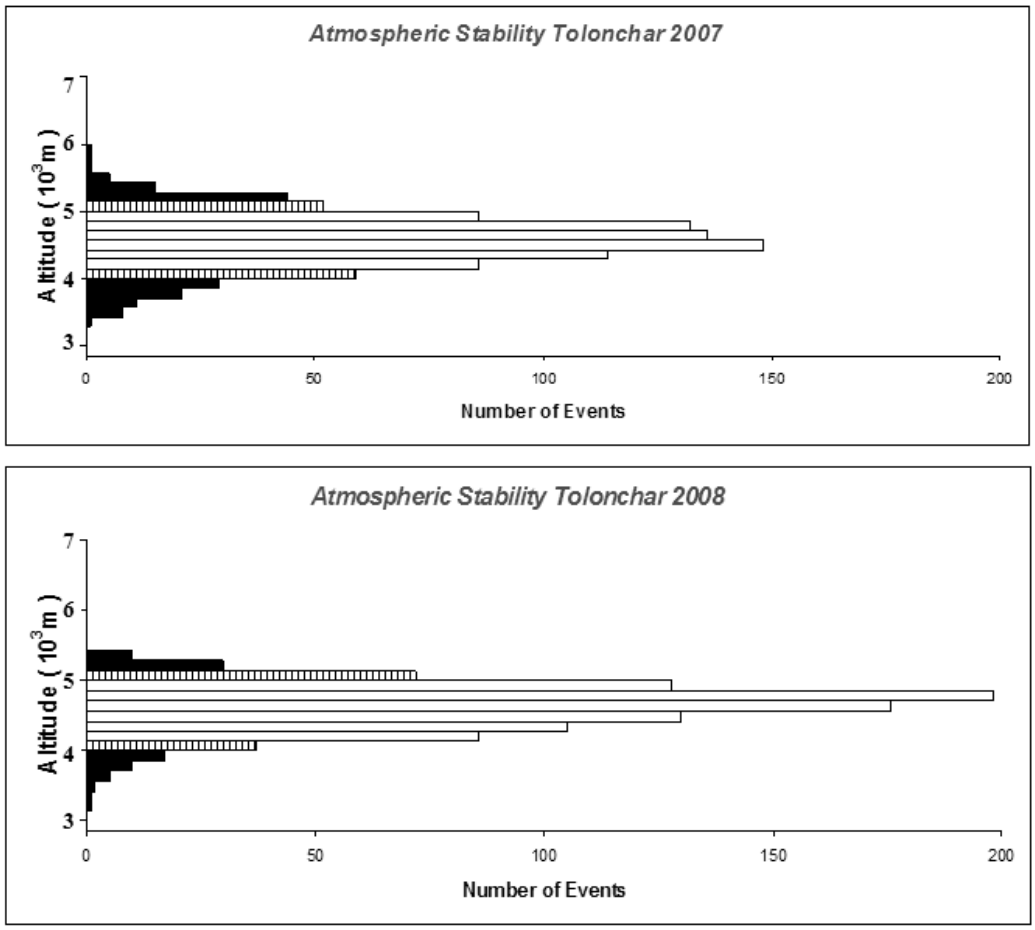

Figure 3.11: Histogram of annual atmospheric stability at Tolonchar. White bars represent the stable nights, gray bars clear nights but unstable, black bars the nights covered.

$$I_{C.A.} = I_{\lambda_3} - [I_{\lambda_6} - I_{\lambda_4}] \tag{3.8}$$

This model takes into account auto-corrections of atmosphere: for instance if two high layers have a positive oscillation and lower layers has an equal magnitude oscillation, but negative, the $F_{C.A.}(t)$ remains constant. From the physical point of view this means that the corresponding wave front observed from earth will be automatically corrected and an event is never been observed, as high atmosphere oscillations provoked by the B3-B4 correlation are always greater than those provoked by the B4-B6 correlation. B4-B6 oscillations can only partially correct the wave front.
In mathematical terms this model provides a brightness temperature of the B3, B4 and B6 combination, given by equation:

$$I_{C.A.} = \frac{R_{\lambda_3} + R_{\lambda_4} - R_{\lambda_6}}{\tau(z_0)} +$$

$$-\frac{\int_{z_0}^{\infty} B_{\lambda_3}[T(z)]K_{\lambda_3} + B_{\lambda_4}[T(z)]K_{\lambda_4} - B_{\lambda_6}[T(z)]K_{\lambda_6} dz}{\tau(z_0)} \tag{3.9}$$

$F_{C.A.}(t)$ can be extrapolated by relating T brightness to time. This function will provide information about atmospheric quality of the surveyed site and the height of the perturbation that is a function of the T brightness. We show in Section 3.6 that this function is related to the seeing.
Subsequently the air mass displacements (dynamical atmospheric instability) can be ranked according to their altitude and then to the kinetic energy. Figure 3.6 will represent a pattern of B3, B4 and B6 at Paranal. The bottom of Figure 3.6 shows the correlation function extrapolated through the RS and the respective histogram of atmospheric stability. This histogram also gives us information on the share that generates the disturbance. We note that the flat distribution of the B4 and B6 show no cloud cover, unlike that of B3, which has strong oscillations. Assuming a standard atmosphere for this band observed at a height of $\approx 8000m$, we infer that the phenomena are of high altitude. Observations from the ground confirm the presence of strong winds and a worsening of the seeing. Figures 3.7, 3.8, 3.9, 3.10, 3.11 depict the histogram of annual atmospheric stability. White bars represent the stable nights, gray bars clear nights but unstable, black bars the nights covered (see Section 4.4 for definitions). The thresholds were obtained solely from analysis of satellite data. Histograms were derived from the correlation function, so they can give information on the contribution of atmospheric phenomenon in question.

3.5 Satellite atmospheric tomography

The atmospheric stability is derived from the atmospheric correlation function. This function, extrapolated from the RS of B3, B4 and B6 bands, is correlated to the integrated structural parameter of the refraction index (C_n^2) and than to the optical turbulence. In fact, as shown belove, the RS of the B3, B4 and B6 bands is function of the changes in temperature at various altitudes. Atmospheric stability can be estimated by involving the model depicted below. Let's consider brightness temperature processed using McIDAS-V package. From a theoretical point of view the brighter a GOES12 image pixel the hotter the observed layer (i.e. lower layer).
Emitted radiation intensities at different satellite observation λ are then:

$$R_{\lambda_3} = (I_0)_{\lambda_3}\tau_{\lambda_3}(z_0) + \int_{z_0}^{\infty} B_{\lambda_3}T(z)K_{\lambda_3}(z)dz$$

$$R_{\lambda_4} = (I_0)_{\lambda_4}\tau_{\lambda_4}(z_0) + \int_{z_0}^{\infty} B_{\lambda_4}T(z)K_{\lambda_4}(z)dz$$

$$R_{\lambda_6} = (I_0)_{\lambda_6}\tau_{\lambda_6}(z_0) + \int_{z_0}^{\infty} B_{\lambda_6}T(z)K_{\lambda_6}(z)dz$$

These equations provide informations about layer height and temperature. Plotting these data as function of time an atmospheric instability function can be extrapolated.

3.6 Correspondence between the seeing and the atmospheric correlation function

In this section we detect a possible correlation between the seeing obtained from the web page of the Robotic Differential Image Motion Monitor (known as RoboDIMM[3]) of Isaac Newton Telescope (INT) and the atmospheric correlation function $F_{C.A.}(t)$ computed for the la Palma sky to test a possible correlation with the image quality.
This RoboDIMM, like all classical DIMMs, relies on the method of differential image motion of telescope sub-apertures to calculate the seeing Fried parameter r_0. RoboDIMM forms four separated images of the same star,

[3]See http://catserver.ing.iac.es/robodimm/

and measures image motion in two orthogonal directions from which it derives four simultaneous and independent estimates of the seeing. The data intepretation makes use of the Sarazin and Roddier's DIMM algorithm as described in (Sarazin & Roddier ([1990])), based on the Kolmogorov theory of atmospheric turbulence in the free atmosphere. There is the possibility that some DIMMs, including the RoboDIMM may have a lower limit threshold in the measurement of the seeing, due to noise, but in our sample (Figures 3.12, 3.13 and 3.14) the seeing values do not have values significantly below $1arcsec$. Moreover in this thesis we do not intend to give an absolute calibration but only a correlation analysis of these two functions.
In fact the solid gray line represents the $F_{C.A.}(t)$ trend. The discontinuous black line represents the available seeing values. We note that the seeing is worse if the $F_{C.A.}(t) > |1\sigma|$ as referred in Section 4.4. A dedicated site testing can clearly improve current models, providing information about fundamental parameters. In a future work we are planning, after an accurate set up of the ING's RoboDIMM (Isaac Newton Group of Telescopes), to correlate the values of seeing with the values of $F_{C.A.}(t)$.
We specify that this is still a preliminary work. In the chapter 8 we analyze in detail this relationship, and we describe a model for the satellite seeing calculation.

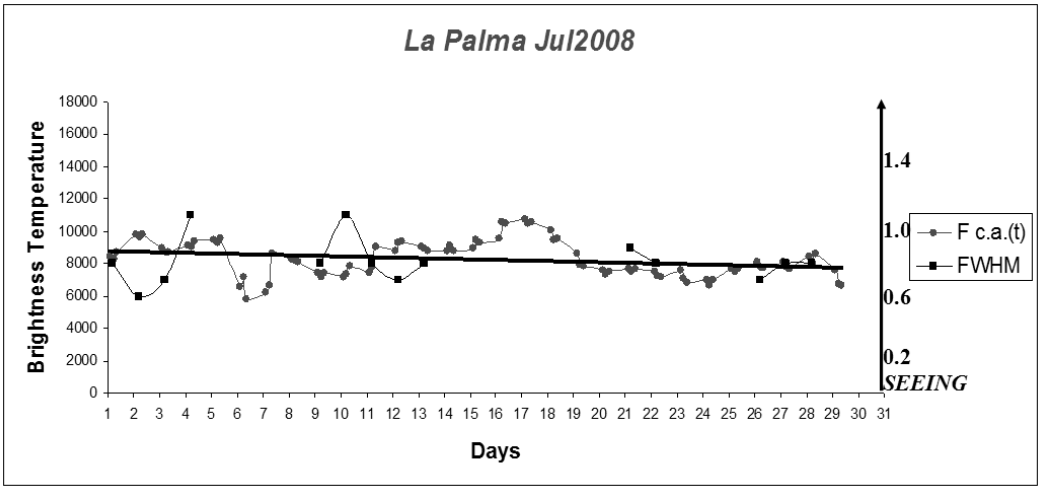

Figure 3.12: Atmospheric Correlation Function-FWHM Correspondence. La Palma, July 2008. The solid gray line represents $F_{C.A.}(t)$ trend. The discontinuous black line represents the available seeing values. The black straight line represents the $F_{C.A.}(t)$ trendline. We note that the worse seeing occurs when the MAX and min values of the $F_{C.A.}(t)$ correspond (Correlation Coefficient= 0.92).

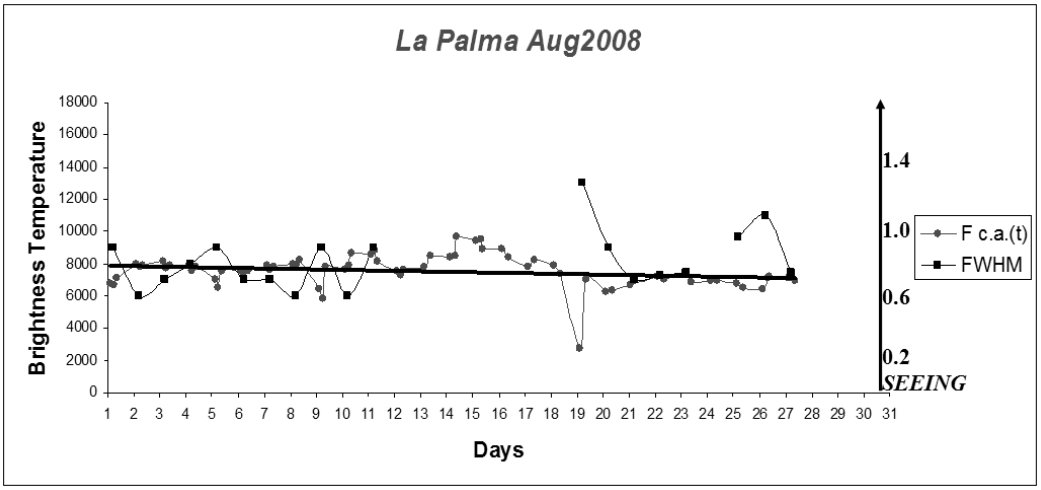

Figure 3.13: Atmosferic Correlation Function-FWHM Correspondence. La Palma, August 2008. The solid gray line represents $F_{C.A.}(t)$ trend. The discontinuous black line represents the available seeing values. The black straight line represents the $F_{C.A.}(t)$ trendline. We note that the worse seeing occurs when the MAX and min values of the $F_{C.A.}(t)$ correspond (Correlation Coefficient= 0.91).

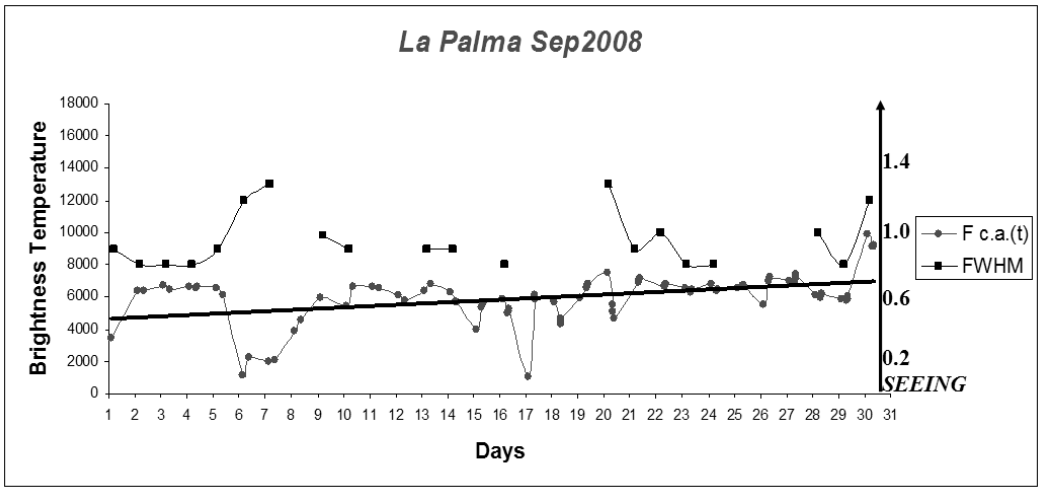

Figure 3.14: Atmosferic Correlation Function-FWHM Correspondence. La Palma, September 2008. The solid gray line represents $F_{C.A.}(t)$ trend. The discontinuous black line represents the available seeing values. The black straight line represents the $F_{C.A.}(t)$ trendline. We note that the worse seeing occurs when the MAX and min values of the $F_{C.A.}(t)$ correspond (Correlation Coefficient= 0.88).

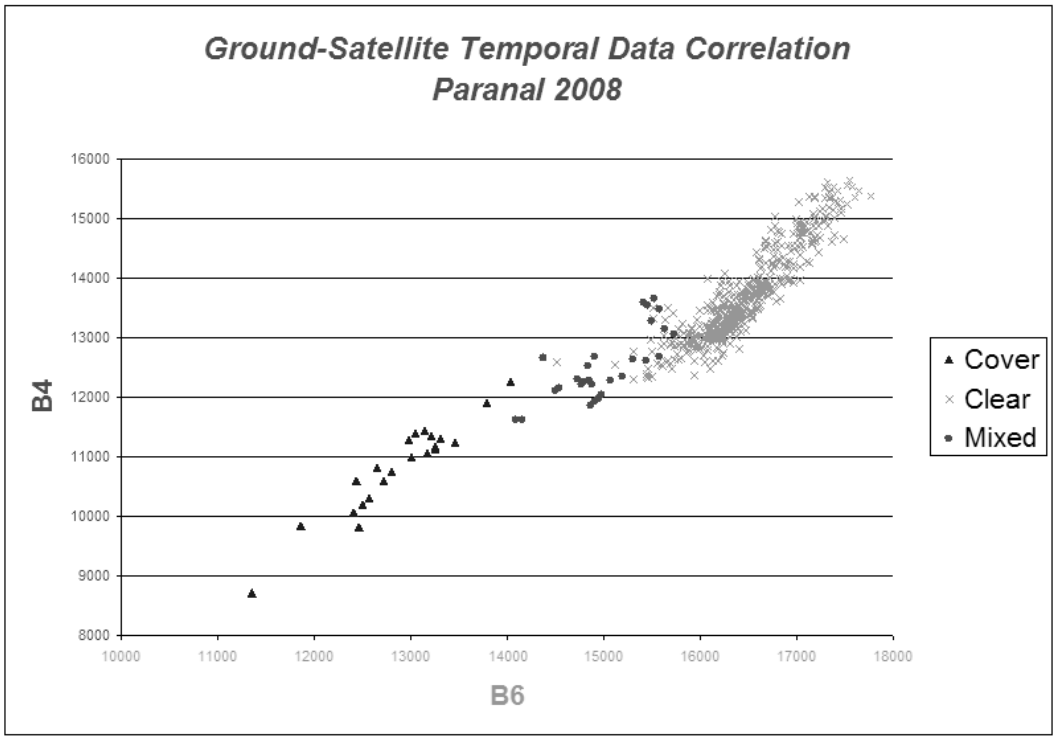

Figure 3.15: Temporal distribution of GOES12 B4 and B6 band emissivity at Paranal in 2008. Sky quality classification has been carried out using the Paranal log.

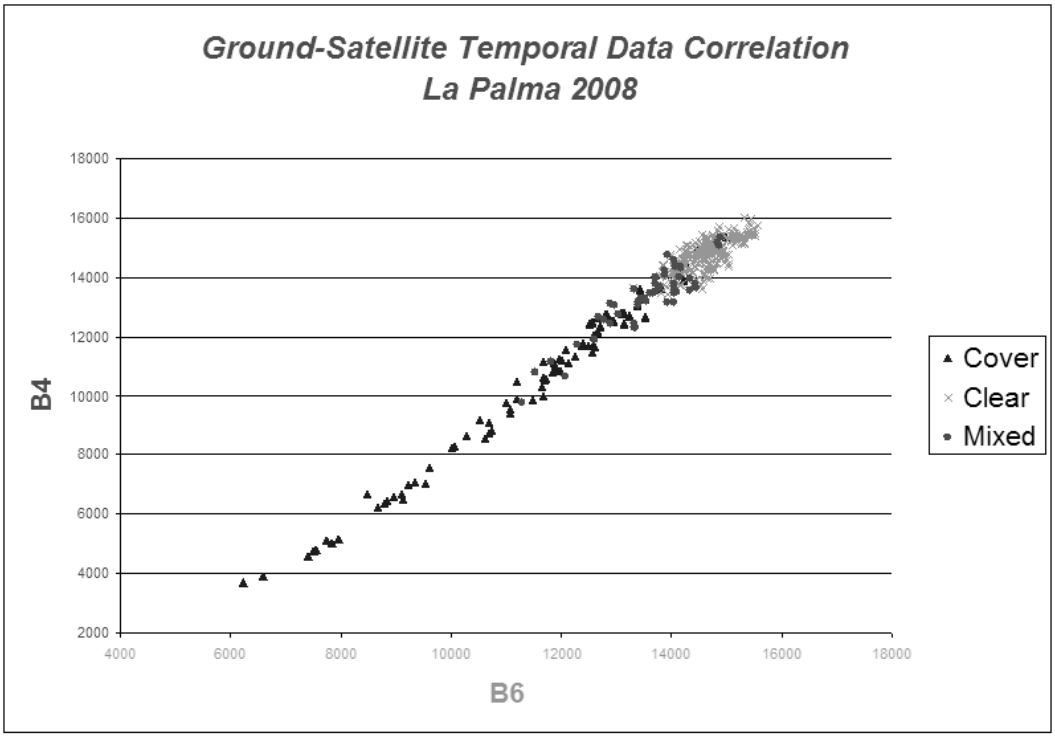

Figure 3.16: Temporal distribution of GOES12 B4 and B6 band emissivity at La Palma in 2008. Sky quality classification has been carried out using the merge of TNG and Liverpool ground based data.

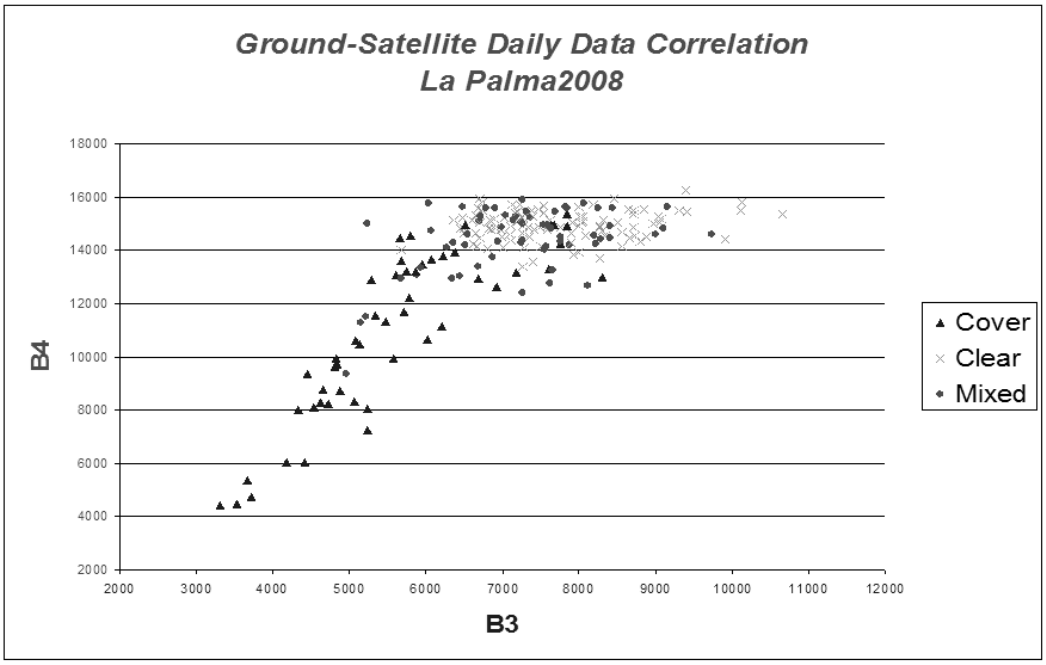

Figure 3.17: Daily distribution of GOES12 B3 and B4 band emissivity at La Palma in 2008. Sky quality classification has been carried out using the TNG log.

Chapter 4

Temporal data analysis

The ground-satellite correlation model used in this article is based on a temporal data correspondence of ≈ 3 values for each night. We have in fact multiple values for each night (≈ 3) and this gives us the opportunity to do a detailed analysis of various conditions. We have also a larger number of data and this, from a statistical point of view, allows to validate the model. Figure 3.15 and 3.16 shown the plots of the obtained temporal emissivity of B4 band vs B6 for the 2008 at Paranal and at La Palma. The nights are classified as a function of the sky quality obtained from the observing log of each analysed site. It appears that clear nights present high values of emissivity.
Moreover Fig. 3.16 shows a lower dispersion and a better separation of clear nights if compared with Fig. 3.17 confirming once more the better quality of the adopted method. From Fig. 3.15 and Fig. 3.16 we can define as clear all the nights having B4 $\geq$ 13000 *Units* at Paranal, while at La Palma we can define as clear all the nights having B4 $\geq$ 13900 *Units*. Table 4.1 shows the obtained percentage of clear, mixed and covered nights at Paranal and at La Palma in the year 2008 from a temporal punctual analysis. As in Paper III, we have found that the fractions of clear time based on satellite data are greater than those of clear nights using ground based data. The differences seem higher than the biases of single logbooks. In fact the amount of nights computed using the different adopted logbooks gives a similar percentage with differences around 2% (computed in the same period, 2008-2009) when a careful and homogeneous analysis is performed.
The obtained percentages are in reasonable agreement with the results reported in Garcia-Gil et al. ([2010]).
We can conclude that the nights classification is more dependent on the adopted methodology and accuracy rather than on biases in the adopted logbooks. The differences can be better explained considering that some

local effects could be ignored by satellites. In addition, we note that considering the fraction of clear time fraction from satellite data vs. that of clear nights from ground data, the first fraction is obviously higher.
However we don't expect a large discrepancy as we demonstrated in Paper III where we found that the fraction of partially used nights is very small. It is interesting to note that we found an amount of satellite clear nights close to that obtained in Paper III even if we have used different bands: we obtained 71.9% of clear nights in Paper III, obtained analysing B3 vs B4 bands, and 71% of clear nights in the present analysis obtained plotting B4 vs B6 bands, but the thresholds are fixed considering only B4 (see Section 4.3).
The last row of Table 4.1 shows the percentage of accuracy to associate to each obtained fraction of nights. The uncertainty is computed as follows:

- $\Delta_{Clear/Mixed} \Rightarrow$ Clear/Mixed Uncertainty
- $\Delta_{Clear/Covered} \Rightarrow$ Clear/Covered Uncertainty
- $\Delta_{Mixed/Covered} \Rightarrow$ Mixed/Covered Uncertainty

We note that the largest satellite uncertainty derives from the overlap of clear and mixed nights, while the satellite is accurate in other cases. It is interesting the comparison between the temporal and daily methods.
Figure 3.17 represents daily distribution of GOES12 B3 and B4 band emissivity at La Palma in 2008. We note how the graph is more dispersed compared to the graph of Figure 3.16. This is due to the greater accuracy of the temporal method and the use of different bands: B3 and B6 respectively. In fact the B6 trend is more regular.
Table 4.2 shows the comparison between temporal and daily data analysis. We can observe how the temporal method uncertainties are smaller than the daily method uncertainties. In this case we chose annual thresholds and considered the mathematical error, the method provides the greatest advantages choosing monthly thresholds and considering the statistical error. The monthly thresholds make it possible to consider seasonal temperature changes of the site reducing the overlap percentages.
As final check Figure 4.1 plots the B4 emissivity (black line) and log ground data (gray line) for February 2008 at Paranal. It is evident that the monthly distribution of the emissivity follows the ground data.

Table 4.1: Clear/Mixed/Covered nights percentage and overlaps at Paranal and La Palma in 2008. Temporal data analysis.

	Ground			Satellite		
	Clear	Mixed	Covered	Clear	Mixed	Covered
Paranal	91%	7%	2%	84%	14%	2%
La Palma	66%	12%	22%	71%	11%	18%
	Paranal			La Palma		
Uncertainty	$\Delta_{Clear/Mixed}$	$\Delta_{Clear/Covered}$	$\Delta_{Mixed/Covered}$	$\Delta_{Clear/Mixed}$	$\Delta_{Clear/Covered}$	$\Delta_{Mixed/Covered}$
Percentage	7%	1%	2%	7%	3%	5%

Table 4.2: Clear/Mixed/Covered nights percentage and overlaps at La Palma in 2008. Comparison between temporal and daily data analysis.

	Ground			Satellite		
	Clear	Mixed	Covered	Clear	Mixed	Covered
La Palma (Daily)	60%	21%	19%	69%	15%	16%
La Palma (Temporal)	66%	12%	22%	71%	11%	18%
	La Palma (Daily)			La Palma (Temporal)		
Uncertainty	$\Delta^D_{Clear/Mixed}$	$\Delta^D_{Clear/Cover}$	$\Delta^D_{Mixed/Cover}$	$\Delta^T_{Clear/Mixed}$	$\Delta^T_{Clear/Cover}$	$\Delta^T_{Mixed/Cover}$
Percentage	9%	3%	9%	7%	3%	5%

4.1 Discussion of error propagation and thresholds

In our model the various thresholds to classify the nights were chosen by the individual analysis of satellite data. This also allows to study sites for which we have no ground data.
The thresholds were selected via the night temperature range detected by satellite and not through the real night brightness temperature range of the site.
This choice was made because the satellite temperature resolution decreases with the observation angle. In fact at La Palma we observe a temperature range lower than other sites. If we consider:

$$Night\ Satellite\ Temperature\ Range = 1\sigma$$

we note that the use of the matrix decreases the threshold value reducing the satellite noise. This makes the model more accurate (Fig.4.2).
The thresholds for each data classification are described below.

4.2 Resolution correlation matrix thresholds

In this section we compare the brightness temperature difference between the single pixel and the matrix method. We assume that the data are correlated

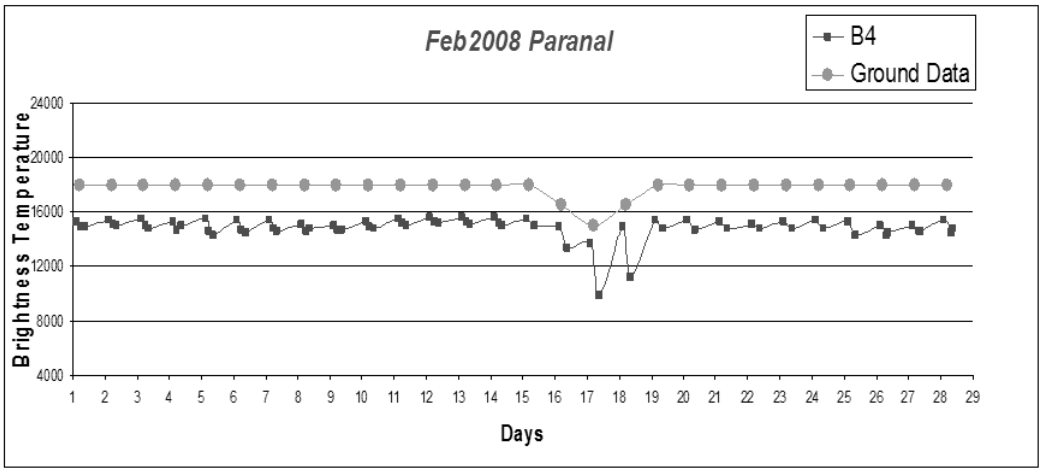

Figure 4.1: Ground Data-Satellite Data Correlation. Paranal, February 2008.

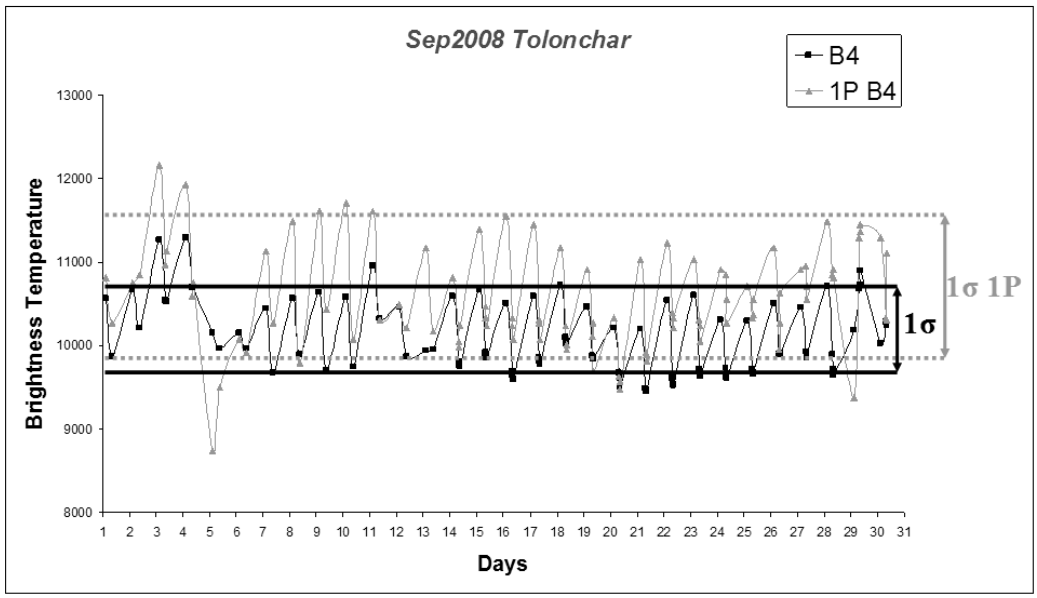

Figure 4.2: Comparison between the single pixel threshold of 1σ and the matrix threshold of 1σ at Tolonchar in September 2008. Figure represents a pattern of $1^\circ \times 1^\circ$ matrix (black line) and the single pixel (gray line) in B4 band for a single month. We note how the use of the matrix decreases the threshold value reducing the satellite noise. This makes the model more accurate.

if the difference is $\leq |1\sigma|$. Figures 2.2 and 2.3 report the obtained percentage of correlation.

$$\left|T^{1Pixel}_{Brightness} - T^{Matrix}_{Brightness}\right| < |1\sigma|$$

where:

- $T^{1Pixel}_{Brightness} \Rightarrow$ Brightness temperature of the single pixel
- $T^{Matrix}_{Brightness} \Rightarrow$ Brightness temperature of the $1° \times 1°$ matrix

4.3 Clear, mixed, covered nights classification

The nights are classified using GOES12 B4 band. The classification of the nights is based in the following assumption: the maximum monthly brightness temperature T_B^{Max} occurs in clear condition.
The other monthly brightness temperatures are correlated with T_B^{Max} when:

- $T_B^{Max} - T_B \leq 2\sigma \Longrightarrow$ Clear
- $2\sigma < T_B^{Max} - T_B \leq 3\sigma \Longrightarrow$ Mixed
- $T_B^{Max} - T_B > 3\sigma \Longrightarrow$ Covered

where $T_B \Rightarrow$ Brightness temperature of the $1° \times 1°$ matrix.
From this definition "clear" sky means a matrix where there are no clouds. As concerning the ground based data we define "clear" the nights cloud free in the logbooks and completely usable for observations.
"Mixed" are nights where comments of presence of clouds or meteorological events (fog, wind, humidity...) have been found, but part of night was used.
"Covered" are unusable nights due to clouds or fog.

4.4 Clear, Stable Nights Classification

We calculated the monthly percentage of clear time relying on temporal data analysis. With this method we classify the fraction of each night by reading multiple data (e.g. if we have three data for a night, two clear values and one covered value, the percentage of clear night will be 67%). This is a definition close to the classical "spectroscopic time". We define "stable" a clear sky without atmospheric phenomena that may affect the photometric quality (wind, fog, humidityĚ).

The monthly percentage of photometric time is calculated by the same method and this is close to the classical definition of the "photometric time". This classification is very important because the photometric quality of clear sky, is influenced by phenomena not detectable by the methods currently used. Finally, we clarify that an unstable sky might be still useful for observing because it is a subset of clear sky. This explains the differences in percentages of our classification (see Tables 4.4 and 4.5).
To be more clear we specify that we calculated the time fraction, not the whole night fraction.
If we take into account the atmospheric correlation function T_B^{Max}, it is possible to introduce the concept of stable nights. Considering $F_{C.A.}(t)$ trendline we get the following classification:

- $\left|T_B - T_B^{Trendline}\right| \leq |1\sigma| \Longrightarrow$ Stable
- $|1\sigma| < \left|T_B - T_B^{Trendline}\right| \leq |2\sigma| \Longrightarrow$ Clear
- $\left|T_B - T_B^{Trendline}\right| > |2\sigma| \Longrightarrow$ Covered

where:

1. $T_B^{Trendline} \Rightarrow$ Brightness temperature of the monthly trendline
2. $T_B \Rightarrow$ Brightness temperature of the $1^\circ \times 1^\circ$ matrix

Through this classification we obtain the histograms in Figures 3.7, 3.8, 3.9, 3.10, 3.11. White bars represent the stable nights, gray bars represent clear but unstable nights, black bars represent the covered nights.
The thresholds were obtained only from analysis of satellite data. Histograms were derived from the correlation function, so they can give information on the contribution of atmospheric phenomenon. The final results are reported in Tables 4.4 and 4.5.

4.5 Mathematics errors propagation

Tables 4.1, 4.2 show the uncertainties to associate to each single data computed through the formula:

$$\Delta_{Tot} = \sqrt{(\Delta_{Cl/Mix})^2 + (\Delta_{Cl/Co})^2 + (\Delta_{Mix/Co})^2}$$

obtaining the following values:

Table 4.3: Clear/Mixed/Covered nights classfication and Clear/Stable nights classfication. Table shows the classification algorithm used in the model. First line shows the classification of cloud cover, second line is a subclassification of clear nights. For example if we consider a clear night (no clouds), the model can classify this night stable or clear. The concept of stable night is comparable to the astronomical concept of photometric night while the concept of clear night is comparable to the astronomical concept of spectroscopic night. Very important is the definition of the used threshold σ. We see that this value is extrapolated directly from the satellite data. This allows us to have an autocalibration of the model: for each site, the algorithm generates a different threshold that takes into account the various characteristics of the site.

$1\sigma = T_B^{23:45} - T_B^{8:45}$	
Clear	$T_B^{Max} - T_B \leq 2\sigma$
Mixed	$2\sigma < T_B^{Max} - T_B \leq 3\sigma$
Covered	$T_B^{Max} - T_B > 3\sigma$
Stable	$\left\|T_B - T_B^{Trendline}\right\| \leq \|1\sigma\|$
Clear	$\|1\sigma\| < \left\|T_B - T_B^{Trendline}\right\| \leq \|2\sigma\|$

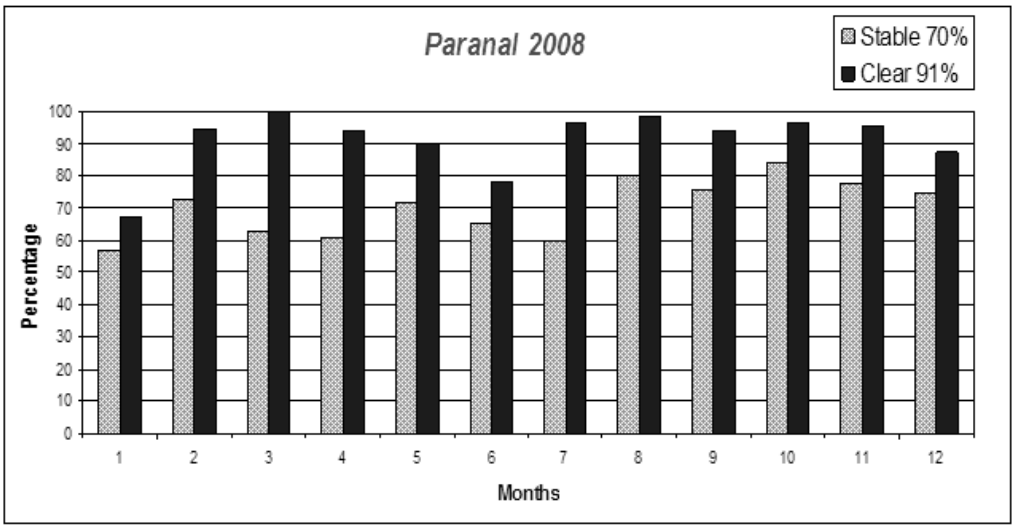

Figure 4.3: Clear and stable night fractions at Paranal 2008 from GOES12 satellite.

- Paranal $\Rightarrow \Delta_{Total} = 7.3\%$
- La Palma (Temporal) $\Rightarrow \Delta_{Total} = 9.1\%$
- La Palma (Daily) $\Rightarrow \Delta_{Total} = 13.1\%$

We observe that the temporal method for La Palma reduces the total uncertainty by 4%.

4.6 Statistics Errors Propagation

Now we consider the statistical error with the unbiased data assumption. We have $N(Ground; Satellite)$ pairs of values and in this case, considering the mathematical error for each site, the standard deviation on the function $F_{\Delta}(Ground; Satellite)$ is derived by the formula:

$$\sigma_{F_{\Delta}} = [\Delta_{Total}]^2$$

Finally, if we consider the number of data ($N(Ground; Satellite)$), the annual statistical uncertainty ($\Delta_{Statistical}$) of the model is given by the formula:

Table 4.4: Satellite Mean Monthly Percentage 2007.

	Paranal		La Silla		La Palma		Mt.Graham		Tolonchar	
	Clear	Stable	Clear	Stable	Clear	Stable	Clear	Stable	Clear	Stable
January	73	55	72	72	38	38	48	48	54	42
February	90	61	90	88	61	61	45	45	72	62
March	86	65	75	75	52	52	51	51	81	63
April	74	58	64	58	75	75	61	61	94	64
May	91	72	59	59	86	86	59	59	87	87
June	60	55	33	33	94	88	72	72	69	69
July	89	82	56	56	93	86	14	14	82	82
August	87	76	65	65	93	93	41	41	89	89
September	94	78	73	73	80	80	44	44	100	92
October	100	91	93	90	80	80	72	69	93	84
November	98	80	85	85	48	48	53	52	93	79
December	80	55	78	78	84	80	72	71	91	76
Mean	85	69	70	69	74	72	53	52	84	74
Clear-Stable Mean	77		70		73		52		79	

Table 4.5: Satellite Mean Monthly Percentage 2008.

	Paranal		La Silla		La Palma		Mt.Graham		Tolonchar	
	Clear	Stable	Clear	Stable	Clear	Stable	Clear	Stable	Clear	Stable
January	67	57	100	68	52	52	49	49	52	52
February	95	73	96	74	68	68	60	60	85	81
March	100	63	93	74	52	52	86	80	99	74
April	94	61	82	82	77	77	93	78	100	80
May	90	72	71	71	87	82	75	70	91	77
June	78	65	64	64	90	90	74	66	72	72
July	97	60	74	65	95	84	20	20	99	88
August	99	80	72	72	90	90	24	24	95	91
September	94	76	56	56	71	71	74	74	100	97
October	97	85	80	77	82	82	86	80	100	89
November	96	78	97	88	37	37	71	71	100	83
December	88	75	100	85	45	45	62	62	70	70
Mean	91	70	82	73	71	69	65	61	89	80
Clear-Stable Mean	81		78		70		63		84	

$$\Delta_{Statistical} = \frac{\sigma_{F_\Delta}}{\sqrt{N(G;S)}}$$

Table 4.6 shows the obtained values whit the $\Delta_{Statistical}$ rounded to integers.

Table 4.6: Mathematical and statistical uncertainties of the model in 2008 at Paranal and La Palma.

Site	Δ_{Total}	$N(G;S)$	$\Delta_{Statistical}$
Paranal	7.3%	1050	2.0%
La Palma (Temporal)	9.1%	1020	3.0%
La Palma (Daily)	13.1%	340	9.0%

Chapter 5

Preliminary model conclusion

In this chapters we have presented a new homogeneous method in order to obtain the amount of available time fraction. The data are extracted from GOES12 satellite imager on five very important and different astronomical sites in order to get comparable statistics. Satellite data are compared with ground based data.
In this analysis a wider spatial field is used in order to reduce the spatial noise: each value is the mean of $1^\circ \times 1^\circ$ matrix. The cloud coverage is obtained using GOES12 B4 and B6 bands independently. Using the correlation of three bands (B3, B4 and B6) we have computed an atmospheric correlation function as a further selection of the clear nights, and we have introduced the new concept of stable night. Temporal data are used for the years 2007 and 2008. We have shown that the derived atmospheric correlation function is correlated with the quality of the night in terms of FWHM (possibly also with wind and humidity). An example of clear/stable nights is given in Fig. 4.3 that shows the monthly distribution of 2008 nights at Paranal. The black bars represent the monthly percentage of clear nights, while the gray bars the percentages of stable nights. We can assume that stable nights could be the best approximation to the photometric nights. We obtained that the amount of stable nights is considerably lower than the clear nights in all the five analysed sites. In view of a better tuning of the stable nights as a function of the ground based parameters, we can adopt as a best approximation of the "clear nights" of the ground based log the satellite clear night percentages.
The mean of the 2007-2008 give a percentage of clear time of 88% at Paranal, 76% at La Silla, 72.5% at La Palma, 59% at Mt. Graham and 86.5% at Tolonchar. These percentage differences are higher than the statistical errors (Table 4.6).
Tolonchar and Paranal (Tables 4.4 and 4.5) show the largest number of clear nights but Tolonchar shows the largest number of stable nights, while La

Palma shows that if a night is clear is also almost stable. Tolonchar appears the best site as concerning the stable nights while Paranal is the best for the clear nights (see also Figures 3.7 and 3.11).
The procedure adopted in this thesis gives different percentages of satellite clear nights when compared with those of Erasmus & van Rooyen ([2006]). In fact we found 88% of clear nights at Paranal to compare with the Erasmus's percentage of 85%, instead, at La Palma we found the 72.5% to compare with the 83.7% of Erasmus. As already explained in the text the two methods differ mainly because (1) we use the direct brightness values of the satellite while Erasmus & van Rooyen ([2006]) converted them into temperatures and intepreted the absolute values of the temperatures in terms of height of the infrared emission, using a temperature-height sounding, and then of cloud coverage, and (2) they used a much smaller matrix. The authors pointed out that this technique has some limitations due to a number of effects, for example anomalous trends in temperatures during the night or for some types of clouds (monsoon clouds are an example). While their approach is certainly valid in terms of general physical interpretation, we found more direct and more reliable to work directly in terms of brigthness relative time fluctuations. A deep analysis should be done comparing the results night by night but this is out of the scope of the present thesis.
On the other hand we should take into account possible biases due to our time sampling, because we are measuring the second part of the night only. Our limit was set by the time availability of the Paranal ground log. In particular, phenomena that occurred during the first part of the night were not analyzed in this chapters.
In addition we note that some low level phenomena could be missing (for example local dust clouds, fog...). A further possible bias is due to the satellite spatial resolution, mainly in sites with abrupt topography.
The use of higher resolution satellites, for example the MERIS spectrograph (on board of Envisat) with a spatial resolution of about 1 km, in principle should be better in these cases. Some authors obtained interesting results. For example Kurlandczyk and Sarazin ([2007]) used MERIS at La Silla and Paranal to get cloud coverage and precipitable water vapour and discussed the horography effects. However, in spite of its high spatial resolution MERIS presents some disadvantages compared to GOES. First the temporal coverage is much lower, second, MERIS is working in daytime and it does not give data during the night. As a consequence it can be used as a complement of GOES data to investigate the effects of spatial resolution, but its generalized use should be carefully validated site by site.
Finally, it is interesting to note the percentage differences between the two years, particularly at Mt.Graham, in 2008, the clear and stable nights per-

centage was considerably higher. We note minor differences also in the other sites. These could be a result of the El *Niño* phenomenon and its consequences at different sites.
It is possible to reduce the uncertainty of this methodology using all the available GOES12 IR bands and refining the tuning of the model. We found that using the correlation function from IR satellite data, it is also possible to observe several atmospheric phenomena (i.e. strong winds, damp winds, warm winds, fogs, humidity, dust etc).
A second work on this correlation analysis is in progress to study of the cyclical fluctuations of this function to test the possibility to have a sort of now-casting seeing.
The possible synergy of this model with seeing forecast models may predict the atmospheric changes in the short and long time-scale, allowing the atmospheric conditions for science cases in order to have the best scientific results.

Chapter 6

Detection of subtle phenomena

We describe here two different algorithm introduced to detect perturbations in two cases: low level perturbations located spatially very close to the telescope or very far to the telescope (located at the wedge of the matrix area) that means to have an incoming perturbation.

6.1 Detection of small clouds in the matrix area

In Della Valle et al. [2010] the reflectivity flux has been obtained from the pixel of the matrix centred close to the coordinates of the interested site. To the aim to reduce the instrumental noise and to looking a wider field of view, we decided to replace the 1 pixel flux reflectivity with the mean value of the 1 degree matrix even centred at the coordinates of the interested site, moreover, to better discriminate small clouds distributed in the matrix area, that are missed giving a limitation of the model as described in the previous section, we computed the standard deviation of each matrix. In fact a high standard deviation signifies the presence of perturbations in the wall area. We are able also to see incoming clouds approaching to the edge of the matrix area Figures 6.1 and 6.2 show two examples in which the average value of the matrix in both the figures correspond to clear nights, but the standard deviation of Figure 6.2 is high, showing a non real flat distribution of the satellite counts. This is the case of incoming perturbation to the telescope site. Considering the standard deviation, we obtain the following classification:

- Standard deviation$(T_B) \leq 2\sigma \Longrightarrow$ Clear
- Standard deviation$(T_B) > 2\sigma \Longrightarrow$ Subtle Phenomena

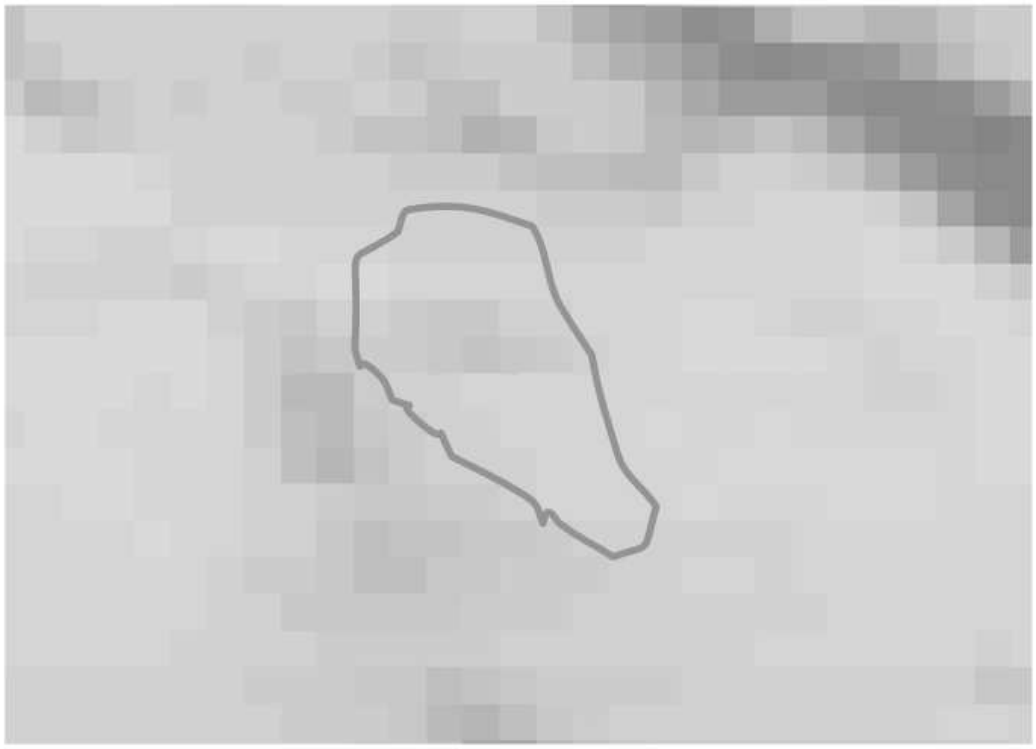

Figure 6.1: Example of a low standard deviation of pixel array.

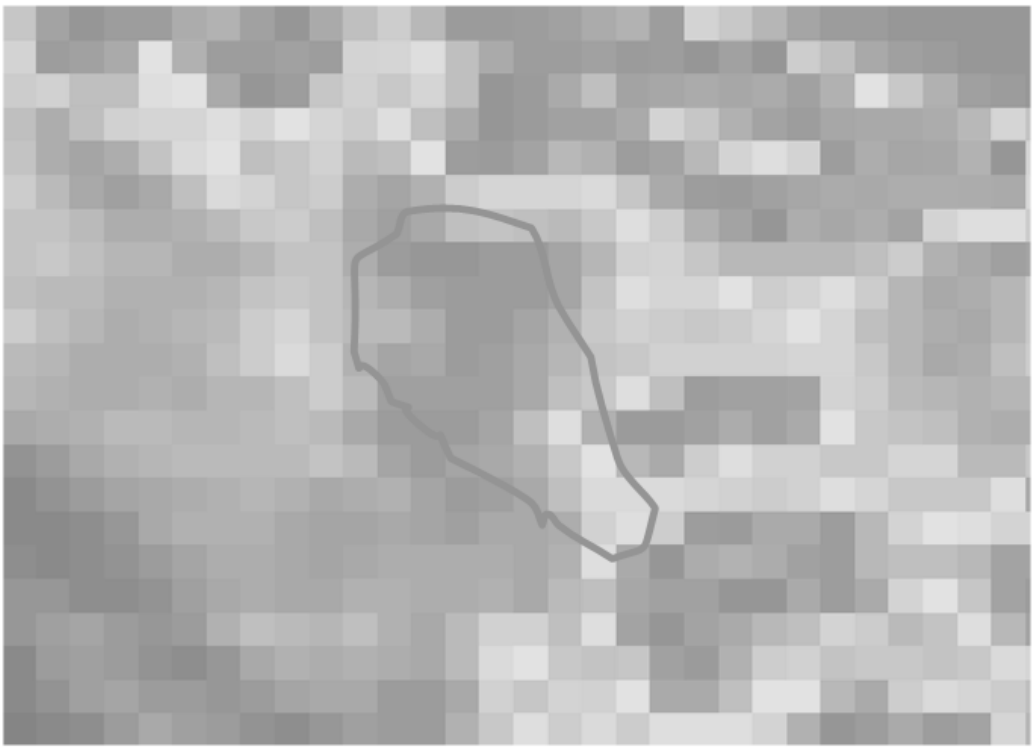

Figure 6.2: Example of a high standard deviation of pixel array.

Figure 6.3: Remote Sounding between the average and the single pixels: example of a large difference between the average and the single pixels.

6.2 Detection of local phenomena

Finally, to better detect the presence of local phenomena close to the telescope, we introduce the difference between the mean matrix reflectivity and the single pixel reflectivity through the formula:

$$I_{RS}(Matrix/1Pixel) = \left|\overline{I_{\lambda_4}} - I_{\lambda_4(1Pixel)}\right| \tag{6.1}$$

A high value of I_{RS} shows the presence of a perturbation, even at low S/N level, not detectable using the simple standard deviation and the matrix average due the the high number of averaged pixels.
In particular, we use this mathematics classification:

- $\left|\overline{I_{\lambda_4}} - I_{\lambda_4(1Pixel)}\right| \leq 2\sigma \Longrightarrow$ Clear
- $\left|\overline{I_{\lambda_4}} - I_{\lambda_4(1Pixel)}\right| > 2\sigma \Longrightarrow$ Subtle Phenomena

Figure 6.3 represent one example of average corresponding to clear nights. In this case, the $Matrix/1Pixel$ RS shows the presence of local stationary phenomena not detected by the mean value of the matrix. By the use of both the $Matrix/1Pixel$ and the standard deviation of each data we can better to detect local phenomena and thin clouds as shown in Figure 6.4 in La Palma. In fact you see that the plot of B4 band evidenced by the circle is flat, typical of clear sky, the bottom of Figure 6.4 plotting $Matrix/1Pixel$ difference show variations indicating the presence of local phenomena. A check with the logbooks describe the presence of high humidity and ice in this nights. We stress that these cases are rare, in fact table 6.1 shows the statistical result of this analysis for the 2009 at Paranal and La Palma. It is given the mean monthly percentage of clear nights and the fraction of the clear nights with low level phenomena. We see that only the 1% of the 91% of clear night at Paranal is affected by low level phenomena, to compare with the 3% of the 67% at La Palma. In both cases is a very low number. At Paranal May shows an high number of SUB_P phenomena. The check with the log gives high wind value coming form the see, that means high humidity justifying the high satellite value. Figure 6.5 shows the amount of clear time at La Palma for the 2009, in gray it is shows the percentage of subtle phenomena.

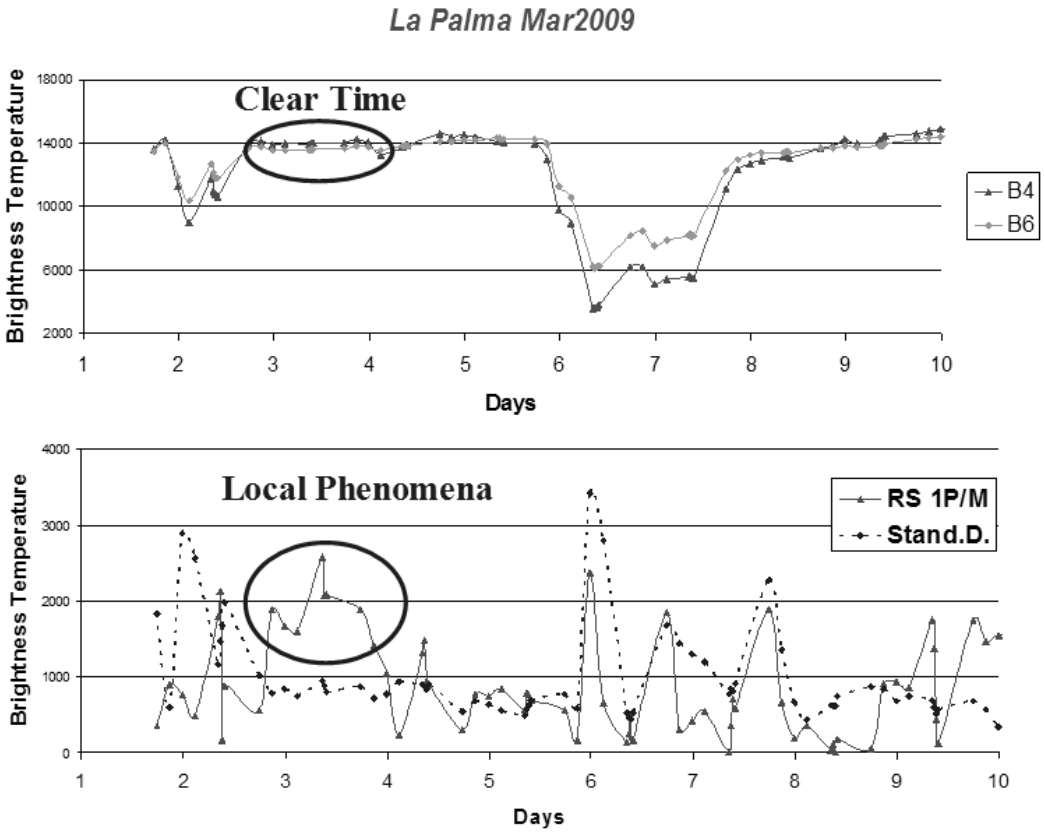

Figure 6.4: The B4 trend (upper panel) shows no indicates while the $RS_{Matrix/1Pixel}$ (bottom panel) indicates the presence of local phenomena: the logbooks in fact describe the presence of high humidity and ice. The brightness temperature is expressed in number of satellite counts as extracted with McIDAS-V program.

Table 6.1: Satellite Mean Monthly Percentage. Paranal and La Palma 2009. Subtle Phenomena (SUB_P).

	Paranal		La Palma	
	Clear Time	SUB_P	Clear Time	SUB_P
January	99.3	1.0	58.3	3.2
February	99.4	1.5	53.7	4.9
March	97.0	1.3	64.2	3.2
April	96.8	0.9	82.0	3.0
May	89.0	2.1	73.3	2.1
June	80.1	0.9	75.9	2.5
July	79.5	1.6	82.9	3.3
August	90.5	1.8	86.5	3.0
September	85.3	0.3	60.2	2.2
October	85.7	0.7	69.2	2.5
November	99.2	0.0	66.2	2.8
December	98.3	0.4	32.2	3.0
Mean	90.8	1.0	67.1	3.1

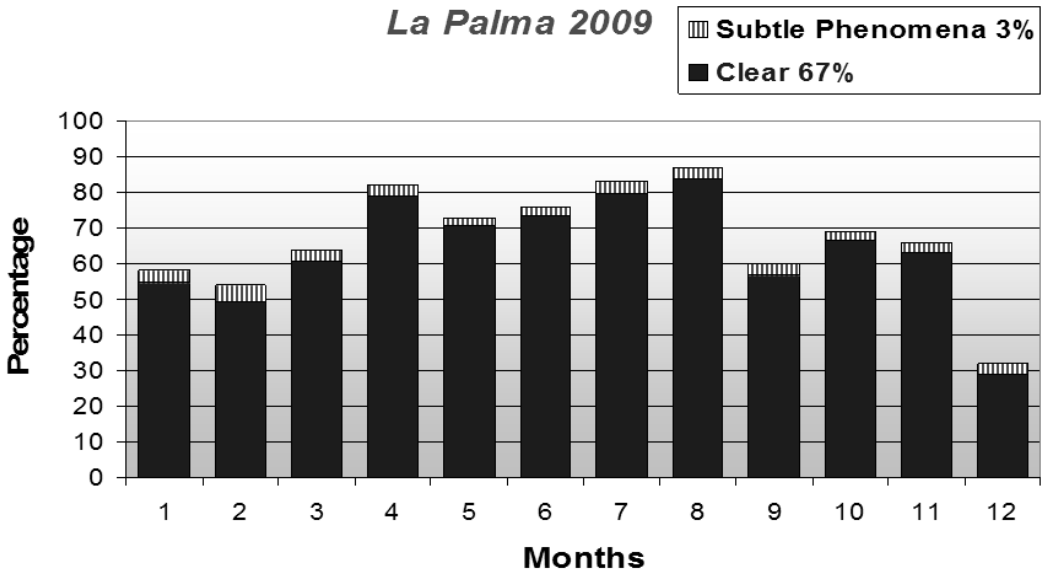

Figure 6.5: Subtle Phenomena. La Palma 2009.

Chapter 7

Seeing evaluation from satellite based data

In the previous chapters we have seen how the atmospheric correlation function is related to the seeing (see Section 3.6). In this chapter we describe a new model for the seeing satellite calculation. We also show how the use of the matrix can detect atmospheric suble phenomena (see Section 6). Finally we show a new study for the short-term statistical forecast of the night quality (see Section 8.1).

We present for the first time a new method to estimate the seeing using remote sounding from the IR night time data of the GOES 12 satellite. We discuss the derived correlation between the ground data and the satellite derived values from the analysis of the sites located at Cerro Paranal (Chile) and Roque de los Muchachos (Canary Islands, Spain). We get a ground-satellite correlation percentage of about 90%. Finally, studying the correlation between the afternoon data and the following night, we are able to provide a forecast of the photometric night quality. We stress that the model has only been tested for sites of Paranal and La Palma. It has theoretical hypotheses, but at the moment the seeing calculation remains empirical.

The capability to optimize the scientific requirements to the observing conditions is a challenging effort crucial to improve the performances and to increase the final efficiency of the system telescope-instrumentation, mainly for very large telescopes. The first parameter needed for this goal is the knowledge of the usable nights. In the last decades this evaluation suffered of biases due to personal judgements, because they were based on visual inspection. A great improvement has been obtained with the use of satellite data. The second important parameter in the site selection and in the site characterization, is the image quality because, as well known, it affects the

scientific quality of the results in many fields of the astronomical research. Since the first campaigns for the site selection, the criteria were based simply on the direct analysis of the size of the stellar images. Now, with the progress of the knowledge in this area, we know that the seeing is characterized by multiple parameters and affected or simply linked to several local and wide scale conditions, such as the external air temperature and gradients (Lombardi et al., ([2006]), hereafter Paper I), pressure, wind velocity (Lombardi et al., ([2007]), hereafter Paper II) and a link between these parameters and the optical turbulence (Cavazzani et al. ([2011])). It is also crucial to know the evolution of the seeing with the time in short and long time scale, mainly for the future giant telescopes, for the optimization of the flexible scheduling. In general the testing campaigns of the past were expensive and time consuming and limited to a few preselected sites. The use of the archive satellite data, instead, is of a great importance because it allows to simultaneously investigate several sites on a time base of many years. A quantitative survey of cloud coverage and water vapor content above several astronomical sites have been recently obtained using both satellite and ground based data by Erasmus and van Rooyen ([2006]), Erasmus and Sarazin ([2002]). They have been among the first to demonstrate the capability of the satellite data to give the amount of useful nights. Della Valle et al. ([2010], Paper III) used a similar analysis and, from independent data, found an agreement of the amount of clear nights between satellite and ground based data at La Palma of about 80%. An evolution of this analysis is presented in Cavazzani et al. ([2011]) where we used a more sophisticated method and we introduced the concept of satellite stable night which is the best approximation of the concept of photometric nights. In this chapters we present for the first time an estimation of the seeing obtained using the satellite remote sounding. We analyze the correlation between ground based seeing and the satellite based seeing. This analysis is applied to two very important astronomical international sites such as Cerro Paranal (Chile) and Roque de Los Muchachos (La Palma, Canary Islands, Spain) in order to validate the code in two very different climatic and topographic conditions. The location of the two sites is presented in Fig. 7.1. La Palma and Paranal are two sites in which the astronomical community built several facilities thanks to the good sky condition, moreover the community is strongly interested to maintain a high performance of the instrumentation. For this reason several authors focused the attention in the characterization of these two sites (Murdin [1985], Sarazin [2004], Varela et al. [2008], ecc.).

The ESO staff was the pioneer of this topic and the long record of data collected at Paranal are useful tools to analyse the connection between astrophysical and physical environmental conditions. Differences with La Palma

microclimate have been discussed in Paper I, Paper II, and Paper III. Paper I shows a complete analysis of the vertical temperature gradients and their correlation with the astronomical seeing, Paper II shows an analysis of the correlation between wind and astronomical parameters as well as the overall long term weather conditions at La Palma. A statistical fraction of clear nights from satellite has been derived in Paper III using a basic approach to test the ability of the satellite to select clear nights.
The main conceptual difference between Erasmus & van Rooyen ([2006]) analysis and Paper III is that they used the radio sounding vertical profile temperature as absolute reference to be compared with the brightness IR temperature measured by the satellite, while we used relative deviations from the bulk of data to detect the presence of clouds. In particular we selected two bands sensitive to the clouds and plotted one band versus the other. The calibration of the plot gives the statistical fraction of usable nights. The use of the two bands separately is efficient to sense thick clouds, but presents some limits in case of partial coverage or thin clouds. For this reason we have refined the analysis introducing a new band sensitive to the local phenomena and introducing a mathematical code to correlate the three bands. This analysis discriminates with success changes in air masses showing also a first connection with seeing variations, as presented in Cavazzani et al. ([2011]). In this thesis, to better analyse the correlation between satellite reflectivity and ground based image quality at La Palma and Paranal, we have used ground and satellite based data sampling the year 2009. We have used GOES satellite, to have homogeneous results with the previous results and easy to compare and discuss. Table 7.1 shows the geographic position and view angle of the satellite for each site.

7.1 Satellite and ground based data

In this analysis we have compared satellite data with the image quality in term of FWHM obtained using the differential image motion monitoring (DIMM) at the two sites. Data at the Observatorio del Roque de los Muchachos (ORM) are derived from the Robotic Differential Image Motion Monitor (known as RoboDIMM [1]) of Isaac Newton Telescope (INT). The INT RoboDIMM, like all classical DIMMs, relies on the method of differential image motion of telescope sub-apertures to calculate the seeing Fried parameter r_0. RoboDIMM forms four separated images of the same star, and measures image motion in two orthogonal directions from which it derives four

[1] See http://catserver.ing.iac.es/robodimm/

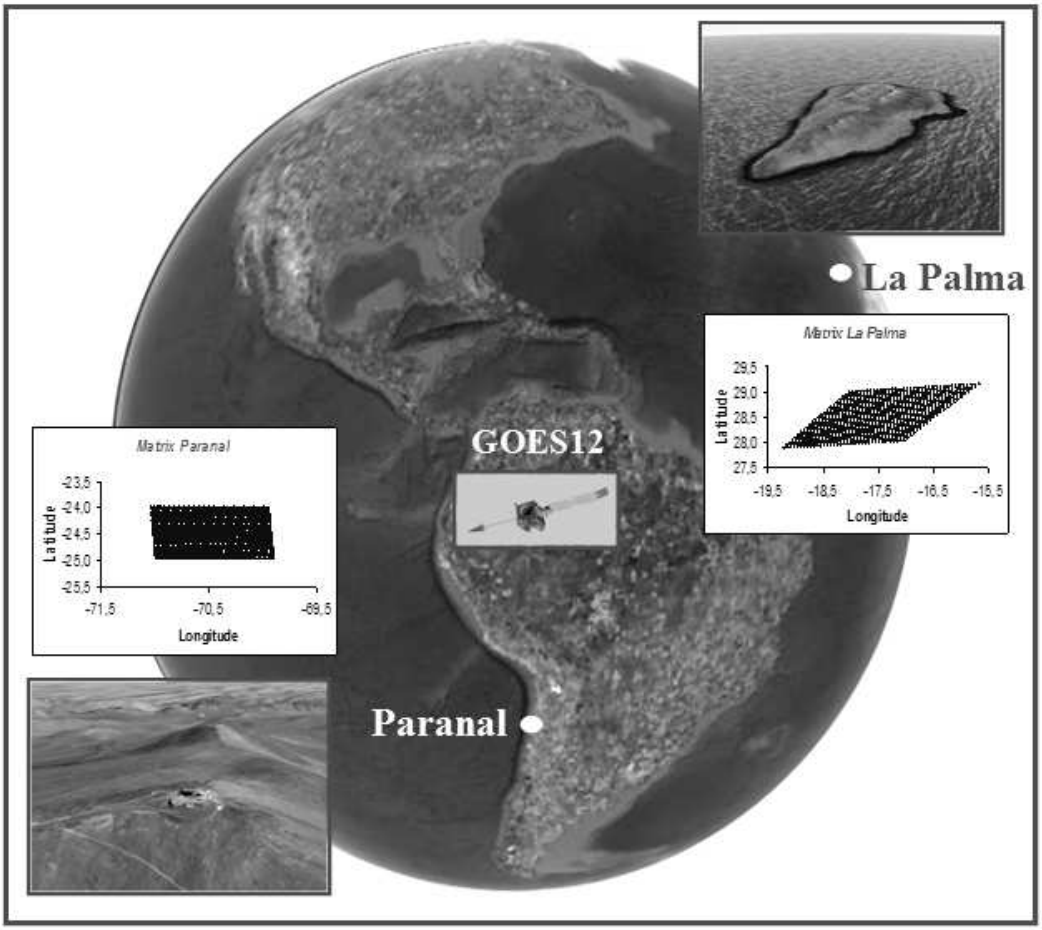

Figure 7.1: Location of the two sites involved in the analysis. As seen in the inserts the selected sites presents very different topographic conditions: La Palma is a sharp island, Paranal is isolated peaks over the Atacama's desert. The position of GOES12 satellite projected on the map. Figure also shows the comparison of one matrix at Paranal and La Palma. The deformation is a result of the satellite observation angle.

Table 7.1: Geographic characteristics of the analyzed sites and GOES12 satellite. The view angle is obtained through the formula $\theta = \sqrt{(\Delta LAT)^2 + (\Delta LONG)^2}$.

site	LAT.	LONG.	Altitude Km	View Angle
Paranal	$-24°37'$	$-70°24'$	2.630	$25°00'$
La Palma	$+28°45'$	$-17°52'$	2.363	$64°10'$
GOES12	$+0°00'$	$-75°00'$	35800	

simultaneous and independent estimates of the seeing. The data interpretation makes use of the Sarazin and Roddier's DIMM algorithm described in Sarazin & Roddier ([1990]), based on the Kolmogorov theory of atmospheric turbulence in the free atmosphere. At the present we do not have other seeing data to check possible local differences. But la Palma is the only site having several DIMM distributed along the top of the mountain. We are planning to follow this analysis using all the available DIMM data to check possible local differences for a better characterization of the site and to correlate direct measurements such as $C_n^2(h)$ with satellite seeing. The seeing data at Paranal are obtained measuring the seeing of the DIMM at VLT observatory. The file contains also measurements of the flux of a reference star, in this way the flux of the star can trace the presence of clouds. The ground based classification of the night quality instead has been done using the night observing log of each telescope.

In this analysis we have used GOES satellite because it is able to detects the infrared (IR) night time emitted radiation permitting to compare in a simultaneous way ground and satellite data. A detailed discussion of the performance of this satellite is presented in Cavazzani et al. ([2011]). The main advantage of GOES with respect other satellite is that GOES is able to observe the full Earth disk and it have on board an imager with five channels allowing the collection of five simultaneous images of almost half of the Earth hemisphere. Our choice to use the IR channels is because they allow the detection of the thermal radiation emitted during the night from different atmospheric layers and/or from the soil. An appropriate choice of the wavelength allows to choose the optimal layer emission height above the site. If it occurs well above the soil surface, the signal becomes independent of the specific soil properties and of low level conditions. Phenomena occurring below the selected site (fog, low clouds...) are also avoided. In some sites, for example at La Palma, this aspect is of crucial importance.

Table 7.2: Characteristics of the GOES12 used bands and resolution at Nadir.

	Window	Passband $[\mu m]$	Resolution [km]
BAND3	H_2O	$6.50 \div 7.00$	4
BAND4	IR	$10.20 \div 11.20$	4
BAND6	CO_2	13.30.	8

For the purposes of this work we used GOES 12 equipped with the imager and we have analysed the year 2009. We have selected the water vapour channel (B3 band) centred at 6.7 μm, able to detect high altitude cirrus clouds, the infrared channel (B4 band) centred at 10.7 μm, able to detect middle level clouds, and the CO_2 band (B6 band) centred at 13.3 μm, able to sense small particle such as fog, ash and semi-transparent high clouds. For each site we have identified and extracted a sub-image of $1^\circ \times 1^\circ$ having the central pixel close to the coordinates given in Table 7.1. We have seen that the use of the matrix is justified by the high correlation with the single pixel and reduces the satellite noise and also allows us to observe the entire sky above the site.

Table 7.2 shows the main characteristics of the selected bands. For each night we have extracted the observations at different hours in local time: at 17:45, 20:45, 23:45, 02:45, 05:45, 7:45, 8:45 and 9:45. The evaluation of the amount of useful hours is done using all the night but 17:45 and 9:45. We have used both the brightness temperature at 17:45 and 9:45 to check a possible day-night correlation. The last column of Table 7.1 shows the satellite view angle. The insert in Figure 7.1 shows the two different projections obtained from each acquisition at La Palma and Paranal.

In the previous chapters there is an exhaustive description of the mathematics approach and of the night classification (see Table 4.3).

7.2 Temporal Satellite classification

To have reliable prediction of the time quality, we have used a high temporal resolution using for each night the following series of data: 20:45, 23:45, 2:45, 5:45, 7:45, 8:45. Using the brightness temperature obtained for each considered hours we have obtained the monthly atmospheric correlation function. Figures 7.3 and 7.4 show the plot of the obtained temporal emissivity of B4 band vs B6 for the 2009 at Paranal and La Palma. Nights are classified according to the comment of the observing logs. Clear time presents high values

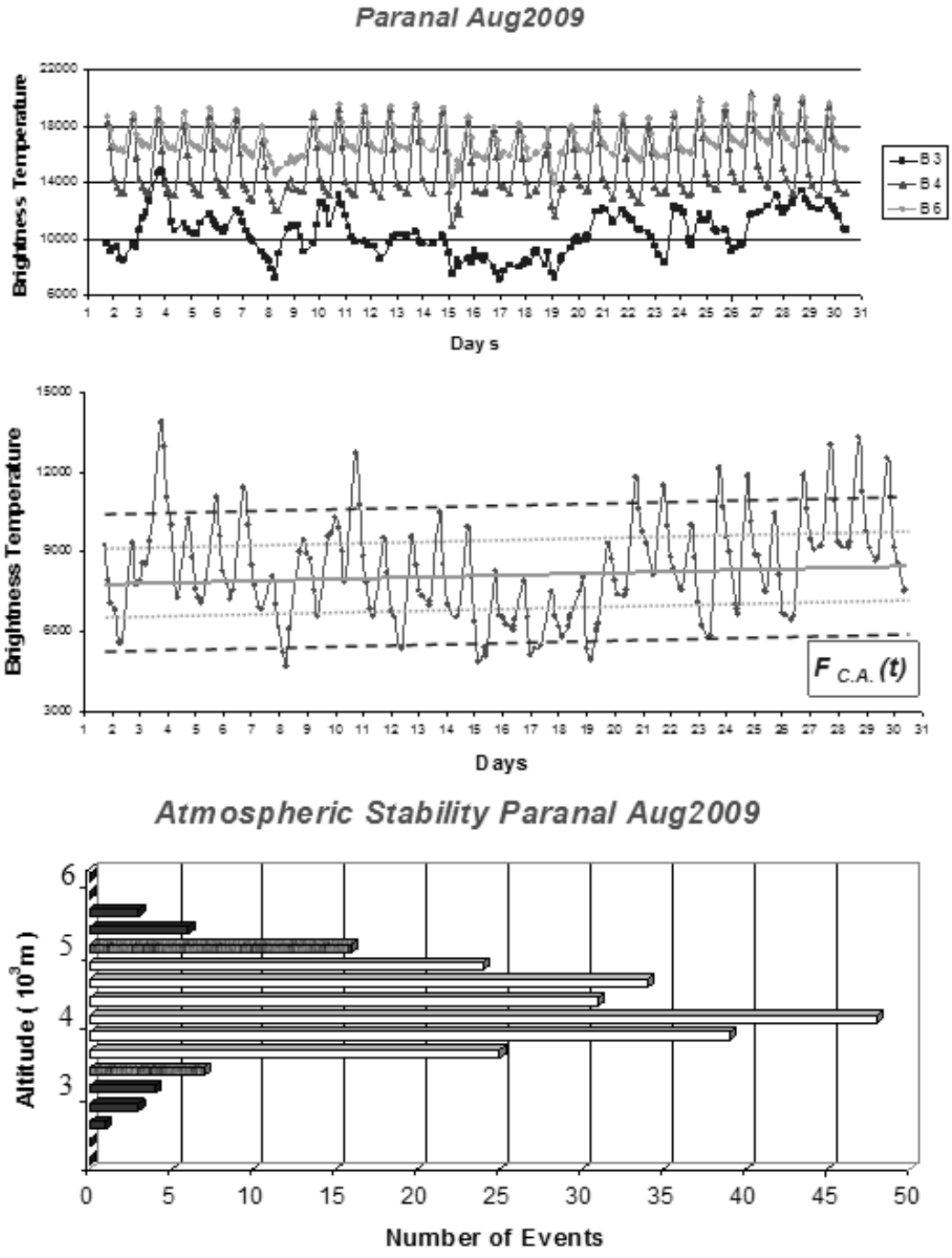

Figure 7.2: Atmosferic Correlation Function at Paranal, August 2009. Top figure shows the monthly plot of the three used bands.The central plot shows the $F_{C.A.}$ of August, the solid gray line is the $F_{C.A.}(t)$ linear regression. The brightness temperature is expressed in number of satellite counts as extracted with McIDAS-V program. The bottom part shows the distribution of the clear and stable nights as a function of the sensed height.

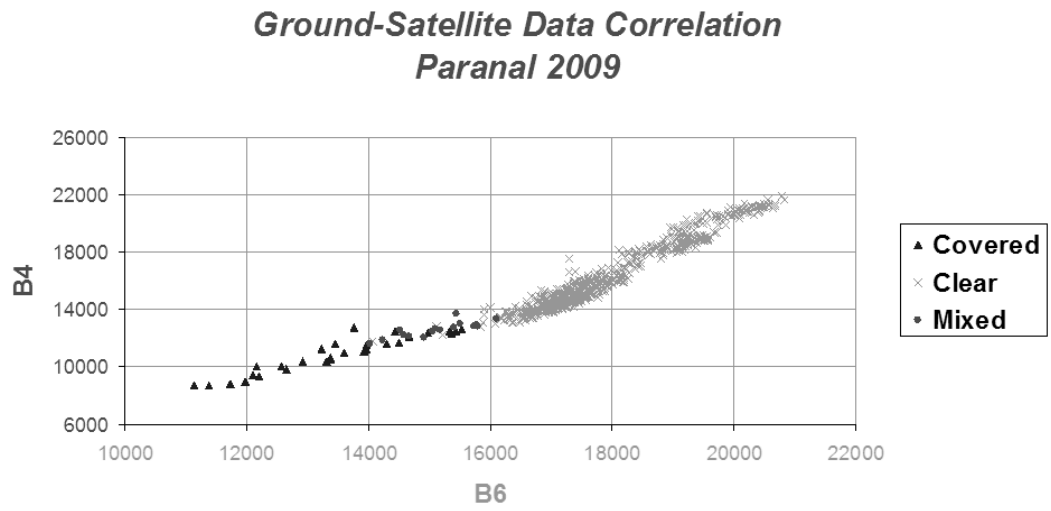

Figure 7.3: Temporal distribution of GOES12 B4 and B6 band emissivity at Paranal in 2009. Sky quality classification has been carried out using the Paranal log.

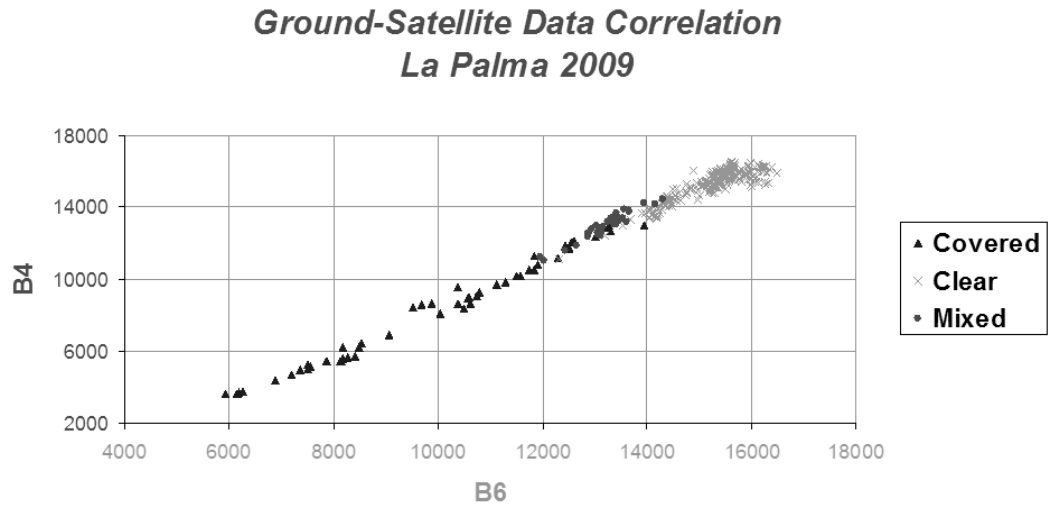

Figure 7.4: Temporal distribution of GOES12 B4 and B6 band emissivity at La Palma in 2009. Sky quality classification has been carried out using the La Palma log.

Table 7.3: Temporal data analysis of Clear/Mixed/Covered time at Paranal and La Palma in 2009.

	Ground			Satellite		
	Clear	Mixed	Covered	Clear	Mixed	Covered
Paranal	90.1%	2.2%	7.8%	90.8%	2.6%	6.6%
La Palma	65.8%	5.0%	29.3%	67.0%	4.5%	28.5%
	Paranal			La Palma		
Uncertainty	$\Delta_{Clear/Mixed}$	$\Delta_{Clear/Covered}$	$\Delta_{Mixed/Covered}$	$\Delta_{Clear/Mixed}$	$\Delta_{Clear/Covered}$	$\Delta_{Mixed/Covered}$
Percentage	1.2%	0.4%	0.8%	1.3%	0.5%	0.8%

of emissivity at both sites. As in Paper III, the classification of satellite time quality is done assuming that the maximum monthly brightness temperature in B4 band (T_B^{Max}) occurs in clear condition. The classification is described in the Table 4.3. Table 7.3 shows the obtained percentage of clear, mixed and covered nights at Paranal and at La Palma for the year 2009 using all the algorithm previous described. The ground based classification is derived from the comments of the night logbook. We found a very good agreement in both the two sites between ground and satellite data. The last row of Table 7.3 shows the percentage of accuracy to associate to each obtained fraction of nights. The uncertainty is computed as follows:

- $\Delta_{Clear/Mixed} \Rightarrow$ Clear/Mixed Uncertainty
- $\Delta_{Clear/Covered} \Rightarrow$ Clear/Covered Uncertainty
- $\Delta_{Mixed/Covered} \Rightarrow$ Mixed/Covered Uncertainty

Usually the quality of the ground based clear nights is divided between photometric and spectroscopic nights. Also for the satellite classification we have introduced a similar definition introducing the concepts of stable night (photometric) and clear night (spectroscopic). Considering the value of the $F_{C.A.}(t)$ linear regression $T_B^{Trendline}$ we define:

1. $T_B^{Trendline} \Rightarrow$ Brightness temperature of the $F_{C.A.}(t)$ linear regression computed in one month
2. $T_B \Rightarrow$ Brightness temperature of the $1^\circ \times 1^\circ$ matrix in one hour

Table 7.4 shows the obtained satellite mean monthly percentage of clear and stable time at Paranal and la Palma.

Figures 7.5 and 7.6 show the distribution of the amount of clear, stable and covered time at Paranal and la Palma for the year 2009 obtained from the $F_{C.A.}(t)$. The maximum of the distribution shows the sensed height and it gives the height in which occur the atmospheric phenomena. Figure 7.7

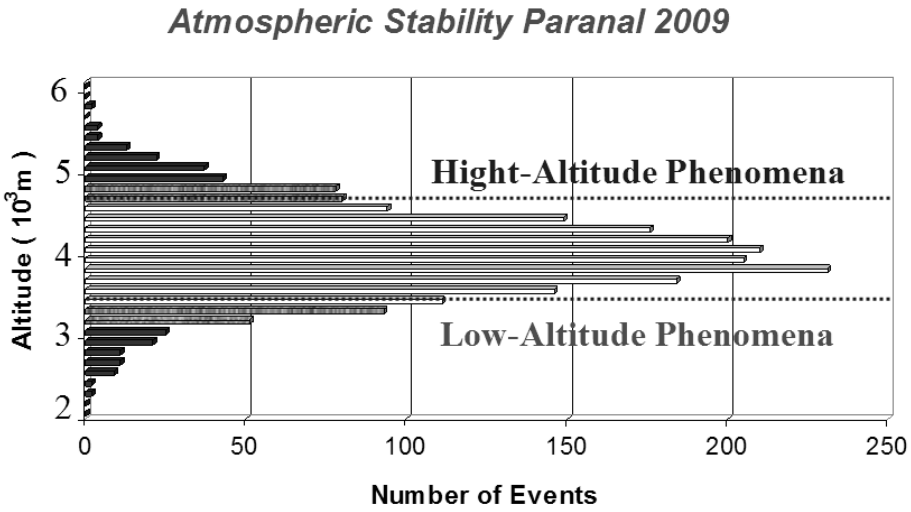

Figure 7.5: Histogram of annual atmospheric stability at Paranal. Light-gray bars represent the stable nights, gray bars clear but unstable nights, black bars the nights covered.

shows the monthly distribution of the clear and stable nights at Paranal for the considered year. We see that during the winter months is low the percentage of stable time and the night is mostly only clear.

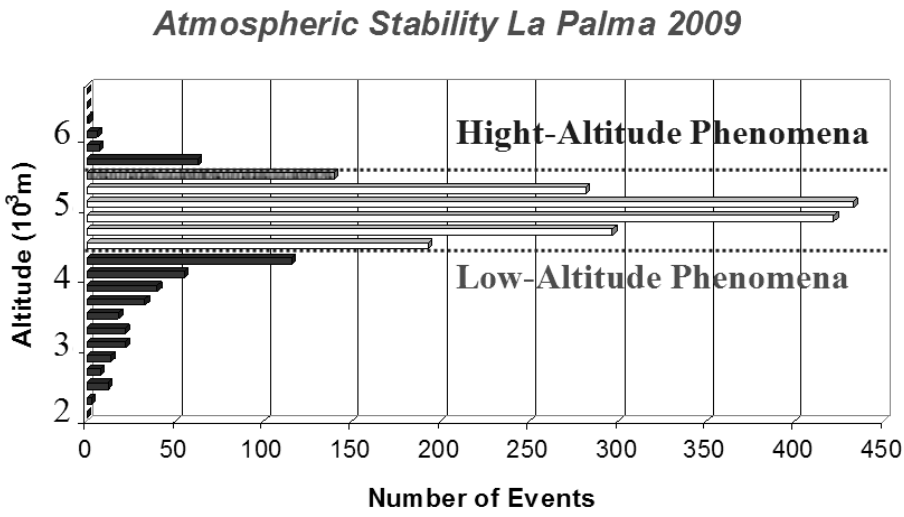

Figure 7.6: Histogram of annual atmospheric stability at La Palma. Light-gray bars represent the stable nights, gray bars clear but unstable nights, black bars the nights covered.

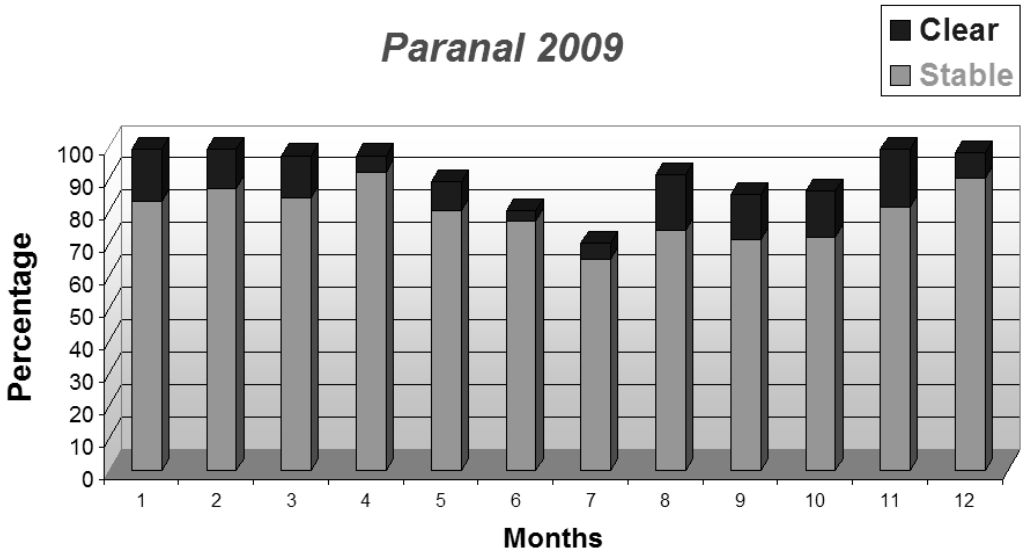

Figure 7.7: Clear and stable night fractions at Paranal 2009 from GOES12 satellite.

Table 7.4: Satellite Mean Monthly Percentage for the year 2009.

	Paranal		La Palma	
Paranal	Clear Time	Stable	Clear Time	Stable
January	99.3	83.3	58.3	57.6
February	99.4	86.6	53.7	48.8
March	97.0	84.4	64.2	57.6
April	96.8	92.2	82.0	78.8
May	89.0	79.7	73.3	64.0
June	80.1	76.7	75.9	72.3
July	69.5	64.9	82.9	75.6
August	90.5	74.0	86.5	76.0
September	85.3	70.9	60.2	56.8
October	85.7	71.7	69.2	64.7
November	99.2	80.8	66.2	59.2
December	98.3	89.8	32.2	30.7
Mean	90.8	79.6	67.1	61.6

Table 7.5: Mathematical and statistical uncertainties of the model in 2009 at Paranal and La Palma.

Site	Δ_{Total}	$N(G;S)$	$\Delta_{Statistical}$
Paranal	1.4%	1510	0.05%
La Palma	1.5%	1510	0.06%

Table 7.6: Satellite FWHM at Paranal for the year 2009.

Months	$FWHM_{Sat}^{Mean}$	$FWHM_{Ground}^{Mean}$	COR_{Coef}
January	0.9	0.9	0.91
February	0.8	0.8	0.97
March	0.8	0.8	0.88
April	0.7	0.7	0.93
May	0.8	0.8	0.93
June	0.8	0.8	0.84
July	0.8	0.8	0.79
August	0.9	0.9	0.92
September	0.9	0.9	0.96
October	0.8	0.9	0.84
November	0.8	0.9	0.95
December	0.8	0.8	0.95

Table 7.7: Satellite FWHM at La Palma for the year 2009. We have calculated the correlation coefficients only for the months in which the RoboDIMM gives us values for more than ten nights. Moreover the mean seeing only refers to the clear time due to the fact that in the covered time the RoboDIMM does not work.

Months	$FWHM_{Sat}^{Mean}$	$FWHM_{Ground}^{Mean}$	COR_{Coef}
January	-	-	-
February	-	-	-
March	0.9	1.0	0.89
April	1.0	1.0	0.91
May	0.8	0.8	0.94
June	0.9	0.8	0.93
July	0.9	0.9	0.92
August	0.8	0.7	0.92
September	0.8	0.7	0.95
October	-	-	-
November	-	-	-
December	-	-	-

Chapter 8

Satellite calculation of seeing

In Cavazzani et al.([2011]) we shown that the adopted code is able to discriminate with success variations of the atmospheric stability function ($F_{C.A.}(t)$) with the optical turbulence showing the first connection between $F_{C.A.}(t)$ and seeing. In this thesis we are going deeper in this analysis and, to better analyse the correlation between satellite reflectivity and ground based image quality at La Palma and Paranal, we have used ground and satellite based data sampling the year 2009. In particular we introduce for the first time the concept of satellite seeing. The $F_{C.A.}(t)$ measure the temperature in different atmospheric layers, and as well as the ground based C_T^2 is linked to the r_0 and to the FWHM, it is possible to derive a satellite based C_T^2, and consequently C_n^2. The zero point is given empirically in this analysis. Using the basic formulae of the seeing theory such as Fried's radius r_0 we have:

$$r_0 = \left[0.423 \cdot \frac{4\pi^2}{\lambda^2} \cdot \frac{1}{cos(\theta_{zen})} \int C_n^2 \cdot dz\right]^{-\frac{3}{5}} \tag{8.1}$$

where C_n^2 is the refractive index structure parameter:

$$C_n^2 = \left[80 \cdot 10^{-6} \frac{P}{T}\right] \cdot C_T^2$$

The full width at half maximum is given by the following formula:

$$FWHM = 0.98 \frac{\lambda}{r_0} \tag{8.2}$$

While the satellite FWHM is obtained through an our empirical model. If we assume:

$$\left|T_B - T_B^{Trendline}\right| \propto C_T^2 \propto C_n^2$$

we can replace the C_n^2 value in the Equation 8.1 obtaining a satellite r_0 calculation:

$$r_{0,Sat} = \left[0.423 \cdot \frac{4\pi^2}{\lambda^2} \cdot \Lambda(\theta) \cdot \frac{\left| T_B - T_B^{Trendline} \right|}{z} \right]^{-\frac{3}{5}} \tag{8.3}$$

Finally, using this value we get the formula for satellite FWHM:

$$FWHM_{Sat} = 0.58 \cdot \lambda^{-\frac{1}{5}} \cdot \left[4\pi^2 \cdot \Lambda(\theta) \cdot \frac{\left| T_B - T_B^{Trendline} \right|}{z} \right]^{\frac{3}{5}} \tag{8.4}$$

where $\Lambda(\theta)$ is an empirical constant defined by the formula:

$$\Lambda(\theta) = \frac{10^{-12}}{cos\theta} \tag{8.5}$$

where θ is the satellite angle of view.
Figure 8.1 shows the comparison between ground based FWHM and satellite based FWHM computed in the same hours. We note the very good agreement between the two set of data. Figure 8.2 shows the dispersion of this correlation and its linear regression. A tentative physical interpretation of our correlation could be related to the Richardson number R_i dependent on the vertical temperature gradient. Tables 8.1 and 8.2 show the comparison between the seeing as given by the ground and those computed by satellite using the equation 8.4. We make the following observations to discuss the obtained values: $FWHM_{Ground}^{Mean}$ values at Paranal are the DIMM data and not the VLT values; at La Palma instead we have calculated the correlation coefficients only for the months in which the RoboDIMM gives us values for more than ten nights. Moreover the mean seeing only refers to the clear time due to the fact that the RoboDIMM does not work during cloudy nights.

8.1 Temporal forecasting seeing analysis

In this section we analysed for the first time the possibility to give a forecasting value of the seeing a few hours before starting the observations. We have proceeded in two different ways to check the capability and the best procedure. In the first test we have correlated the brightness temperature obtained from the value at 9:45 with the brightness temperature obtained using the values of the nights before.

In the second test we have correlated the brightness temperature obtained from the afternoon value at 17:45 and the same night time. Figure 8.3 shows

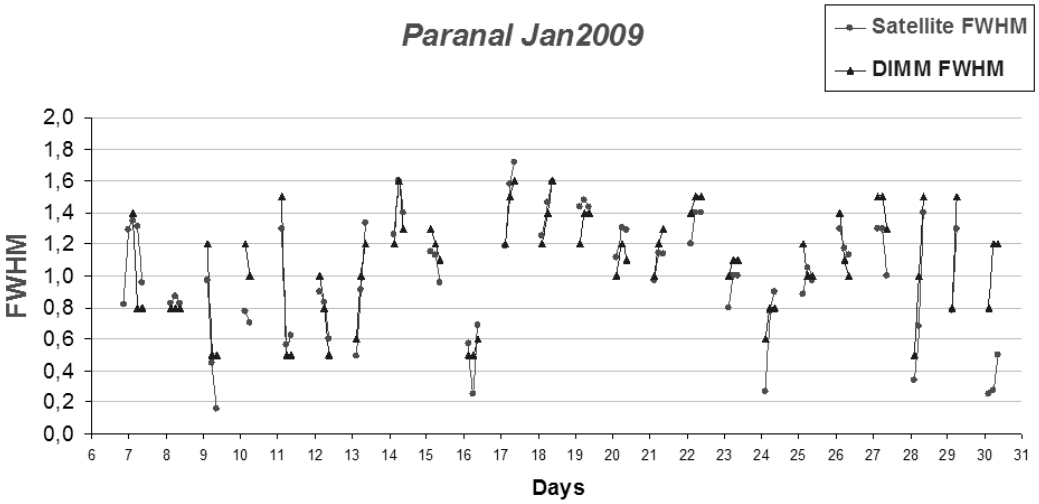

Figure 8.1: Ground Data-Satellite Data Correlation. Comparison between the FWHM calculated from the ground and the satellite FWHM. Paranal, January 2009 (Correlation Coefficient= 0.91). The satellite FWHM is calculated through the Formula 8.4.

Table 8.1: Forecast at Paranal and at La Palma for the year 2009. $A \rightarrow N$ is the correlation between the afternoon and the next night and $N \rightarrow M$ is the correlation between the morning and the night before.

		Paranal		La Palma	
Months	Days	$A \rightarrow N$ Correlation	$N \rightarrow M$ Correlation	$A \rightarrow N$ Correlation	$N \rightarrow M$ Correlation
January	31	100.0	100.0	93.5	96.8
February	28	96.4	100.0	85.7	92.9
March	31	96.8	100.0	90.3	93.5
April	30	96.7	100.0	90.0	96.7
May	31	100.0	96.8	100.0	96.8
June	30	100.0	93.3	90.0	90.0
July	31	93.5	93.5	96.8	96.8
August	31	96.8	96.8	96.8	100.0
September	30	100.0	100.0	96.7	100.0
October	31	100.0	100.0	96.8	96.8
November	30	100.0	100.0	100.0	100.0
December	31	96.8	96.8	96.8	96.8

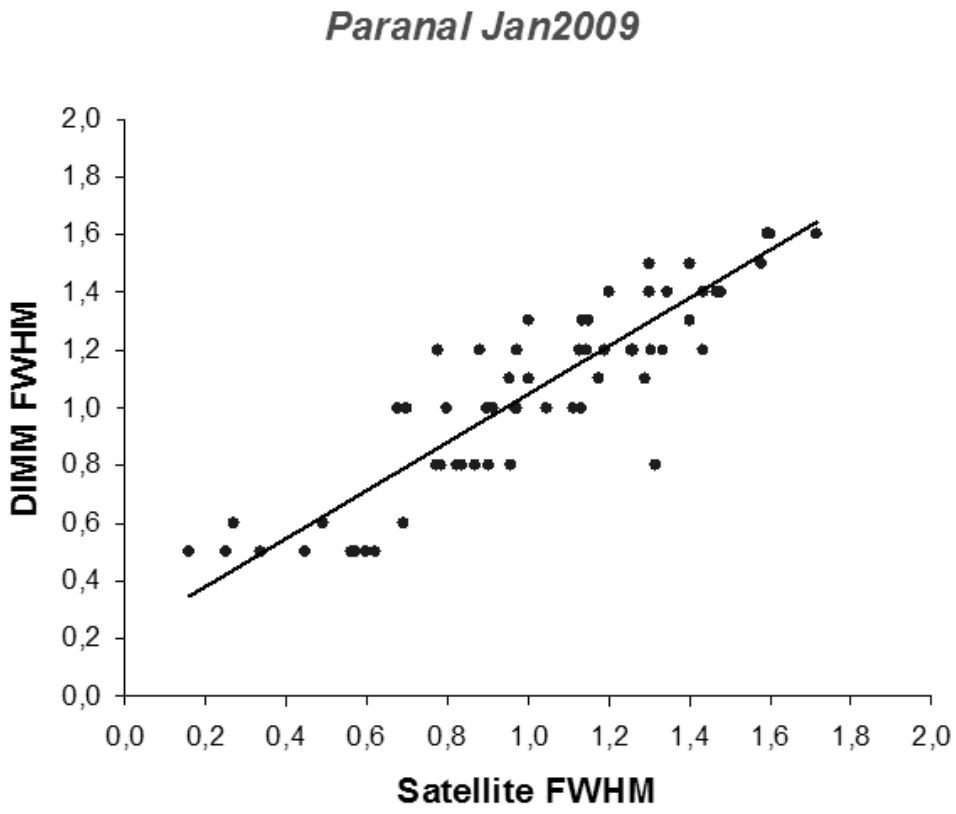

Figure 8.2: Ground Data-Satellite Data Correlation. Figure shows the dispersion of this correlation and its linear regression. Paranal, January 2009 (Correlation Coefficient= 0.91).

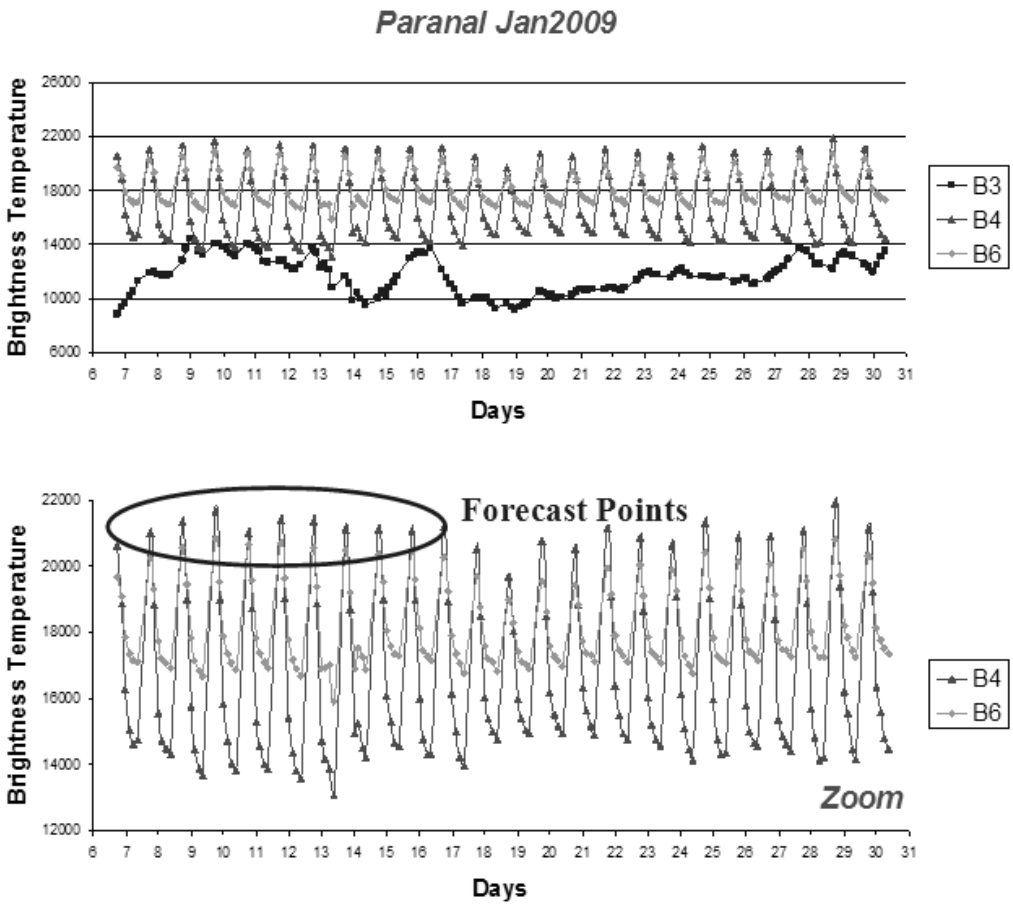

Figure 8.3: GOES 12 emissivity in B3, B4, B6 bands (upper panel) at Paranal for January 2009. Botton panel shows the B4, B6 vertical scale zoom. The brightness temperature is expressed in number of satellite counts as extracted with McIDAS-V program.

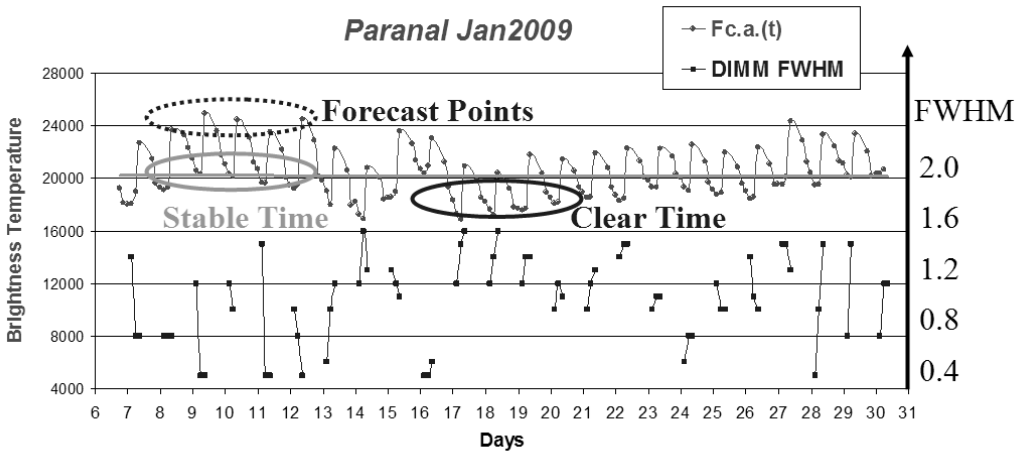

Figure 8.4: Figure shows the trend of the $F_{C.A.}(t)$. In this function we have highlighted the new points used for the night quality forecast (Forecast points). Through the position of these points we can predict whether the night will be stable (Stable time) or clear (Clear time). In fact, Figure also shows the DIMM FWHM values at Paranal (drawn in black). We note that at these stable time points we have low seeing values, conversely we have high seeing values at clear time points (The ordinate on the right shows the DIMM FWHM values). The brightness temperature is expressed in number of satellite counts as extracted with McIDAS-V program.

the monthly distribution of the three bands at Paranal for January 2009 (upper panel) and the zoom (bottom panel) in which is possible to see the new day point used for the forecasting seeing. We see that in case of hight day values the night after is stable (photometric night). It is interesting to note that in this analysis we are able to give a percentage of useful nights instead of useful time. Table 8.1 shows the monthly values of the derived correlation at the two sites. Column 1 of tables shows the month, column 2 shows the number of used days, column 3 shows the afternoon to night correlation ($A \rightarrow N$ is the correlation between the afternoon and the next night) and column 4 shows the night to morning correlation ($N \rightarrow M$ is the correlation between the morning and the night before). For our analysis we are interested to column 3 that give the correlation of all the available day-night data. We see that at Paranal and at La Palma the correlation decrease during the winter months. Tables 8.2 and 8.3 instead show the period of the day in which the meteorological variation occurred. Column 1 shows the month, column 2 shows the percentage of the variation occurred in the time range between 5 p.m. and 6 a.m., column 3 shows the variation occurred in the time between 9 p.m. and 10 a.m., column 4 show the percentage obtained for the not analysed day ($10_{a.m.} - 5_{p.m.}$) and obtained for difference.
These numbers are obtained through the percentage of clear time (Table 7.4) and the correlation percentages (e.g. If we have clear time = 70% $\Longrightarrow$ covered time = 30%. Then we have $A \rightarrow N$ correlation = 95% and $N \rightarrow M$ correlation = 90%. This means that 5% of the meteorological changes occurred between 5 p.m. and 6 a.m., 10% between 9 p.m. and 10 a.m. and the remaining 15% between 10 a.m. and 5 p.m.). We see that most of the changing occur during the day time (from 10 a.m. to 5 p.m.) so it is possible to correlate the afternoon satellite data with the next night satellite data.

Figure 8.4 shows the trend of the $F_{C.A.}(t)$ obtained using all the brightness values and the DIMM seeing. The gray line is the best fit of the monthly plot. In this function we have highlighted the new points used for the night quality forecast (Forecast points). Through the position of these points we can predict whether the night will be stable (Stable time) or clear (Clear time).
Figure 8.5 shows the obtained r_0 values from satellite. These values are obtained through the model described in Section 8 (Equation 8.3). Moreover the value of r_0 is computed taking into account the Paranal height and it is given in the visible range. We obtained values close to those obtained using ground based data. In fact, the FWHM calculated by the $r_{0,Sat}$ value has a high correlation coefficient with the ground FWHM (see Tables 7.6, 7.7 and Figure 8.2).

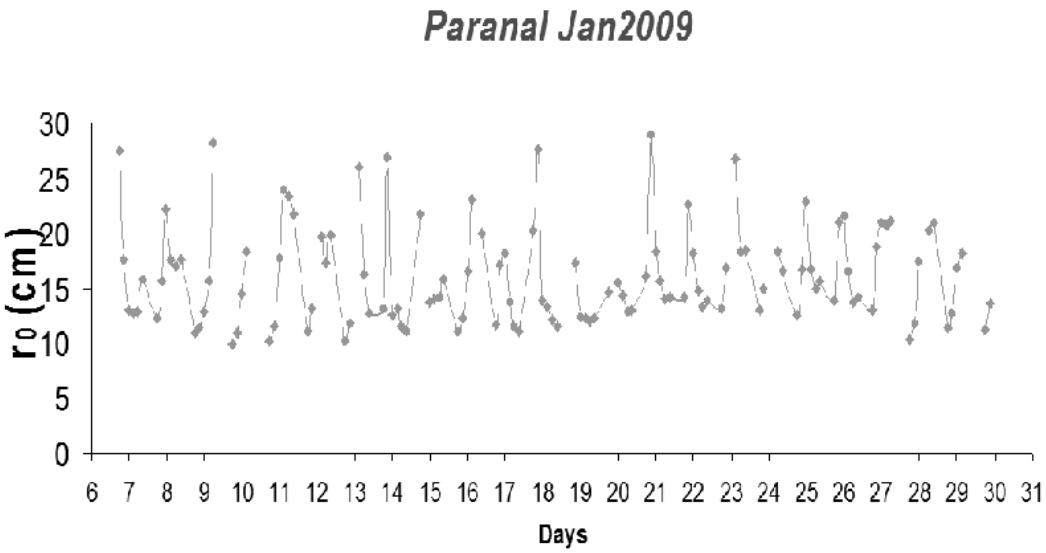

Figure 8.5: Fried's radius values calculated from satellite ($r_{0,Sat}$) at Paranal, January 2009. The satellite FWHM calculated with these values has a correlation coefficient of 0.91 with the ground FWHM (see Figure 8.1).

8.2 Seeing and short-term forecast discussion

In this thesis, as first, we have introduced the concept of satellite seeing using remote sounding from the IR night time data of the GOES 12 satellite. We have discussed the derived correlation between the ground data and the satellite derived values from the analysis of the sites located at Cerro Paranal (Chile) and Roque de Los Muchachos (Canary Islands, Spain) for the 2009. In this analysis we used the $F_{C.A.}(t)$ obtained correlating the monthly mean values obtained in a 1 deg matrix of each of the three selected bands. This functions that is a measure of the gradient of temperature among the three layers sampled by the three bands is, as well as the ground based C_T^2, linked to the r_0. The r_0 values derived using $F_{C.A.}(t)$ (see Section 8) at Paranal and La Palma are close to ground based values, in particular the FWHM calculated by the $r_{0,Sat}$ value has a high correlation coefficient with the ground FWHM (see Tables 7.6, 7.7 and Figure 8.2). In this first analysis we obtained empirically the zero point using the DIMM seeing from each site. We have demonstrate that the plot of the seeing from satellite is in good agreement with the DIMM seeing of the same month (see Figure 8.1) showing a correlation ranging between 80% and 97 % during the months at Paranal. Figure 8.2 shows an example of the dispersion of this correlation and its linear regression for January 2009 at Paranal. We found a better correlation at la

Table 8.2: Meteorological changes at Paranal
for the year 2009.

Months	$5_{p.m.} - 6_{a.m.}$	$9_{p.m.} - 10_{a.m.}$	$10_{a.m.} - 5_{p.m.}$
January	0.0	0.0	100.0
February	100.0	0.0	0.0
March	100.0	0.0	0.0
April	100.0	0.0	0.0
May	0.0	29.3	70.7
June	0.0	33.3	66.7
July	21.5	21.5	57.0
August	35.8	35.8	28.3
September	0.0	0.0	100.0
October	0.0	0.0	100.0
November	0.0	0.0	100.0
December	50.0	50.0	0.0

Palma (89% to 95%), this is due to the fact that the correlation only refers to the clear time, in fact the RoboDIMM does not work during cloudy nights.

Any comments we can gives about the obtained values due the zero point, but we have intention to refine the procedure. As further step we are giving for the first time the forecasting seeing from satellite (see Figure 8.4). We have proceeded in two ways to select the best procedure. In the first test we correlated the brightness temperature of the morning 9:45 with the values of the night before. In the second test we correlated the brightness temperature of the 17:45 afternoon with the night after. The two procedures seems to be show similar results, with a marginal higher percentage in the night-morning values for both the sites, but for the purpose of the prediction of the image quality for the incoming observing night we can use the correlation afternoon-night. We see that at Paranal the correlation decrease during the winter months, instead we found a more homogeneous distribution at la Palma. Through this afternoon-night relationship we can give an estimate of the photometric night quality. In fact, in Section 8 we have demonstrated a high correlation between the $FWHM_{Sat}^{Mean}$ and the $FWHM_{Ground}^{Mean}$ (see Tables 7.6, 7.7 and Figure 8.2). In addition, in Section 8.1 we have shown how the afternoon data are correlated with the night data (see Tables 8.1, column 3). With these two results we have a model that can provide a satellite seeing calculation and a forecast. An interesting result are the values shown in Tables 8.2 and 8.3. The two tables show the monthly percentage of the changes in the observation conditions at the two sites during the 2009. We have obtained that at Paranal the variation of the meteorological conditions

Table 8.3: Meteorological changes at La Palma for the year 2009.

Months	$5_{p.m.} - 6_{a.m.}$	$9_{p.m.} - 10_{a.m.}$	$10_{a.m.} - 5_{p.m.}$
January	15.4	7.7	77.0
February	31.1	15.5	53.4
March	26.9	17.9	55.2
April	55.6	18.5	25.9
May	0.0	11.9	88.1
June	41.7	41.7	16.7
July	19.0	19.0	62.0
August	24.8	0.0	75.2
September	8.3	0.0	91.7
October	10.4	10.4	79.2
November	0.0	0.0	100.0
December	4.7	4.7	90.5

occur during the day time, but the months of February, March and April occur in the time interval between the 5 p.m. and 9 p.m. During the night the weather is almost stable. At La Palma we shown that the variation occur during the day.

Chapter 9

Satellite wind analysis

In this chapter we estimate the amount of available telescope time at four interesting sites for astronomical instrumentation. We use the *GOES 12* data for the years 2008 and 2009. We use a homogeneous methodology presented in several previous chapters to classify the nights as clear (completely cloud-free), mixed (partially cloud-covered), and covered. Additionally, for the clear nights, we evaluate the amount of satellite stable nights which correspond to the amount of ground based photometric nights, and the clear nights corresponding to the spectroscopic nights. We have applied this model to two sites in the Northern Hemisphere (San Pedro Martir (SPM), Mexico; Izaña, Canary Islands) and to two sites in the Southern Hemisphere (El Leoncito, Argentine; San Antonio de Los Cobres (SAC), Argentine). We have obtained, from the two years considered, a mean amount of cloud free nights of 68.6% at Izaña, 76.0% at SPM, 70.6% at Leoncito and 70.0% at SAC. We have evaluated, among the cloud free nights, an amount of stable nights of 62.6% at Izaña, 69.6% at SPM, 64.9% at Leoncito, and 59.7% at SAC. Finally, we describe an empirical model for the satelllite wind calculation (see Section 9.7.

The satellite site testing analysis evolved with the use of multi-channel data, in particular at infrared wavelengths. It allows to detect temperatures at different altitudes, discriminating parameters which produce the cloud coverage. In this study we extracted the night-time data to derive parameters to assess the amount of useful nights, using the Geostationary Operational Environmental Satellite 12 (*GOES 12*) archive. *GOES 12* data are analysed using a code which correlates several bands. We decided to use only GOES data because we have a uniform set of GOES data validated in different situations and at different sites. We know that Meteosat could be in a more favourable position with respect to the geographical location of Izaña, but

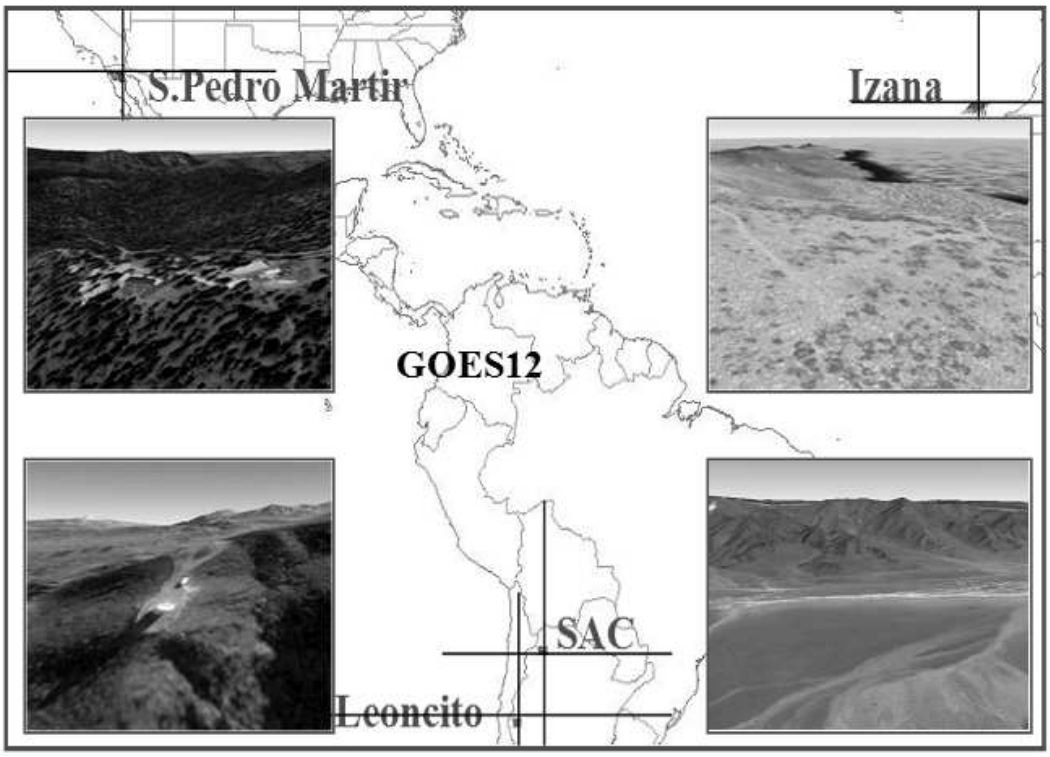

Figure 9.1: Location of the four sites involved in the analysis. As seen in the inserts (modified from Google Earth) the selected sites presents very different topographic conditions. The position of *GOES 12* satellite projected on the map (McIDAS-V Map).

Meteosat data, available on the Web-page[1], are being obtained already as daily averages. The night-time temporal resolution, which is crucial for the purpose of our analysis, is missing. The validation of our code was done using data of two important sites for the optical astronomy: El Roque de Los Muchahcos (ORM, Canary Islands), and Cerro Paranal (Chile), two very different sites with different climatic conditions. The results of the validation are published in Cavazzani at al. ([2011]), Della Valle et al. ([2010]).
We point out that our analysis is connected with the traditional definitions of the astronomical nights (clear, mixed and unusable). We are aware that there are interesting packages of data such as ECMWF[2] (Dee et al. ([2011])), FriOWL[3] (Sarazin et al. ([2006]), Graham et al. ([2005]), ([2008])) and Giovanni [4] (Acker and Leptouk ([2007])), used for wide scale and long term climatic trends. We intend to use them in a next chapter dedicated to long term cloud coverage. For the present thesis these data do not have the required temporal and space resolution we need. In addition they have to be calibrated in terms of astronomical properties. Specific studies should be done on the sites. In this chapter we present the evaluation of the amount of usable nights for four interesting sites for astronomical instrumentation. The sites are located in Argentina, Spain (Canary Islands) and Mexico. For each site we additionally report the mean temperature and rainfall obtained from literature to have a more complete information of each analysed site. Table 9.1 shows the geographic positions of the sites, while Figure 9.1 shows the location of the interested sites. The tiles of Figure 9.1 show how different is the morphology of each site. All the candidates sites are located in the subtropical belt, and the Canary Islands site is the only one centred in a wide homogeneous oceanic air mass.

9.1 Satellite based data and acquisition

A detailed discussion about the advantages of this satellite is presented in the previous chapters. Each infrared band detects clouds at different heights. This is due to the Planck shape of its weighting function (WF), specific for each band, that presents a maximum of efficiency at different altitude according to the different selected band. The water vapour band (channel 3, band 3 hereafter B3, centered at 6.7 μm and sensitive between $6.5 - 7.0$ μm)

[1] http://www.eumetsat.int
[2] www.ecmwf.int
[3] http://archive.eso.org/friowl-45/
[4] http://disc.sci.gsfc.nasa.gov/giovanni/overview/index.html

Table 9.1: Geographic characteristics of the analyzed sites and *GOES 12* satellite. The view angle is obtained through the formula $\theta = \sqrt{(\Delta LAT)^2 + (\Delta LONG)^2}$.

site	LAT.	LONG.	Altitude Km	View Angle
Leoncito	$-31°47'$	$-69°17'$	2.552	$32°00'$
S.Pedro Martir	$31°02'$	$-115°29'$	2.800	$51°00'$
Izañ a	$+28°18'$	$-16°29'$	2.373	$61°00'$
SAC	$-24°\ 02'$	$-66°\ 14'$	3.600	$26°00'$
GOES 12	$+0°00'$	$-75°00'$	35800	

Table 9.2: *GOES 12* bands and resolution at Nadir with their weighting functions (WF).

	window	pass-band $[\mu m]$	1px resolution $[km]$	WF $[m]$
BAND3	H_2O	$6.50 - 7.00$	4	8000
BAND4	IR	$10.20 - 11.20$	4	4000
BAND6	CO_2	13.30	8	3000

is able to detect high altitude cirrus clouds, up to 8 km. The cloud coverage channel (channel 4, band 4 hereafter B4, centered at 10.7 μm and sensitive between $10.2 - 11.2$ μm) can detect middle level clouds, at about 4 km, and the CO_2 band (channel 6, band 6 hereafter B6, centered at 13.3 μm) senses small particles such as fog, ash and low level clouds, at about 3 km[5]. The output of the detector is proportional to the energy reaching the sensor per unit time (radiance) that is equivalent to the brightness temperature. If clouds are not present during the night, the emission at B4 (10.7 μm) reaching the satellite is not absorbed by the atmosphere so the measured radiance values are due to the emission from surface.

Figure 9.1 shows the area of the field of view covering the sites interested in this analysis. We have selected a region of the image for downloading, centered on each site. For each hour and for each band we have processed data as following:

- Extraction of $1° \times 1°$ sub-matrix centered on the coordinates of each site, at 20:45, 23:45, 02:45, 05:45, 8:45 local time for each night.

[5]http://goes.gsfc.nasa.gov/

- Computing of the mean matrix value at 20:45, 23:45, 02:45, 05:45, 8:45 of each night and for each site.
- The total number of images used in this analysis is $N_{Tot} = 43200$

9.2 Satellite night classification

We have seen in previous chapters that the satellite night classification is based on the B4 band flux variability in each month. We assume that the maximum brightness temperature T_B^{Max} in the B4 band occurs if the night is clear. This occurs because, when we have an optically thick cloud in the path, the brightness temperature detected by the satellite drops according to the top temperature of the cloud. The model is accurately described in Cavazzani et al. ([2010]) and Cavazzani et al. ([2011]). We search the maximum brightness temperature T_B^{Max} for each month as the reference temperature. Moreover we compute for each month a threshold as the statistical mode, night by night, of just the differences of the brightness temperature at 23:45 and 8:45 (we have estimated that at these times we have the maximum and minimum values of the brightness temperature). We define 1σ value through the formula:

$$Mode\ Night\ Satellite\ Temperature = 1\sigma = T_B^{23:45} - T_B^{8:45}$$

The nights are then classified according to the value of T_B (see Table 4.3) where $T_B \Rightarrow$ is the computed mean brightness temperature of the $1° \times 1°$ matrix at 20:45, 23:45, 02:45, 05:45, 8:45 for each night and in the B4 band. All the above described procedures were validated using the Paranal and La Palma observing logbooks. Table 4 of Cavazzani et al. ([2011]) shows the results of the validation.
To have a more reliable comparison between satellite and ground based classification we introduce the concept of a stable night. This concept takes into account all the selected bands defining an atmospheric correlation function $F_{C.A.}(t)$ in the following way

$$F_{C.A.} = I_{\lambda_3} - [I_{\lambda_6} - I_{\lambda_4}] \tag{9.1}$$

Where I_{λ_3}, I_{λ_4} and I_{λ_6} are the monochromatic emission fluxes from the Earth surface in each band as received by the sensor. $F_{C.A.}(t)$ is a value computed for each detected hour and for each night. We would say that this model takes into account auto-corrections of atmosphere: for instance if two high layers have a positive oscillation and one lower layers has an equal magnitude oscillation, but negative, the $F_{C.A.}(t)$ remains constant. From the

physical point of view this means that there are no relative changes in the atmospheric properties at the two layers, so they are affected by uniform air masses.
Considering the best fit of the monthly plot of $F_{C.A.}(t)$ we obtain the classification described in Table 4.3. With these definitions we obtain the fraction of clear and stable nights of the analysed sites as shown and discussed in the following sections.

9.3 Sites analysis

In this section we present the classification of the nights at each site using the code described above. In order to have a more general information. The results are compared with literature data.

9.4 Izañ a (Canary Island) site

The climate of all the Canary Islands, located in north of the Tropic of Cancer, is modulated by the Azores Anticyclone. Izañ a Observatory (IZO) has an Atmospheric Research Center (IARC) in the mountains of the island of Tenerife. The climatic characteristics of IZO are driven by the altitude. IZO is located at 2400 meters above sea level, higher than the quasi-permanent temperature inversion layer associated to the trade-winds regime. The inversion layer separates the moist marine boundary layer from the dry, free troposphere. Table 9.3 shows the monthly distribution of temperature and rain obtained using the Agencia Estatal de Meteorología (AEMET) database to show the seasonal trend. The average of temperatures obtained on this time baseline is 9.2°C. In 2008 the mean annual temperature was 9.8°C, while in 2009 it was 10.2°C. These two values are well above the mean values in Table 9.3. Moreover we see that the precipitations occur mainly in winter time when Atlantic low pressure systems pass over the Canary Islands.

The first evaluation of the available observing time at Tenerife, is by Murdin ([1985]) with 61% of photometric hours and 14% of spectroscopic hours, computed from February to September 1975.

The results obtained by our code using the *GOES 12* satellite data are shown in Table 9.4, where we present the percentage of covered, clear and stable nights for 2008 and 2009. The number of clear nights shows a large variability over the two years, including the summer time, which is a typically dry period. Taking into account the same period from Murdin, February-September, we obtain from satellite 79% of clear nights for 2008 and 69%

Table 9.3: Mean monthly temperature (1920-2010),rain(1971-2000) and wind velocity at Izaña (www.Izaña.org).

month	Mean temp. (deg C)	Precipitation (mm)
January	3.8	86.6
February	3.9	64.3
March	5.3	65.0
April	6.8	25.6
May	9.3	13.7
June	13.2	0.5
July	17.4	0.4
August	17.4	2.4
September	13.6	14.8
October	9.7	36.0
November	6.6	50.0
December	4.2	73.4

for 2009, considerably higher values with respect to those of Murdin. Can we ascribe these differences to a yearly variability or to different evaluation criteria?

9.5 S.Pedro Martir (Baja California) site

The second site analysed is the observatory at San Pedro Martir in Baja California, Mexico.

Tapia et al. [2007] give the results of more than three decades of site characterizations. This long statistical analysis of cloud coverage shows that the fraction of nights lost due to bad weather is about 21.4% in the period July 1982 to December 2006. From January 1984 to December 2006, 64.1% of the nights were of photometric quality and 80.3% were of spectroscopic quality. The average relative humidity near the ground was 54% (Tapia ([1992])) with a large seasonal dependence. Spring and autumn are the best seasons in terms of cloudless and low humidity nights, while winter is affected by the tails of North Pacific storms and mid summer is characterized by a mild monsoon season. The data are based on the $2.1m$ telescope observing log. For the same site, Erasmus and van Rooyen ([**?**]) found an amount of useful time of 81.6%, obtained using the IR GOES satellite bands computed for the period June 1997 to May 1998, showing, for the same period, a good

Table 9.4: *GOES 12* night time classification at Izaña .

	Izaña 2008				Izaña 2009			
Month	Covered	Mixed	Clear	Stable	Covered	Mixed	Clear	Stable
January	39.9	6.3	53.8	48.3	34.2	14.2	51.6	50.8
February	21.8	5.6	72.6	62.1	30.6	14.5	54.9	49.2
March	33.8	9.0	57.2	47.6	27.8	11.1	61.1	54.9
April	9.3	2.9	87.9	79.3	10.7	12.9	76.4	66.4
May	5.6	7.0	87.4	74.1	9.1	18.2	72.7	68.5
June	0.0	4.9	95.1	93.1	16.7	7.6	75.7	66.7
July	3.4	4.1	92.5	78.6	11.0	9.0	80.0	76.6
August	10.9	7.0	82.1	81.4	8.6	8.6	82.8	72.9
September	30.9	9.2	59.9	59.2	34.9	16.6	48.5	45.0
October	9.2	6.9	83.9	78.2	20.1	10.9	69.0	67.2
November	27.3	10.5	62.2	53.8	20.3	16.1	63.6	59.4
December	42.6	11.5	45.9	41.0	51.1	19.9	29.0	27.7
Mean	19.6	7.1	73.4	66.4	22.9	13.3	63.8	58.8

agreement with the Tapia data (about ±5%). Using the weather station installed at this site, we collected temperature, wind speed and rainfall data for the years 2007 to 2010 using the SPM weather Web-page[6]. Table 9.5 summarizes the monthly distribution of these parameters.

Table 9.6 shows the classification of the nights obtained using the *GOES 12* satellite. For this site we also see a large variability for the two years. The percentages of the nights are not very different from those obtained using the ground based data. The satellite gives an additional 10% of clear nights.

9.6 S. Antonio de los Cobres (Argentina) site

S. Antonio de los Cobres is located at 3600 m above sea level, and is located in the province of Salta, 164 km away from Salta. Some limited meteorological data are available for the period 2001-2010, and the monthly values can be found in the official report of the two sites in Argentina compiled by the Argentinian and Brazilian parties (version 1.1, July 6 2011). On the basis of the temperatures acquired at the meteorological station of the *Gendarmeria National*, which gives the monthly averages over ten years (2001-2010), we found that the maximum temperature occurs in November (14.4 ^{0}C) while the minimum temperature occurs in August (-7 ^{0}C). From the *GOES 12* satellite we obtain the percentages of available time presented in Table 9.7. These results are almost in agreement with a similar analysis of Erasmus

[6]http://www.astrossp.unam.mx/weather15/

Table 9.5: Mean monthly temperature,rain and wind velocity at SPM of the years 2007 to 2010. (http://www.astrossp.unam.mx/weather15/)

month	Mean temp. (deg C)	Precipitation (mm)	wind speed (m/s)
January	1.2	18.5	4.1
February	1.3	1.2	3.6
March	4.1	3.6	3.3
April	5.5	2.9	3.7
May	8.8	1.5	3.4
June	13.9	3.2	3.7
July	15.7	62.2	2.3
August	15.2	80.9	2.9
September	12.3	9.9	3.5
October	8.7	14.2	4.7
November	5.9	11.8	4.2
December	3.8	3.4	3.8

Table 9.6: *GOES 12* night time classification at SPM.

	S.Pedro Martir 2008				S.Pedro Martir 2009			
Month	Covered	Mixed	Clear	Stable	Covered	Mixed	Clear	Stable
January	32.2	2.8	65.0	58.7	18.3	10.0	71.7	69.2
February	13.7	8.1	78.2	75.8	32.3	9.7	58.0	54.8
March	4.1	2.1	93.8	84.1	16.7	7.6	75.7	63.2
April	3.6	0.7	95.7	84.3	7.1	7.1	85.8	80.7
May	8.4	4.2	87.4	83.2	7.0	4.2	88.8	71.3
June	0.0	1.4	98.6	97.2	22.9	14.6	62.5	56.3
July	14.5	6.9	78.6	75.2	22.1	7.6	70.3	60.0
August	16.3	17.1	66.6	58.9	8.6	2.1	89.3	82.9
September	9.2	5.9	84.9	80.3	13.0	7.1	79.9	74.0
October	0.0	3.4	96.6	89.7	11.5	9.2	79.3	70.1
November	30.1	11.2	58.7	54.5	15.4	4.2	80.4	72.7
December	42.6	11.5	45.9	42.6	46.6	22.7	30.7	29.8
Mean	14.6	6.3	79.2	73.7	18.5	8.8	72.7	65.4

Table 9.7: *GOES 12* night time classification at SAC.

	S.Antonio de Los Cobres 2008				S.Antonio de Los Cobres 2009			
Month	Covered	Mixed	Clear	Stable	Covered	Mixed	Clear	Stable
January	67.8	13.3	18.9	16.8	25.8	24.2	50.0	47.5
February	15.3	16.9	67.8	56.5	28.2	14.5	57.3	54.8
March	10.3	15.2	74.5	66.2	27.8	20.8	51.4	50.7
April	6.4	9.3	84.3	72.9	7.1	9.3	83.6	72.1
May	7.0	4.2	88.8	76.9	4.2	2.1	93.7	72.0
June	13.9	9.7	76.4	67.4	13.9	6.9	79.2	63.9
July	0.0	2.1	97.9	74.1	26.9	19.3	53.8	49.7
August	3.1	3.1	93.8	76.0	7.9	8.6	83.5	65.7
September	6.6	13.8	79.6	64.5	8.3	10.1	81.6	65.1
October	39.7	5.7	54.6	49.4	20.7	10.9	68.4	60.3
November	4.2	14.0	81.8	72.0	12.6	21.7	65.7	49.7
December	29.5	21.3	49.2	47.5	42.6	12.1	45.3	41.1
Mean	17.4	10.7	72.3	61.7	18.8	13.4	67.8	57.7

and Maartens ([2001]) using the *GOES 8* satellite. They derive percentages of 75% of clear time and 5% of partially cloudy time at the coordinates of Macon (Lat -24 37' Long -67 19'), for the period 1993-1999.

9.7 Satellite wind analysis

Analyzing the SAC site we noticed strong fluctuations of the B3. In particular, we noticed that sometimes the B3 value exceeded the B4 value (see Figure 9.3). These episodes occur only in rare cases at Paranal, although to a lesser extent. From the Paranal Web-site we noticed that a strong ground wind corresponds to these events. For this reason we started a preliminary study from the satellite wind analysis, using the B3 and B4 bands, for this site which we discuss in this Section. We plan to improve this model in the future using more data to detect the presence of different wind phenomena affecting the results. In this thesis we present two different and preliminary classifications: a statistical classification based only on the trend of B3 and B4 and a physical classification based on site characteristics (altitude, temperature and satellite angle of view). The physical classification gives us the opportunity to obtain an estimate of the wind speed. The wind model is empirically calibrated using the data of Paranal obtained from the Web-site. Figure 9.2 shows that the two sites lie at a distance of about $430km$.

We stress that at the moment this is an empirical model. This means that the results may be subject to various interpretations: we observe large-scale fluctuations and assume that they can cause the wind phenomena due to

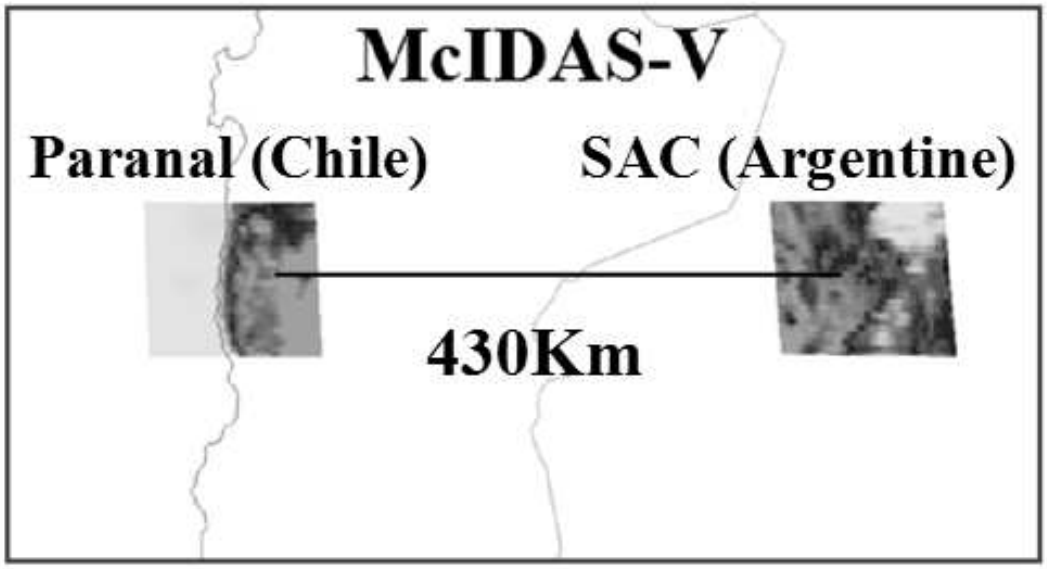

Figure 9.2: Paranal and SAC matrix (McIDAS-V Map). The geographical proximity allows the same calibration of the empirical model.

the calibration done at Paranal. The fluctuation could also occur with other local phenomena due to the particular topography of the site. Certainly the fluctuation corresponds to fast temperature changes at high altitude and these variations cause winds at the ground for sites of Paranal and La Palma.

9.7.1 Statistical wind classification

Using the classification of the ESO Web-page[7] for Paranal we can do an initial classification of the wind speed:

- Weak wind $\Rightarrow v < 10m/s$

$$I_{\lambda_4} - I_{\lambda_3} > 1\sigma$$

- Strong wind $\Rightarrow 10m/s < v < 15m/s$

$$0 < I_{\lambda_4} - I_{\lambda_3} < 1\sigma$$

- Extremely strong wind $\Rightarrow v > 15m/s$

$$I_{\lambda_4} - I_{\lambda_3} < 0$$

[7] http://archive.eso.org/asm/ambient-server

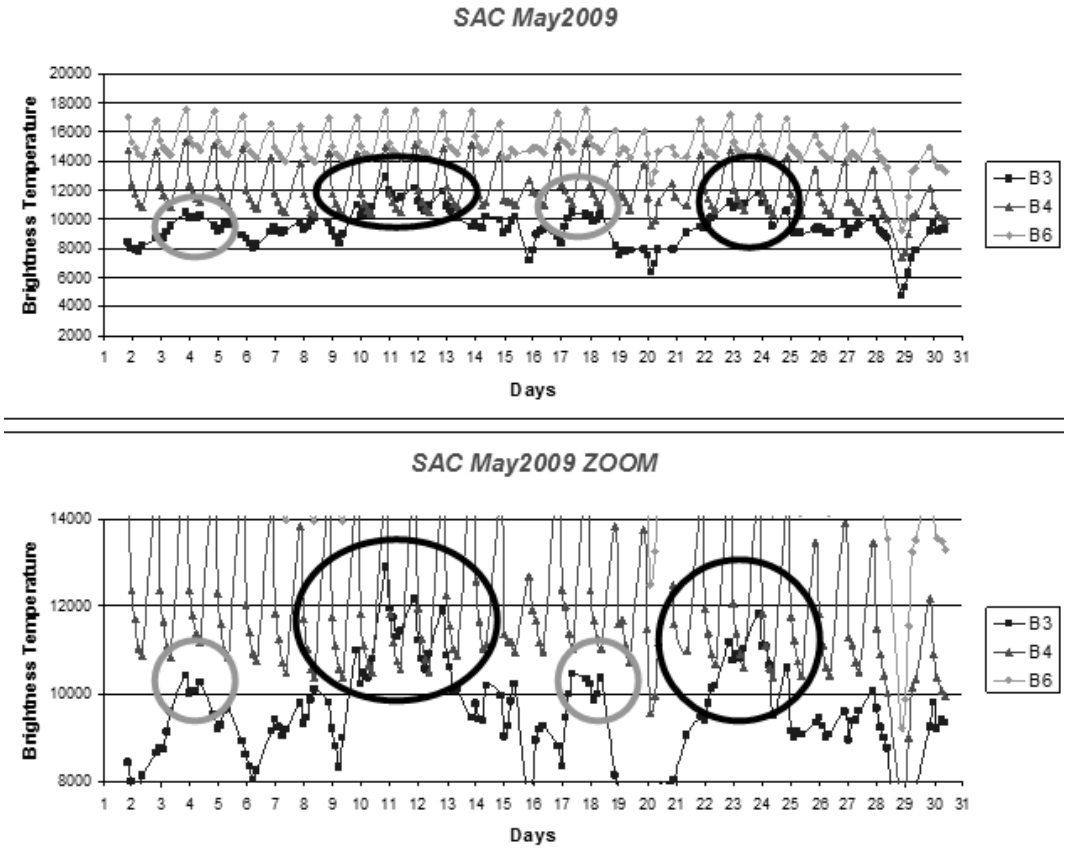

Figure 9.3: Analysis of the brightness temperature May 2009 at SAC. The gray ovals show perturbed points to be interpreted as windy episodes. Black ovals contains points possibly corresponding to the extremely strong wind.

Tables 9.8 and 9.9 show the results of this classification applied at SAC in 2008 and in 2009 respectively. Figure 9.4 shows the two years histogram of this satellite analysis. July 2008 has been a very windy month followed by May 2008 as shown in Figure 9.5 that plots the wind speed for the complete month of May 2008 at SAC.

9.7.2 Physical wind classification

We can also to evaluate empirically the wind speed that we present in this Section. Also in this case the model is calibrated using the down-loaded data from the Web-page of Paranal. The wind speed is calculated as a function of the site altitude ($h(m)$) and the satellite angle of view (θ). The model uses the exponential trend of the Kolmogorov theory of turbulence combined

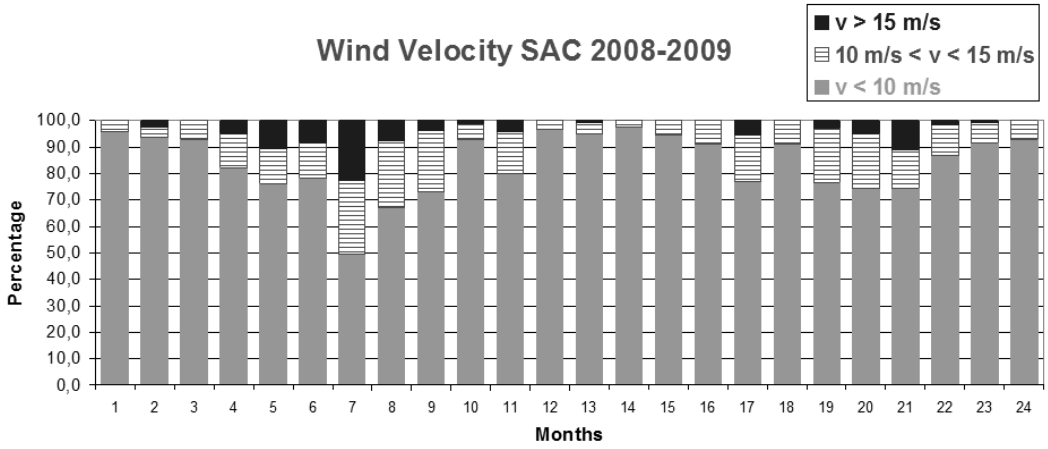

Figure 9.4: Estimated distribution of the wind speed at SAC (2008-2009) from satellite analysis. The gray bars show the monthly percentage of time with little or no wind ($v < 10m/s$), the dashed gray bars indicate the monthly percentage of time with strong winds ($10m/s < v < 15m/s$) and the black bars indicate the monthly percentage of time with extremely strong wind ($v > 15m/s$).

Table 9.8: *GOES 12* velocity of wind classification at S. Antonio de Los Cobres (SAC) 2008.

Month	Weak Wind	Strong Wind	E-Strong Wind
January	95.8	4.2	0.0
February	93.6	4.0	2.4
March	93.1	6.9	0.0
April	82.1	12.9	5.0
May	76.2	13.3	10.5
June	78.5	13.2	8.3
July	49.4	27.8	22.8
August	67.4	24.8	7.8
September	73.1	23.0	3.9
October	93.2	5.7	1.1
November	79.7	16.1	4.2
December	96.7	3.3	0.0
Mean	81.6	12.9	5.5

Table 9.9: *GOES 12* velocity of wind classification at S. Antonio de Los Cobres (SAC) 2009.

Month	Weak Wind	Strong Wind	E-Strong Wind
January	95.0	4.2	0.8
February	97.6	2.4	0.0
March	94.4	5.6	0.0
April	91.4	8.6	0.0
May	76.9	17.5	5.6
June	91.0	9.0	0.0
July	76.5	20.7	2.8
August	74.3	20.7	5.0
September	74.5	14.8	10.7
October	86.8	11.5	1.7
November	91.6	7.7	0.7
December	92.9	7.1	0.0
Mean	86.9	10.8	2.3

with the kinetic theory of gases, and the wind velocity (expressed in $\left[\frac{m}{s}\right]$) is obtained through the formula:

$$v = \sqrt{e^{\left[\frac{A}{B/cos\theta}\right]}} \tag{9.2}$$

where:

$$A = \frac{I_{\lambda_4} - I_{\lambda_3}}{cos\theta} + \left\{\frac{\overline{|I_{\lambda_4} - I_{\lambda_3}|}}{h(m)}\right\} \cdot \frac{\overline{I_{\lambda_3}}}{cos\theta} + \frac{2h(m)}{cos\theta}$$

and

$$B = \overline{|I_{\lambda_4} - I_{\lambda_3}|}$$

We emphasize that the model was empirically calibrated. We note, however, that the equation 9.2 is based only on the altitude of the site and on the satellite data. This allows us to estimate the wind speed without the need of ground data.

9.8 El Leoncito (Argentina) site

This site is located in the San Juan Province. It is near Casleo Observatory, and close to the El Leoncito National Park. The Observatory has its own

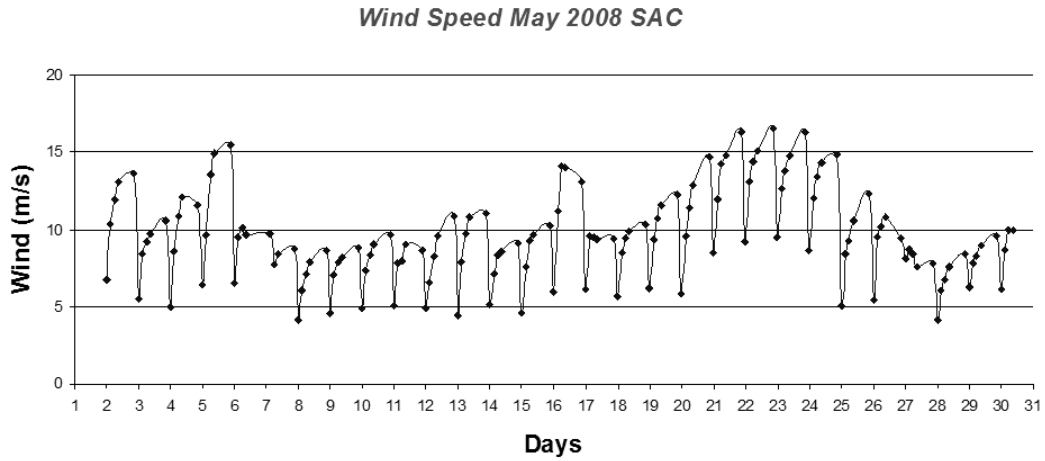

Figure 9.5: Figure shows the monthly trend of the wind speed $\left[\frac{m}{s}\right]$ obtained with the physical wind classification (May 2008 at SAC).

meteorological station. The Web-page[8] shows the current data. Rovero et al. ([2008]) give the monthly mean values of the last 10 years derived from the local meteorological station. Some of the most important meteorological data are given in Table 9.10. Table 9.11 shows the percentages of available time from *GOES 12* obtained for this site. We obtained an amount of about 71% of clear time, in good agreement with the percentage of 74% of observing nights obtained by Rovero et al. ([2008]) from the analysis of more than 20 years of observing nights.

[8] www.casleo.gov.ar/weather/leonci_weather.htm

Table 9.10: Mean monthly meteorological parameters

Parameters	Values
Mean temperature	5.5 ^{0}C.(July) and 17.5 ^{0}C. (January)
Maximum temperature	20.3^{0}C.(June) and 30.5 ^{0}C. (January)
Rel.hum.	27-43 % along the year
Rainfall	11-18 mm (December-March) and 2-7 mm (April-November)
Wind speed	4.5-8.4 km/hr, mainly from SW (55 %) and from SE (30 %)
Maximum wind speed	62-88 km/hr along the year
Hail	1-2 days/yr
Frost	none
Lightning	6-8 days/yr
Maximum snowfall	30 cm

Table 9.11: *GOES 12* nights classification at Leoncito.

	Leoncito 2008				Leoncito 2009			
Month	Covered	Mixed	Clear	Stable	Covered	Mixed	Clear	Stable
January	9.1	19.6	71.3	66.4	15.8	20.8	63.4	60.
February	27.4	9.7	62.9	62.1	13.7	6.5	79.8	67.7
March	17.9	2.8	79.3	73.8	13.2	12.5	74.3	72.9
April	17.1	8.6	74.3	72.1	1.4	4.3	94.3	83.6
May	15.4	7.0	77.6	69.2	38.5	23.8	37.7	34.3
June	15.3	6.9	77.8	72.2	27.8	7.6	64.6	56.3
July	37.0	5.9	57.1	55.6	13.8	13.1	73.1	62.8
August	21.7	12.4	65.9	58.9	27.1	11.4	61.5	58.6
September	35.5	7.9	56.6	54.6	20.1	14.8	65.1	58.6
October	9.2	6.3	84.5	77.6	33.9	9.2	56.9	50.0
November	5.6	7.0	87.4	86.7	16.8	6.3	76.9	65.0
December	9.8	9.8	80.4	78.7	21.3	7.1	71.6	59.6
Mean	18.4	8.7	72.9	69.0	20.3	11.5	68.3	60.8

Chapter 10

Discussion of the satellite characterization

In our analysis we found that, with regard to the cloud cover and atmospheric stability (Mean 2008-2009: 76.0% Clear, 69.6% Stable), the best site is SPM. Then we have two sites to be considered on the same level: Izaña and Leoncito (respectively, Mean 2008-2009: 68.6% Clear, 62.6% Stable. Mean 2008-2009: 70.6% Clear, 64.9% Stable). El Leoncito has a uniform distribution of the observation time, less influenced by the seasons compared to the Izaña. Izaña, on the contrary has very stable summer months and lower quality winter months (especially in December and January). We also noticed that the statistics of only two years may be influenced by a particular month: for example December 2009, SPM Clear 30.7%; December 2009, Izaña Clear 29.0%; May 2009, Leoncito Clear 37.7%; January 2008, SAC Clear 18.9%. Figures 10.1 and 10.3 show the seasonal trends of the clear and stable nights for the sites in the northern hemisphere and southern hemisphere respectively. In addition Figures 10.2 and 10.4 show the seasonal trends of the clear, mixed and covered nights for the same sites. The anomalous months and the characteristics described above in these figures are evident. We have to make comments regarding the site of SAC (Mean 2008-2009: 70.0% Clear, 59.7% Stable). SAC has generally a low cover, but it has bad months that are not always related to the seasons. Furthermore, analysis of data showed strong fluctuations of the B3. These fluctuations indicate the presence of large atmospheric airmass instabilities and may indicate strong winds as shown in Cavazzani et al. ([2010]). In Sections 9.7 we have described an empirical procedure for the calculation of these winds (Mean 2008, strong wind $\Rightarrow 10m/s < v < 15m/s$, 12.9%; extremely strong wind $\Rightarrow v > 15m/s$, 5.5%. Mean 2009, strong wind , 10.8%; extremely strong wind, 2.3%). This is consistent with the fact that SAC is the highest

Table 10.1: Satellite available nights for the candidate sites.

	Izaña				SPM			
	Clear		Stable		Clear		Stable	
	2008	2009	2008	2009	2008	2009	2008	2009
Mean	73.4	63.8	66.4	58.8	79.2	72.7	73.7	65.4
	Leoncito				SAC			
	Clear		Stable		Clear		Stable	
	2008	2009	2008	2009	2008	2009	2008	2009
Mean	72.9	68.3	69.0	60.8	72.3	67.7	61.7	57.7

site (3600m).
Using *GOES 12* satellite we have presented a homogeneous method in order to obtain the amount of available time fraction for four interesting sites for astronomical instrumentation. In order to have a complete analysis we have also collected meteorological characteristics from literature. In this analysis a wider spatial field is used in order to reduce the spatial noise: each value is the mean of $1^\circ \times 1^\circ$ matrix. The cloud coverage is obtained using the *GOES 12* B4 band. Using the correlation of the three bands, B3, B4 and B6, we have computed an atmospheric correlation function as a further selection of the clear nights, and we have introduced the new concept of stable night. The years 2008 and 2009 are analysed.

We found for the 2008 the following clear nights: 73.4% Izaña, 79.2% at San Pedro Martir, 72.9% Leoncito and 72.3 % SAC. For the 2009 we found: 63.8% Izaña, 72.7% at San Pedro Martir, 68.3% Leoncito and 67.8 % SAC. Instead, the number of stable nights for the 2008 is: 66.4% Izaña, 73.7% at San Pedro Martir, 69.0% Leoncito and 61.7 % SAC. For the 2009 we found 58.8% Izaña, 65.4% at San Pedro Martir, 60.8% Leoncito and 57.7 % SAC.

The mean of the two years gives a percentage of clear nights of 68.6% Izaña, 76.0% at San Pedro Martir, 70.6% Leoncito and 70.0 % SAC, while the mean of the two years gives a percentage of stable nights of 62.6% Izaña, 69.6% at San Pedro Martir, 64.9% Leoncito and 59.7 % SAC.
Izaña shows a large variability of clear night in these two years, while the percentage of stable nights is about 6.0% less that the clear nights. SAC shows a large fluctuation in the considered years and the estimate of the percentage of clear nights does not take into account the wind speed (see Section 9.7).

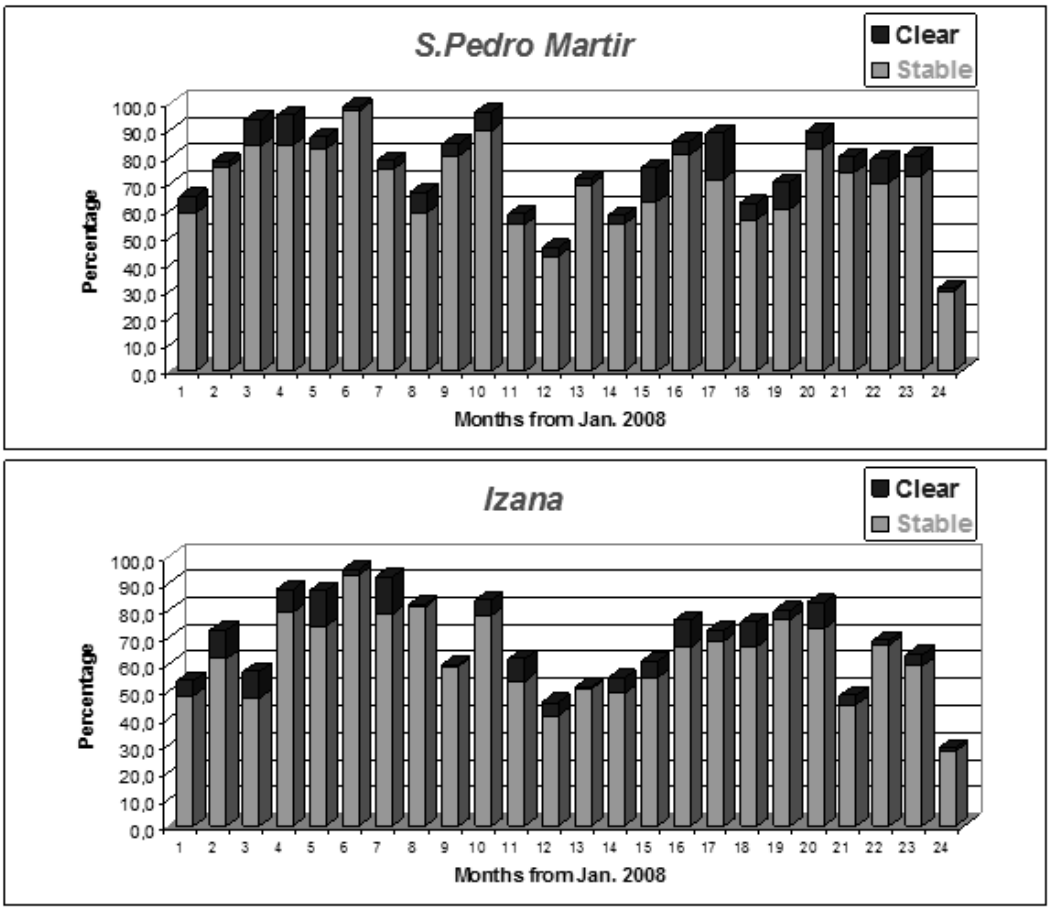

Figure 10.1: Distributions of stable and clear nights at S. Pedro Martir and Izaña (2008-2009) obtained from *GOES 12* satellite.

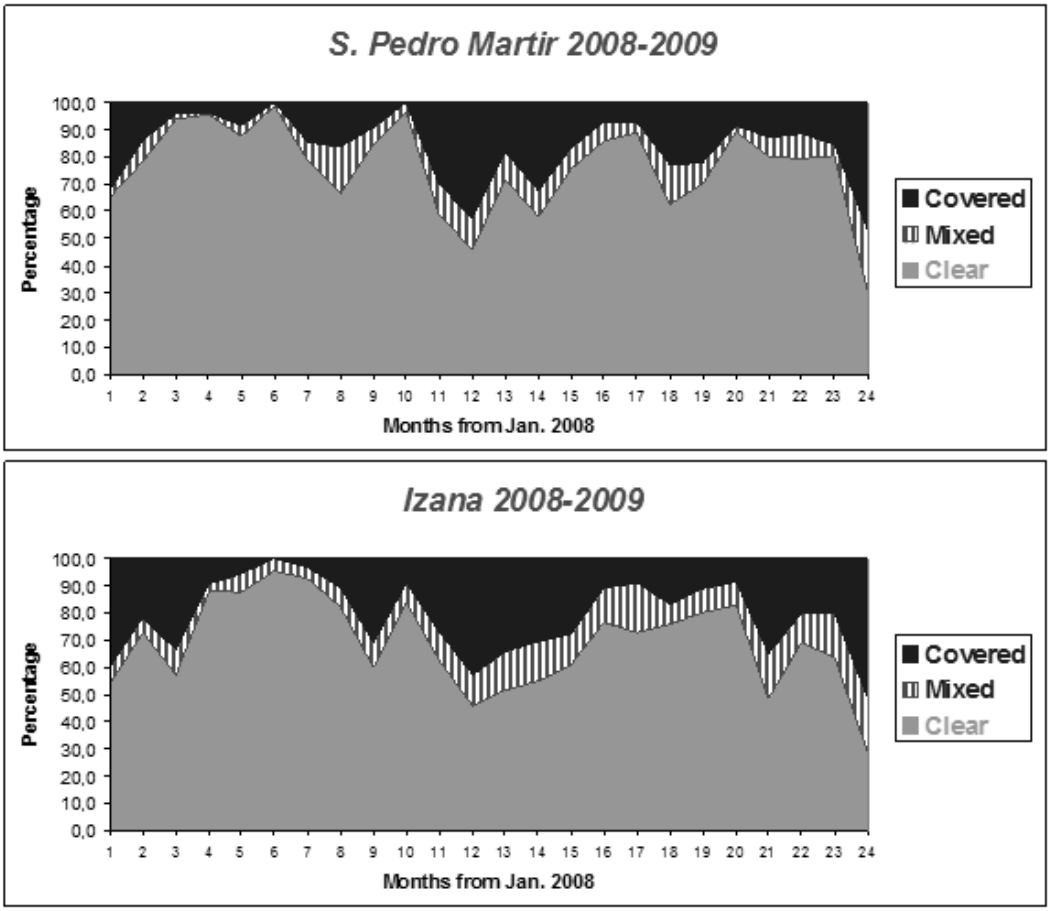

Figure 10.2: Distributions of clear, mixed and covered nights at S. Pedro Martir and Izañ a (2008-2009) obtained from *GOES 12* satellite.

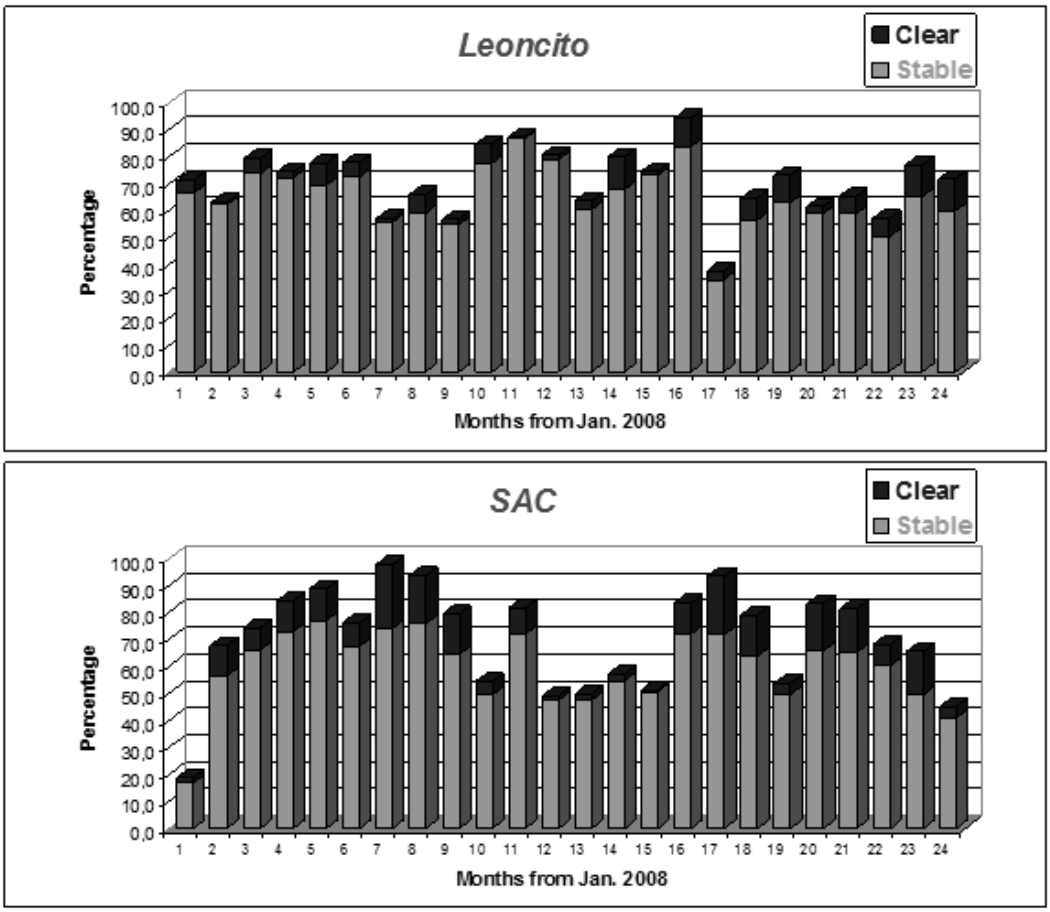

Figure 10.3: Distributions of stable and clear nights at Leoncito and SAC (2008-2009) obtained from *GOES 12* satellite.

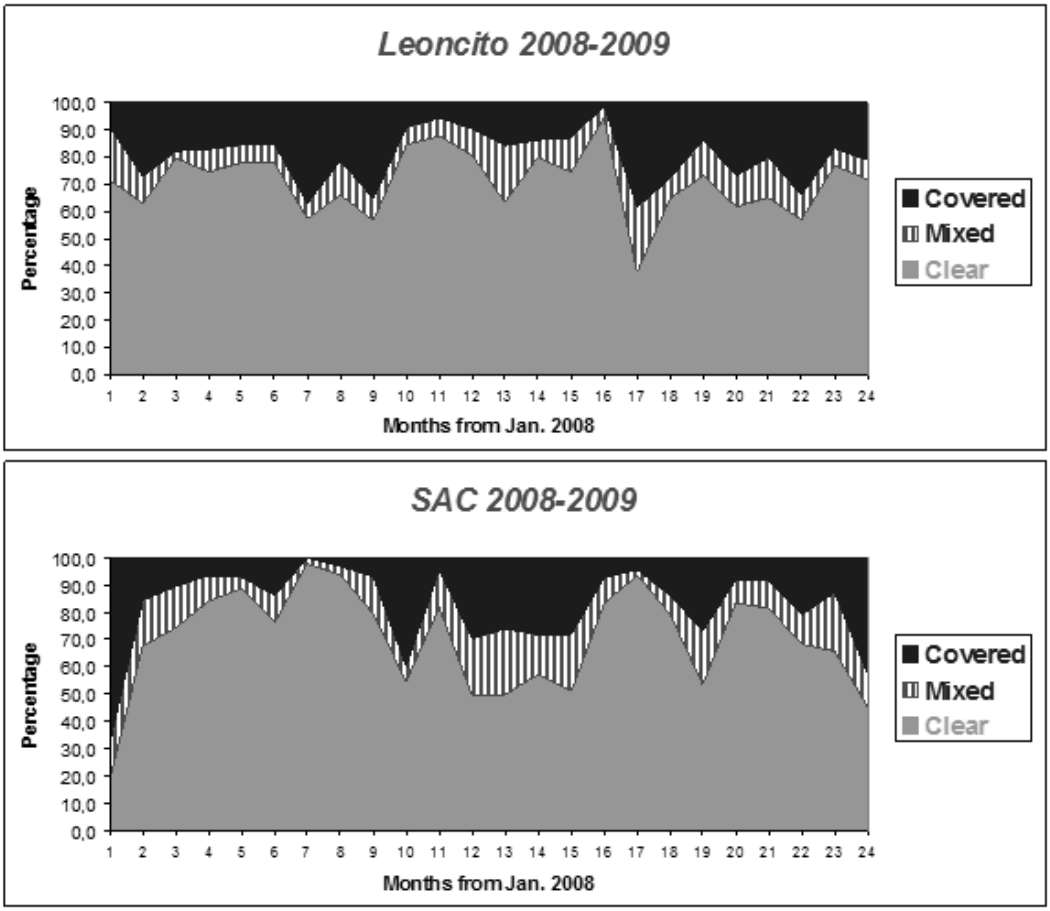

Figure 10.4: Distributions of clear, mixed and covered nights at Leoncito and SAC (2008-2009) obtained from *GOES 12* satellite.

Chapter 11

Long-term analysis of astronomical sites: a comparison between polar and geostationary satellite

In recent years, with the development of new telescopes projects, becomes of great importance the study of cloud cover: in particular for the selection of new sites as well as for the development of existing telescopes. At the moment there is a discussion on how to study the climatic conditions. Mainly we have two large data sets: satellite data and ground data, the two groups have advantages and disadvantages. In this thesis we make an analysis of three sites of great astronomical importance: Mt Graham, Paranal and La Silla. We analyze in detail of the various data available, we compare these data and we seek a correlation between them. In particular, we focus on the long-term study to have a statistical trend of climate change. In detail, we use two satellites: GOES (Geostationary Operational Environmental Satellite) and MODIS (Moderate Resolution Imaging Spectroradiometer). Finally we use two ground data archives: FriOWL and Wolfram Alpha. FriOWL is a Java based Geographical Information System (GIS) using a global climatic and geomorphological database while Wolfram Alpha is a computational knowledge engine. The use of such data allows us a mutual validation of results, moreover this analysis can be applied to each site of the planet.

In this chapter we analyze three astronomical sites: Mt. Graham, Paranal e La Silla see Table 11.1 and Figure 11.1. This analysis is divided into three main steps:

1. We analyze the year 2009 at Mt. Graham and Paranal with GOES

Table 11.1: Geographic characteristics of the analyzed sites and GOES12 satellite. The view angle is obtained through the formula $\theta = \sqrt{(\Delta LAT)^2 + (\Delta LONG)^2}$.

site	LAT.	LONG.	Altitude Km	View Angle
Mt.Graham	$+32°42'$	$-109°52'$	3.267	$47°40'$
Paranal	$-24°37'$	$-70°24'$	2.630	$25°00'$
La Silla	$-29°15'$	$-70°43'$	2.347	$29°30'$
GOES12	$+0°00'$	$-75°00'$	35800	

and MODIS data. We compare these data and we give a monthly correlation coefficient.

2. We do a long-term satellite analysis and we extrapolate a statistical climate trend for Mt. Graham, Paranal and La Silla.

3. We compare the obtained satellite results with the ground data processed by FriOWL.

The comparison with the various groups of data allows us to overcome the limitations of the individual analyzes. At the same time it helps us to understand important features of the two satellites.
Specifically, we describe in detail a new model for the study of the GOES weighting functions, this helps us to know the observation altitude of the satellite. We also provide a model to eliminate the noise due to the presence of the sea in the field of view of the MODIS satellite.

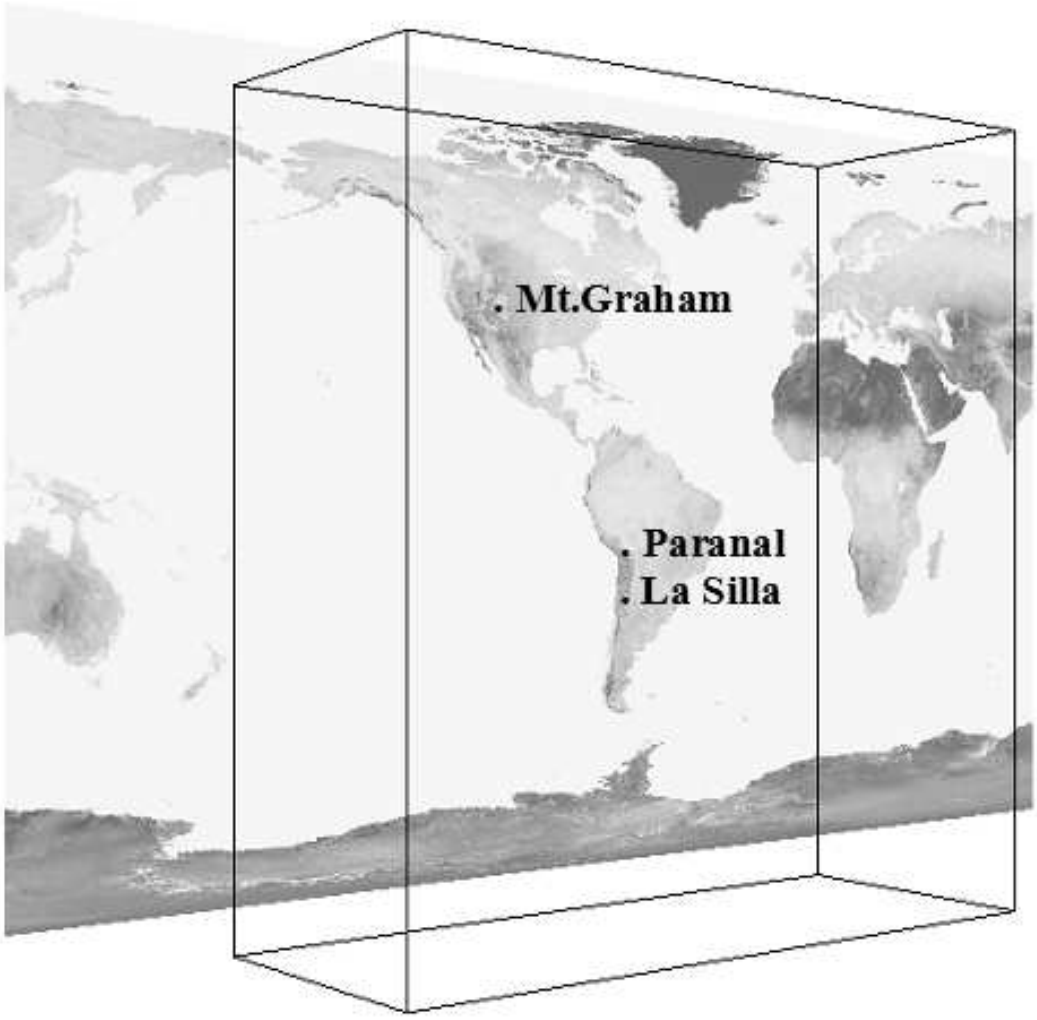

Figure 11.1: Figure shows the location of the analyzed sites. The box represents the field of view of the GOES satellite (3D McIDAS map).

Chapter 12

Satellite Data

In this thesis we use two satellites: GOES 12 and MODIS satellite. MODIS (or Moderate Resolution Imaging Spectroradiometer) is a key instrument aboard the Terra and Aqua satellites. Terra's orbit around the Earth is timed so that it passes from north to south across the equator in the morning, while Aqua passes south to north over the equator in the afternoon: in our analysis we use Aqua MODIS. Terra MODIS and Aqua MODIS are viewing the entire Earth's surface every 1 to 2 days, acquiring data in 36 spectral bands, or groups of wavelengths. The cloud cover is analyzed with the bands from 20 to 36 see Table 12.1. These data will improve our understanding of global dynamics and processes occurring on the land, in the oceans, and in the lower atmosphere. MODIS is playing a vital role in the development of validated, global, interactive Earth system models able to predict global change accurately enough to assist policy makers in making sound decisions concerning the protection of our environment. MODIS has a near-polar circular orbit at an altitude of 705 km. GOES band (see Table 12.2).

12.1 GOES data analysis

The model for GOES data analysis described in this thesis has been simplified compared to the model described in Cavazzani et al. ([2011]). This model is sufficient and more homogeneous for the comparison with the MODIS data and on the objectives of this thesis. We extrapolate the threshold σ for the classification and the correlation from the thermal night excursion (between the 23:45 and the 8:45 local time). Then we consider only the data of the 2:45 and we do the monthly trend. Finally, we classify according to the value of T_B:

Table 12.1: MODIS bands. The spatial resolution of the bands is $1km$.

Primary Use	Band	Bandwidth [μm]
Surface/Cloud Temperature		
	20	3.660 - 3.840
	21	3.929 - 3.989
	22	3.929 - 3.989
	23	4.020 - 4.080
Atmospheric Temperature		
	24	4.433 - 4.498
	25	4.482 - 4.549
Cirrus Clouds Water Vapor		
	26	1.360 - 1.390
	27	6.535 - 6.895
	28	7.175 - 7.475
Cloud Properties		
	29	8.400 - 8.700
Ozone		
	30	9.580 - 9.880
Surface/Cloud Temperature		
	31	10.780 - 11.280
	32	11.770 - 12.270
Cloud Top Altitude		
	33	13.185 - 13.485
	34	13.485 - 13.785
	35	13.785 - 14.085
	36	14.085 - 14.385

Table 12.2: GOES12 bands and resolution at Nadir.

	Window	Passband [μm]	Resolution [km]
BAND1	Visible	$0.55 \div 0.75$	4
BAND2	Microwaves	$3.80 \div 4.00$	4
BAND3	H_2O	$6.50 \div 7.00$	4
BAND4	IR	$10.20 \div 11.20$	4
BAND6	CO_2	13.30	8

- $T_B^{Max} - T_B \leq 2\sigma \Longrightarrow$ Clear
- $T_B^{Max} - T_B > 2\sigma \Longrightarrow$ Covered

So we have a single data for each night and this can be classified as clear or covered. With this classification we can extrapolate the percentages of monthly coverage.

12.2 MODIS data

MODIS data are analyzed through Giovanni Interactive Visualization and Analysis Website[1]. This tool is designed for visualization and analysis of the Atmosphere Daily Global Products. Users can generate plots or ASCII Output for Lat-Lon Map, Time Series, Hovmoller diagram, Scatter Plot, and Correlation Map. Animation is available for Lat-Lon Maps. The MODIS Science Team recommends MODIS Collection 5.1 data be used for scientific investigations. Also in this case the data are classified as Atmosphere Daily Global $1° \times 1°$ Products. This means a single image per night of a $1° \times 1°$ area.

12.3 MODIS data conversion

Giovanni Interactive Visualization and Analysis Website gives the MODIS results in terms of cloud cover percentage. To compare and correlate with GOES data we do an expansion-translation and an inversion of the data. We know that a high brightness temperature (BT) value corresponds to a low percentage of cloud cover, then the minimum value of the MODIS cloud cover corresponds to the maximum value of the GOES brightness temperature. Due to this we can compare the MODIS data with the GOES data through the formula:

$$MODIS_{T_B} = [(1 - X) \times E] + \Gamma \tag{12.1}$$

where X is the MODIS percentage of cloud cover, E is the expansion factor and Γ is the translation factor. While the expansion factor remains constant the translation factor changes every month due to the seasonal changes in temperature.

[1] http://disc.sci.gsfc.nasa.gov/giovanni

Table 12.3: Table shows the results of cloud cover at Paranal in 2009 with MODIS satellite. We see the results of the three used matrices ($100km \times 100km$). The matrix number 3 observes only ocean, the matrix 2, centered on Paranal, observes 50% sea and 50% coast and the matrix 1 observes only the Chile coast. The most reliable result and highly correlated with the GOES data is that of the matrix 1.

Paranal 2009	Matrix 1	Matrix 2	Matrix 3
Average	12%	49%	89%

12.4 MODIS ocean contribution

In this Section we show that, if in the MODIS matrix we have a ocean portion, the results of the cloud covered show a systematic error. We noted that analyzing the data at Paranal the satellite gave us a cloud cover of about 50%. This result is in contrast with all the analysis made for the same site. The error lies in the type of bands used by MODIS for the clouds analysis (see Table 12.1). The presence of a ocean portion observed at these wavelengths involves an increase of the water vapor percentage and the instrument used for data analysis interprets this as an increase in cloud cover. To confirm this result, we do a check divided into three main steps:

1. we consider the site of Paranal and analyze three different matrices shifted in horizontal (see Figure 12.1)

2. we analyze the cloud cover for the year 2009 of the same matrices.

3. we compare these trends. Figure 12.2 shows the trend of these results and Table 12.3 shows the average for the year 2009

It is evident that the presence of the ocean introduces a systematic error proportional to the water surface fraction present in the satellite field of view. Moreover, GOES and MODIS data are closely related at Mt Graham and La Silla while at Paranal (Matrix2) there are several discrepancies between the trends (see Figure 12.3). We note that some MODIS fluctuations is correlated with the GOES Band 3. In Cavazzani et al. ([2010]) and Cavazzani et al. ([2011]) we have shown that this band is not efficient for the cloud cover analysis. In fact it shows fluctuations during clear nights due to the presence of winds or other meteorological phenomena (e.g. fog or high humidity).

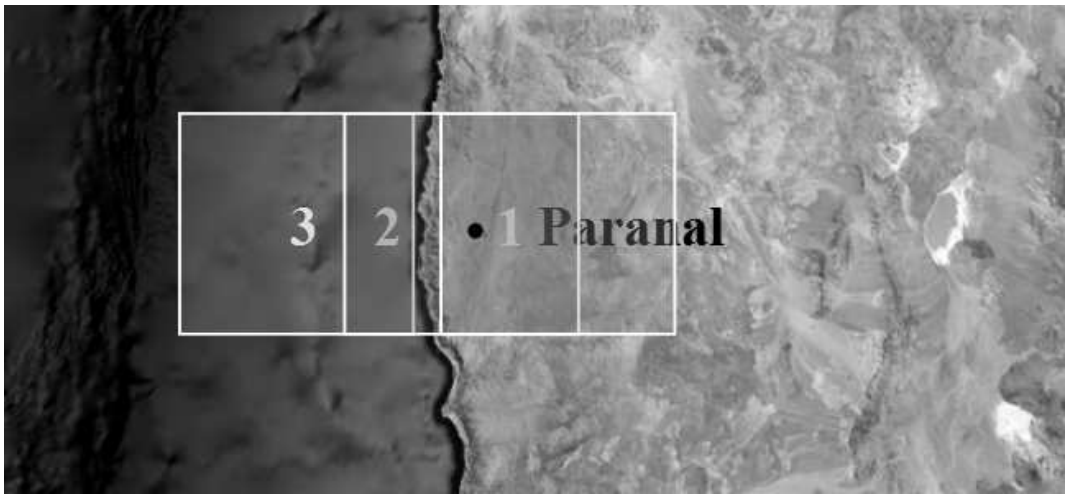

Figure 12.1: Figure shows the topographical features of the Paranal site (black dot). We see in the numbered boxes the three used matrices ($100km \times 100km$) of the MODIS satellite. The matrix number 3 observes only ocean, the matrix 2, centered on Paranal, observes 50% sea and 50% coast and the matrix 1 observes only the Chile coast.

12.5 MODIS analysis of 10 years at Paranal and La Silla

In this section we analyze and compare the MODIS data of 10 years (2002-2012) at Paranal (Matrix 1) and La Silla. We have a single point for each night. The mean of cloud cover for the 10 years are 12% at Paranal and 22% at la Silla. In Section 12.4 we have justified the displacement of the Paranal matrix: from array 2 to array 1.
Figure 12.4 shows the comparison between the cloud cover at Paranal (Matrix1) and La Silla. Top panel represents all the data of Paranal (gray trend) and La Silla (black trend): one night point for each day of the 10 analyzed years. We note the seasonal trend of the two sites due to the effects of the monsoon climate. Following the arrow of the box we can see a zoom of the year 2003. In the bottom panel we show the same data with the respective linear regressions:

$$r_{Paranal} : y = +1.209 \cdot 10^{-5}x + 0.9425$$

$$r_{La\ Silla} : y = -1.069 \cdot 10^{-5}x + 0.2323$$

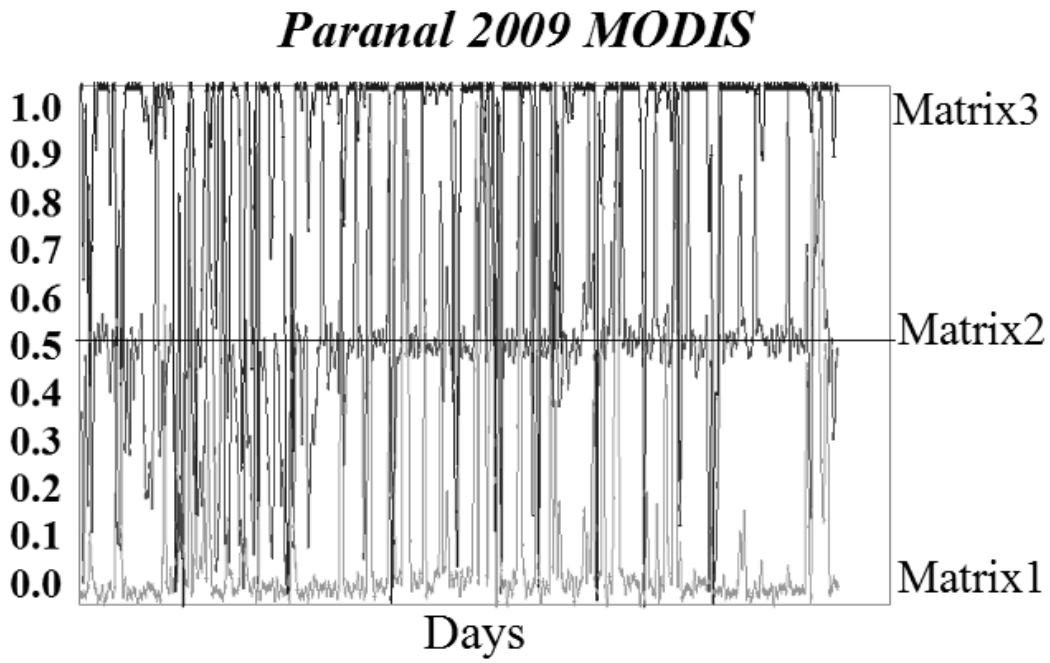

Figure 12.2: Figure shows the MODIS results of the three used matrices for the cloud cover in 2009 at Paranal. The top trend represents the results of the matrix 3 and provides a mean cloud cover of 89%, the central trend represents the results of the matrix 2 and gives a mean cloud cover of 49% and the bottom trend represents the results of the matrix 1 and gives a mean cloud cover of 12%.

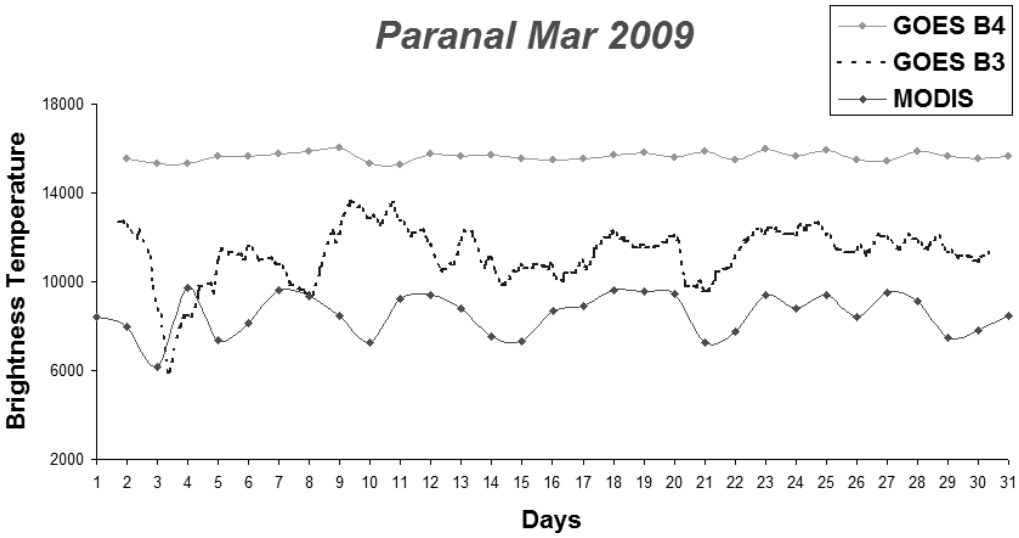

Figure 12.3: Figure shows the differences between the GOES data and the MODIS data centering both arrays on the Paranal site. The top trend shows (a single night point 2:45 local time) the results of the GOES band 4, the central trend shows the results of the GOES band 3 and finally, the bottom trend represents the MODIS data (March 2009, Paranal). We note how the data are not correlated, and also as some B3 fluctuations are correlated with the cloud covered detected by MODIS satellite. These differences are reduced if we shift the MODIS matrix, that is, if we pass from the matrix 2 to the matrix 1 (Figure 12.1).

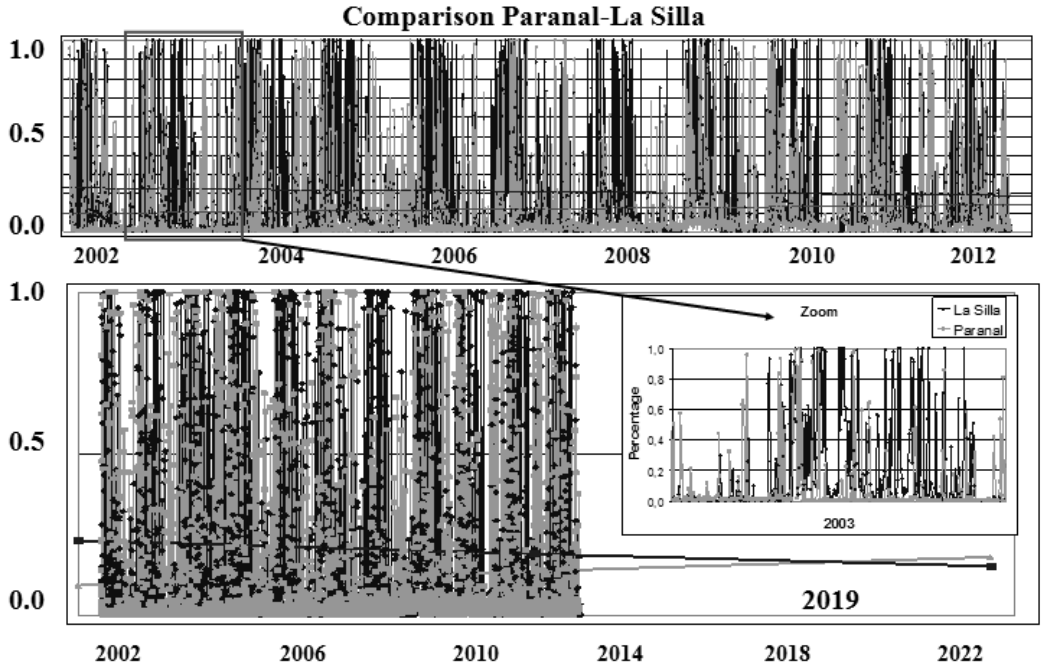

Figure 12.4: Figure shows the comparison between Paranal (Matrix 1) and La Silla 2002-2012 (MODIS data). Top panel represents all the data of Paranal (gray trend) and La Silla (black trend): one night point for each day of the 10 analyzed years. We note the seasonal trend of the two sites. Following the arrow of the box we can see a zoom of the year 2003. In the bottom panel we show the same data with the respective linear regressions. We note that the data give us an increase in cloud cover at Paranal (gray line) and a decrease at La Silla (black line). With a simple analysis we can estimate that the two trends will be intersected in the year 2019.

We note that the data give us an increase in cloud cover at Paranal (gray line) and a decrease at La Silla (black line). With a simple analysis we can estimate that the two trends will be intersected in the year 2019.

Chapter 13

MODIS-GOES Comparison

In this chapter we compare the results obtained with the analysis of the GOES data with the MODIS data. Table 13.1 shows the comparison between the GOES results and the MODIS results at Mt. Graham in 2009. In the first column we have the month, in the second column the coverage detected by GOES, in the third column the percentage of clear nights detected by GOES, in the fourth column the coverage detected by MODIS and in the fifth column the percentage of clear nights detected by MODIS. The GOES results correspond to the analysis of a single night point (2:45 local time).
Table 13.2 shows the monthly correlation coefficient at Mt. Graham in 2009.
Figure 13.1 shows the comparison between the GOES data (single night point, 2:45 local time) and the MODIS night data. We see two examples: March 2009 and May 2009 at Mt. Graham. We note that the two sets of data are related in terms of clear nights and of covered nights. While the expansion factor E remains constant the translation factor Γ changes every month due to the seasonal changes in temperature.
Figure 13.2 shows the comparison between the annual trend of MODIS data (black trend) and trend of GOES data (grey trend) at Mt.Graham in 2009. The difference shown in figure highlights that the GOES data show the cloud cover and the annual trend of temperature. Due to this the need to use monthly thresholds for the GOES data analysis. We empirically varies the translation factor to correlate the two sets of data, then if the two daily data have a difference $\geq 2\sigma$ we consider that the data is not correlated. For this analysis we associate the maximum error of one day for each month (e.g. January $(1/31) \cdot 100 = 3\%$). The mean punctual correlation is $(96 \pm 3)\,\%$.

Table 13.1: Table shows the comparison between the GOES results and the MODIS results at Mt. Graham in 2009. In the first column we have the month, in the second column the coverage detected by GOES, in the third column the percentage of clear nights detected by GOES, in the fourth column the coverage detected by MODIS and in the fifth column the percentage of clear nights detected by MODIS. The GOES results correspond to the analysis of a single night point (2:45 local time).

2009	GOES Mt.Graham		MODIS Mt.Graham	
Month	Covered	Clear	Covered	Clear
1	33	67	35	65
2	36	64	37	63
3	30	70	31	69
4	27	73	30	70
5	33	67	33	67
6	57	43	55	45
7	47	53	49	51
8	34	66	38	62
9	37	63	36	64
10	34	66	36	64
11	23	77	23	77
12	52	48	48	52
Average	37	63	38	62

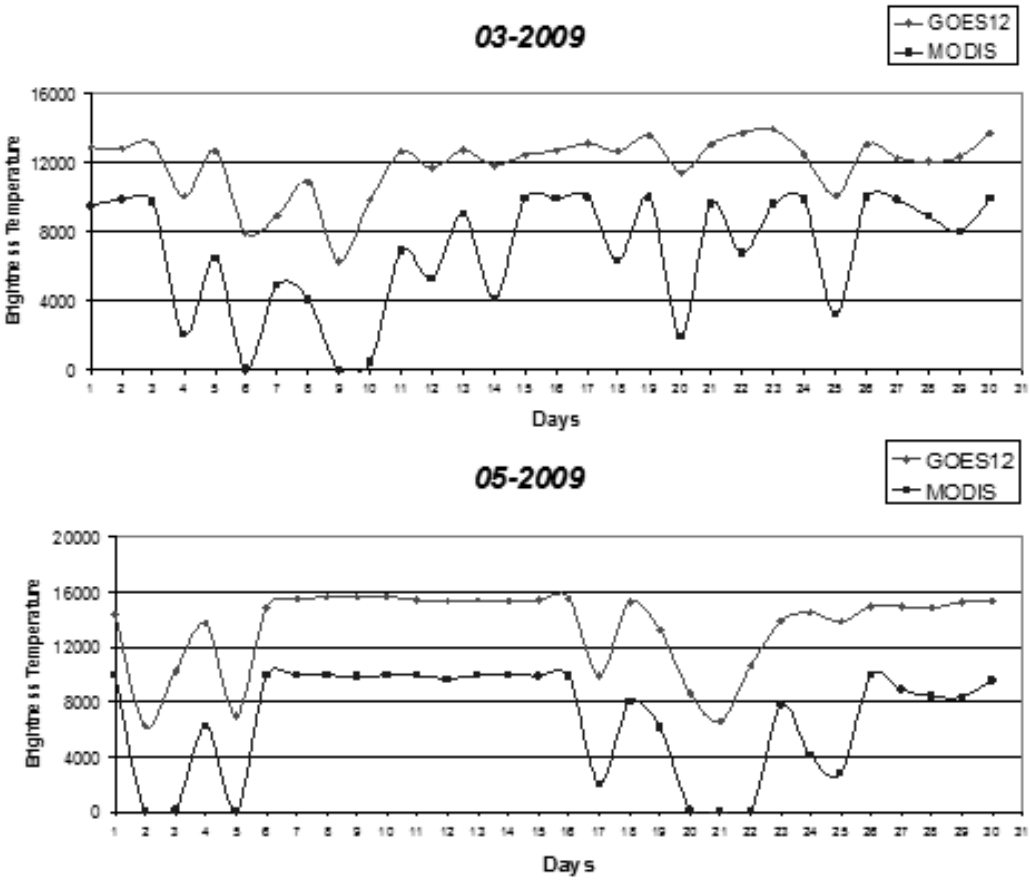

Figure 13.1: Figure shows the comparison between the GOES data (single night point, 2:45 local time) and the MODIS night data. We see two examples: March 2009 and May 2009 at Mt. Graham. We note that the two sets of data are related in terms of clear nights and of covered nights.

Table 13.2: Table shows the monthly correlation coefficient at Mt. Graham in 2009.

Month	Punctual Correlation [%]	ϵ_{Max} [%]
1	93	3
2	93	4
3	97	3
4	97	3
5	97	3
6	97	3
7	100	3
8	97	3
9	93	3
10	93	3
11	97	3
12	93	3
Average	96	3

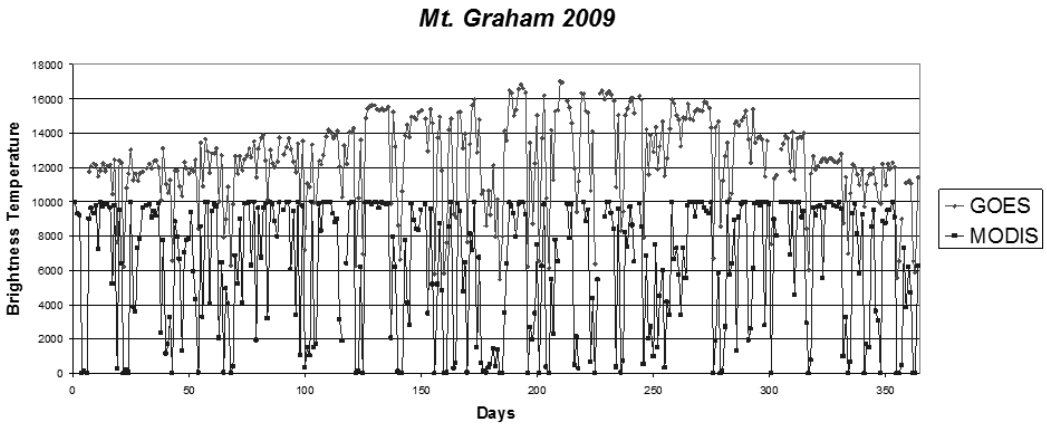

Figure 13.2: Figure shows the comparison between the trend of MODIS data (black trend) and trend of GOES data (grey trend). As we have shown the mean punctual correlation is $(96 \pm 3)\%$. The difference shown in figure highlights that the GOES data show the cloud cover and the annual trend of temperature. Due to this the need to use monthly thresholds for the GOES data analysis.

13.1 MODIS and GOES long-term comparison

In this section we analyze ten years for three sites with the MODIS satellite. We do annual averages of day and night then we compare these results with the GOES results published in Cavazzani et al. ([2010]) and Cavazzani et al. ([2011]). Table 13.3 shows this comparison. We see that there is no correlation between the day data and the night data: there are years in which the cloud cover is greater during the day than during the night and vice versa. In addition, we note that the GOES data published in Cavazzani et al. [2010] and Cavazzani et al. [2011] are in agreement with the results from the MODIS satellite. The mean difference between the percentages of cloud cover during the night provided by the two satellites is 1.6%. Figure 13.3 shows the comparison between the cloud cover during the day (gray trend) and the cloud cover during the night (black trend) for the 10 years analyzed at Mt.Graham. We can also see the respective linear regressions: gray line for the day data and the black dashed line for the night data. These trends show a decrease in cloud cover during the last 10 years. Finally we can see the comparison with GOES data trend (dark gray with triangles) of the three analyzed years ($2007 - 2008 - 2009$): the differences with the MODIS night data are $\leq 2\%$. The use of both satellites allows us to have more information on each site. The high obtained correlation gives us a mutual confirmation of the used models for the two satellites. Figure 13.4 shows the difference between the GOES temporal resolution (top trend) and the MODIS temporal resolution (bottom trend) Figure 13.4 also shows the trend of the daily average of the GOES data (dashed trend). This dashed trend is closely correlated with the MODIS data. This fact justifies the statistical comparison between our previous models and the MODIS data elaborated in this thesis. We can also note how a single night point can be used for statistical analysis, but as this is insufficient to analyze the temporal evolution of a night. For example, if we consider the night of 9 or 11 October shown in the Figure 13.4, we see as the single point of a polar satellite is not sufficient for a detailed analysis of the night characteristic.

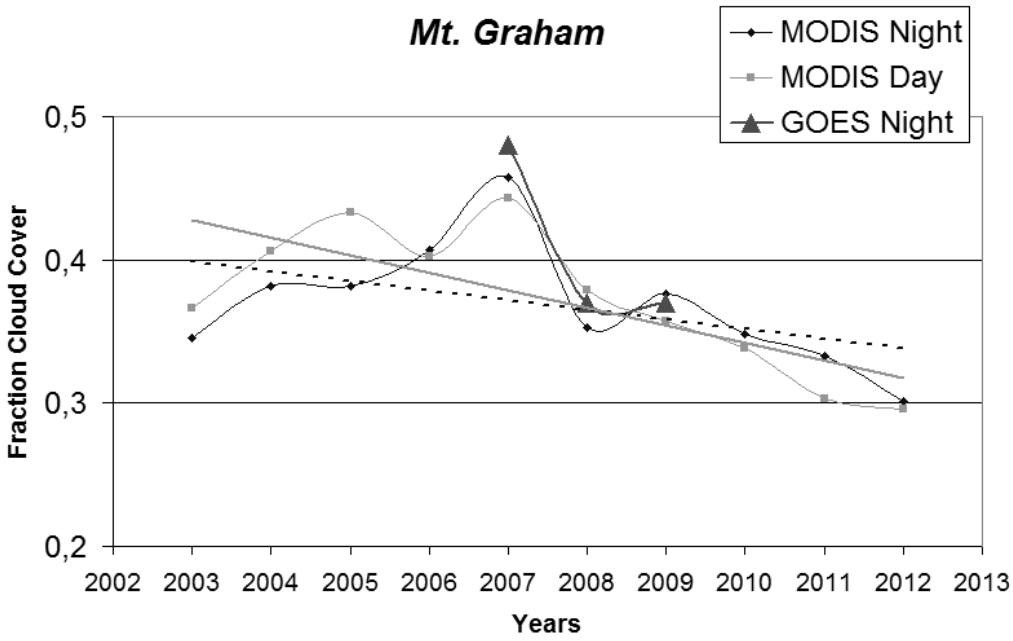

Figure 13.3: Figure shows the comparison between the cloud cover during the day (gray trend) and the cloud cover during the night (black trend) for the 10 years analyzed at Mt.Graham. We can also see the respective linear regressions: gray line for the day data and the black dashed line for the night data. These trends show a decrease in cloud cover during the last 10 years. Finally we can see the comparison with GOES data trend (dark gray with triangles) of the three analyzed years ($2007 - 2008 - 2009$): the differences with the MODIS night data are $\leq 2\%$.

Table 13.3: Table shows the MODIS results of 10 years for the analyzed sites. Table also shows the comparison with the results obtained in Cavazzani et al (2010) and Cavazzani et al (2011). Table is divided into three groups of 5 lines. In the first line of each group we give the studied site, in the second line we give the analyzed year, in the third line we give the annual average of cloud cover during the day, in the fourth line we give the annual average of cloud cover during the night and in the fifth line we give the GOES results of the cloud cover during the night.

Paranal											
Year	2003	2004	2005	2006	2007	2008	2009	2010	2011	2012	Average
MODIS Day	0.09	0.11	0.12	0.08	0.20	0.14	0.11	0.08	0.09	0.08	0.11
MODIS Night	0.09	0.10	0.14	0.09	0.14	0.09	0.11	0.13	0.16	0.15	0.12
GOES12 Night					0.15	0.09	0.10				
La Silla											
Year	2003	2004	2005	2006	2007	2008	2009	2010	2011	2012	Average
MODIS Day	0.21	0.22	0.30	0.24	0.27	0.25	0.24	0.20	0.22	0.20	0.23
MODIS Night	0.20	0.23	0.26	0.21	0.25	0.19	0.22	0.19	0.22	0.19	0.22
GOES12 Night					0.30	0.18					
Mt. Graham											
Year	2003	2004	2005	2006	2007	2008	2009	2010	2011	2012	Average
MODIS Day	0.37	0.41	0.43	0.40	0.44	0.38	0.36	0.34	0.30	0.30	0.37
MODIS Night	0.35	0.38	0.38	0.41	0.46	0.35	0.38	0.35	0.33	0.30	0.37
GOES12 Night					0.48	0.37	0.37				

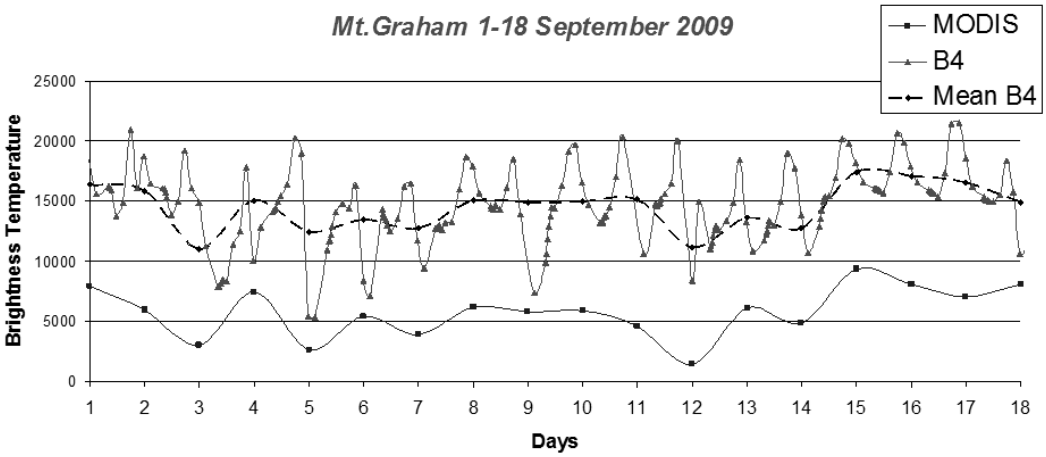

Figure 13.4: Figure shows the difference between the GOES temporal resolution (top trend) and the MODIS temporal resolution (bottom trend) Figure also shows the trend of the daily average of the GOES data (dashed trend). This dashed trend is closely correlated with the MODIS data. We can note how a single night point can be used for statistical analysis, but as this is insufficient to analyze the temporal evolution of a night.

Chapter 14

Conclusion

We have described in the first part of this thesis a new type of analysis for the sites characterization.
We used data from two satellites: the geostationary satellite GOES 12 and the polar satellite MODIS.
This analysis is divided into 6 main steps:

1. Collect satellite and ground data (see Chapter 1).

2. Analysis of satellite data (see Chapters 2 and 3): in this part we have improved the previous models for the site testing.
   We have introduced three main original contributions, the remote sounding of three bands with a detailed study of weighting functions that characterize these bands.
   In particular, we have shown that these bands observed at a high altitude (4000m).
   Thanks to this hypothesis, we introduced the use of a 100km x 100km matrix. The use of this matrix has been justified by the high correlation between it and the single pixel centered over the site (95%).
   The matrix has allowed the reduction of the satellite noise, the opportunity to observe the entire sky above the site increasing the temporal resolution of the model, and through the stadard deviation of its pixels, has allowed us the detection of subtle phenomena.
   The third original contribution was the introduction of monthly thresholds instead of annual thresholds. This has reduced the error due to seasonal variations in temperature.
   In addition, this threshold is extrapolated directly from the satellite data, then the model does not need additional measurements with balloons, weather stations, etc.

Table 14.1: Satellite Mean Monthly Percentage (2007-2008-2009).

	Paranal		La Silla		La Palma		Mt.Graham		Tolonchar	
	Clear	Stable	Clear	Stable	Clear	Stable	Clear	Stable	Clear	Stable
Mean 2007	85	69	70	69	74	72	53	52	84	74
Mean 2008	91	70	82	73	71	69	65	61	89	80
Mean 2009	91	80			67	62	63	60		

Table 14.2: Satellite Mean Monthly Percentage (2008-2009).

	Izaña		SPM		Leoncito		SAC	
	Clear	Stable	Clear	Stable	Clear	Stable	Clear	Stable
Mean 2008	73	66	79	74	73	69	72	62
Mean 2009	64	59	73	65	68	61	68	58

3. We have validated the model using Paranal and La Palma ground data. We have made a punctual correlation between the satellite image and the corresponding ground data. We have obtained a punctual error $\leq 5\%$ and a statistical error $\leq 2\%$ for the analyzed sites.

4. Through this model, we analyzed 3 bands x (about) 5 images for each day x 365 x 2 (or 3) years x 9 Sites = about 100000 processed GOES images. Tables 14.1 and 14.2 summarize the obtained results.

5. Thanks to the remote sounding we extrapolated the atmospheric correlation function. This function allows us the satellite subclassification of the stable nights (photometric nights) from the the clear nights (spectroscopic nights).
   This function is related to the seeing and the wind at the ground. With this correlation we have described two empirical models for the satellite measurement of the seeing (at Paranal and La Palma) and the wind (at SAC): see Chapters 7, 8 and 9.
   We did the validation with the ground data in the model for the seeing measurement.
   The wind model was calibrated with Paranal ground data and then it has been applied at SAC. In fact we do not have any ground data at SAC.

6. Finally, we analyzed MODIS data and we made a correlation between the two satellites: we have obtained a correlation of 97% at Mt. Graham in 2009.
   This result for a site that has various climatic conditions has allowed us to cross-validate the two satellites. A model that uses polar and geostationary satellite data allows us to overcome the respective limits

of the two groups of satellites. GOES has a high temporal resolution while the MODIS field of view covers the entire Earth's globe.
One MODIS disadvantage is that its data are provided as "black box", on the other hand the MODIS data analysis is very fast compared to the analysis of GOES images.
Thanks to this, in the last part of the thesis, we have made a long term analysis (see Chapter 11). We have analyzed 10 years (2003-2012) at Paranal, La Silla and Mt. Graham. This analysis showed a negative trend in cloud cover at La Silla and Mt.Graham, and a positive trend at Paranal.

In conclusion, the first part of this thesis describes a new model for analysis of Earth's atmosphere. This model has been used in particular for the cloud cover analysis, this is very important because there are no meteorological database on the night cloud cover at astronomical sites and it's very difficult to separate the components of the infrared emission (ocean, ground, cloud and atmosphere). The study of WFs combined with the remote sounding of the 3 bands has improved the infrared emission knowledge detected by satellites. Finally, the use of a matrix and the introduction of a autocalibrated monthly thresholds has reduced the error compared to previous models for the site testing. In the future work we will analyze other sites and we will implement the observation period for the long-term satellite analysis. In addition, we will try to improve the semi empirical models for the seeing and wind measurement. At the moment we only have physical hypotheses, but in the future we will try to develop a robust physical theory for the satellite study of the winds and the atmospheric turbulence.

Part II

Photon Propagation Properties

Chapter 15

Fluctuations of Photon Arrival Times in Free Atmosphere

In this chapter we calculate the delay of the arrival times of visible photons on the focal plane of a telescope and its fluctuations as function of local atmospheric conditions (temperature, pressure, chemical composition, seeing values) and telescope diameter. The aim is to provide a model for delay and its fluctuations accurate to the picosecond level, as required by several very high time resolution astrophysical applications, such as comparison of radio and optical data on Giant Radio Bursts from optical pulsars, and Hanbury Brown Twiss Intensity Interferometry with Cerenkov light detectors. The results here presented have been calculated for the ESO telescopes in Chile (NTT, VLT, E-ELT), but the model can be easily applied to other sites and telescope diameters. Finally, we describe a theoretical mathematical model for calculating the Fried radius through the study of delay time fluctuations.
Several high time resolution instruments are able to measure the arrival time of visible photons with an internal precision in the range 10 - 100 picoseconds, and refer those arrivals to the commonly used UTC scale with an accuracy of the order of 500 picoseconds (see for instance, Barbieri et al. [2010] and Naletto & Barbieri, [2009]).
The step of referring the arrival times to UTC is usually done with the intermediary of time signals broadcasted over radio frequencies (e.g. GPS, GLONASS, Galileo GNSS), signals which are very accurately corrected for atmospheric propagation effects like ionospheric scintillation and wet troposphere refraction. In the usual astronomical applications, the arrival times of optical photons are not corrected to the same accuracy.
The possibility to perform such correction is actually shown by accurate laser ranging to geodetic satellites (recall that 1 nanosecond in vacuum corresponds to 30 cm). For instance, Kral et al. ([2005]) quote a precision of

few picoseconds by taking into account the atmospheric seeing. Moreover a recent discussion has been performed by Dudy D.Wijaya and Fritz K. Brunner ([2011]) on the atmospheric range correction for two-frequency Satellite Laser Ranging (SLR) measurements.
Motivated by our own very precise time measurements on celestial sources with Aqueye and Iqueye ([2010] and Naletto & Barbieri, [2009]), we have undertaken the calculation of the delay and delay dispersion of visible photon arrival times in the usual conditions prevailing in astronomical observatories. In the first step of our procedure, the Marini-Murray model (Marini & Murray, [1973]) is used to calculate the correction ΔR to the optical path of photons in air.
Through this calculation, the atmospheric refractive index n and a fixed delay time independent of the photometric night quality is derived. Then the photon paths are correlated with the astronomical seeing.
Through this relation we derive a statistical set of delay times as function of the Fried radius r_0 and telescope diameter. Finally, the difference of these delay times with the fixed delay gives the fluctuations.
Reversing this model we also developed a theoretical mathematical model for the r_0 calculating through the observation of these fluctuations.

15.1 MARINI-MURRAY Model for the Refraction Correction

The Marini-Murray model is based on an expansion of hypergeometric functions (Marini & Murray, [1973]). The model relies on hydrostatic equilibrium and the barometric equation. It considers a hydrostatic water vapor distribution and the water vapor behavior such as that of an ideal gas. The refraction correction is given as a function of temperature, pressure, vapor partial pressure, gravity acceleration and universal gas constant. The model also includes the values of water vapor molar mass and air average molar mass. Finally the refraction correction is calculated in relation to the Earth radius, the site altitude and latitude. Through these parameters we can determine Optical Path Length (OPL) correction as described in detail below. According to the original Marini-Murray model, the refraction correction $\Delta R = R_1 - R$ (see Fig. 15.1), is calculated as:

$$\Delta R = \frac{f(\lambda)}{g(\phi, H)} \left[\frac{g_1 + g_2 + g_3}{sin(\theta_\omega) + \frac{\frac{g_2}{g_1+g_2+g_3}}{sin(\theta_\omega)+0.01}} \right]$$

where g_1, g_2, g_3 and $g(\phi, H)$ are defined below, θ_ω is angle of elevation, ϕ is the latitude and H is the altitude of the observatory. The several terms are defined as:

- $g_1 = 80.343 \cdot 10^{-6} \left[\frac{R_G}{M_d \cdot \vec{g}} P + (1 - \frac{M_\omega}{M_d}) \frac{R_G}{4 M_d \cdot \vec{g}} P_\omega \right]$
- $g_2 = 10^{-6} \left[\frac{80.343 \cdot R_G}{R_E \cdot M_d^2 \cdot \vec{g}^2} P \cdot T \cdot K(\phi, T, P) \right] + 10^{-6} \left[10^{-12} \frac{80.343^2 \cdot 2 R_G \cdot P^2}{4 M_d \cdot \vec{g} \cdot T (3 - \frac{1}{K(\phi, T, P)})} \right]$
- $g_3 = -10^{-6} \left[\frac{11.3 \cdot R_G}{g(\phi, H) \cdot 4 M_d \cdot \vec{g}} P_\omega \right]$

where:

- $g(\phi, H) = 1 - 0.0026 \cdot cos(2\phi) - 0.00031 \cdot H$
- $K(\phi, T, P) = 1.163 - 0.00968 \cdot cos(2\phi) - 0.00104 \cdot T - 0.00001435 \cdot P$

In the original model the function $f(\lambda)$ was defined by with the following formula:

$$f(\lambda) = 0.965 + \frac{0.0164}{\lambda^2} + \frac{0.000228}{\lambda^4}$$

However, the refraction index formula used in the original Marini-Murray formalism is valid for a limited wavelength range ($0.40 \mu m \div 0.60 \mu m$). This is due to the model assumptions. For this reason, Ciddor ([1996]) devised a more refined model valid for a wider wavelength range ($0.30 \mu m \div 2.00 \mu m$). This refined model is described by the formula (Riepl et al. [2001]):

$$\Delta R = f_{Gr}(\lambda) \left[\frac{g_1 + g_2}{sin(\theta_\omega) + \frac{\frac{g_2}{g_1 + g_2}}{sin(\theta_\omega) + 0.01}} + \frac{g_3}{sin(\theta_\omega)} \right] \tag{15.1}$$

where the dispersion formula, taken from Ciddor ([1996]) normalized to the wavelength of $0.6943 \mu m$, gives:

$$f_{Gr}(\lambda) = \frac{k_1 (k_0 + (\frac{1}{\lambda})^2)}{(k_0 - (\frac{1}{\lambda})^2)^2} + \frac{k_3 (k_2 + (\frac{1}{\lambda})^2)}{(k_2 - (\frac{1}{\lambda})^2)^2} \tag{15.2}$$

The values of the involved a-dimensional constants resulting from the normalized dispersion formula are:
k_0=238.0185, k_1=205.0638, k_2=57.362 and k_3=5.944936.
In the formulae, $T\,[K]$ is the temperature, $P\,[mb]$ is the total pressure, and $P_\omega\,[mb]$ is the water vapor partial pressure, $\vec{g} = 9.784 \left[\frac{m}{s^2} \right]$ is the acceleration of gravity at the equator. The gas constant is taken as $R_G = 8314.36 \left[\frac{mJ}{K} \cdot mol \right]$. The following molecular values are used:

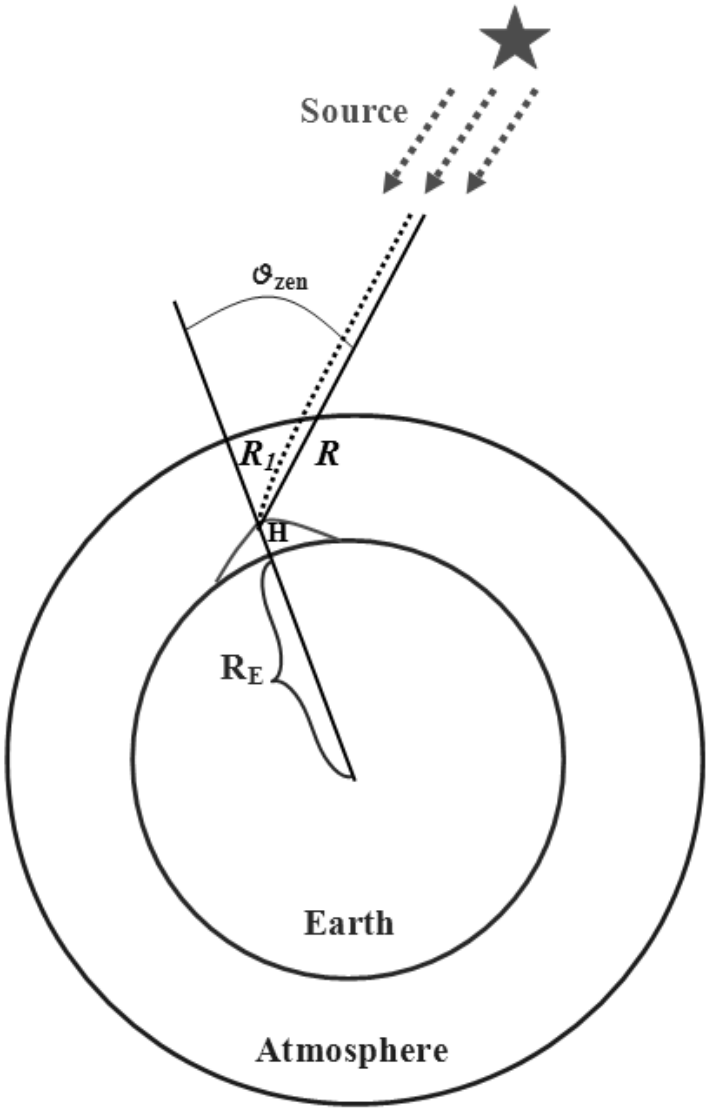

Figure 15.1: Optical path length (OPL) R and its variation ΔR due to atmospheric refraction. R is the OPL in vacuum, R_1 is the OPL in atmosphere, R_E is the Earth radius which the model calculates according to the latitude, θ_{zen} is the Zenith angle and H is the site altitude.

- $M_\omega = 18.016 \left[\frac{g}{mol}\right] \Rightarrow$ Water vapor
- $M_d = 28.966 \left[\frac{g}{mol}\right] \Rightarrow$ Air average.

Equation 15.1 fills the Marini-Murray simplifications with a hybrid approach in which the dry and wet refraction delays are treated separately.

15.2 Refractive Index and Delay Time Calculation

Through the refraction correction path ΔR we can calculate, in a first approximation, the mean atmospheric refractive index n_1. In fact, we note that the n_1 fluctuation is of the order of 10^{-9} for 1 ps (see Section 16.0.5). If we assume that n_1 has a constant distribution:

$$n_1 = \frac{OPL + \Delta R}{OPL} \tag{15.3}$$

where the geometric optical path length (OPL) is given by the formula:

$$OPL = \frac{AA - SA}{cos(\theta_{zen})} \tag{15.4}$$

where:

- AA=Atmosphere indicative thickness (In this thesis we have considered the $AA = 10Km$)
- SA=Site altitude

The refractive angle θ_1 is then calculated as:

$$\theta_1 = arcsin\left(\frac{1}{n_1}\right)$$

With the value of the refractive index n_1 the delay time t_1 is calculated through the formula:

$$t_1 = \frac{n_1 \cdot OPL}{c/n_1} - \frac{OPL}{c} \tag{15.5}$$

where c is the velocity of light in vacuum $\left(c = 299792.458 \left[\frac{Km}{s}\right]\right)$. Equation 15.5 allows us to calculate the propagation delay time in the atmosphere as a function of the refractive index n, including the geometric effects.
The first term in Equation 15.5 is the ratio between the geometric OPL and the speed of light in the atmosphere. The main contribution of the delay time comes from the denominator of this ratio.

15.3 Application of the model to ESO astronomical sites for the delay time

In this Section we calculate the delay time for the three Chilean sites of ESO telescopes. Table 15.1 shows the sites characteristics. We assume an average ground temperature of 288 K and an average ground relative humidity of 20% for the three sites. Table 15.2 shows the obtained values from the simulation (through the Equation 15.5) at different Zenith angles. The delay time is calculated as a function of wavelength ($\lambda = 0.632\mu m$) and has been calculated for a zenith angle ranging from 0° to 60°. The data show the increase of the delay time with the θ_{zen} following the trend of the *cos* function. We note that this delay does not depend on the telescope diameter and has variations in the order of $10^{-2}ns$ between Paranal and La Silla. These variations are due to the difference in altitude and geographical coordinates of the sites.

15.4 Calculation of the Fried parameter and Seeing

The atmospheric optical turbulence introduces variations on t_1 according to refraction fluctuations. We now recall one of the main parameters of the astronomical seeing, namely the Fried's radius r_0, which defines the average size of the turbulent cell. This parameter will be useful to introduce the concept of photons delay time fluctuations. Fried has shown (Fried, [1965]), within the limits of validity of the Kolmogoroff law, that r_0 is expressed by the formula:

$$r_0 = \left[0.423 \cdot \frac{4\pi^2}{\lambda^2} \cdot \frac{1}{cos(\theta_{zen})} \int C_n^2 \cdot dz\right]^{-\frac{3}{5}} \tag{15.6}$$

where C_n^2 is the refractive index structure parameter:

$$C_n^2 = \left[80 \cdot 10^{-6} \frac{P}{T}\right] \cdot C_T^2$$

and the temperature structure parameter $C_T^2(x)$ is defined through the formula:

$$C_T^2(x) = \frac{[T(x) - T(x + \Delta x)]^2}{\Delta x^{-\frac{2}{3}}}$$

this parameter is expressed in $(°C)^2 \cdot m^{-\frac{2}{3}}$ and expresses the temperature variations between two locations at a distance Δx.

Table 15.1: Geographic Characteristics of the Sites.

Site	LAT.	LONG.	Altitude Km	Telescope Diameter m
La Silla	$-29°15'$	$-70°43'$	2.347	3.58
Paranal	$-24°37'$	$-70°24'$	2.630	8.20
Armazones	$-24°35'$	$-70°11'$	3.064	42.00

Table 15.2: Delay time vs Zenith angle for different sites ($\lambda = 0.632\mu m$). We note that this delay time does not depend on the telescope diameter and varies slightly with the location of the site.

Zenith Angle	(°)	0	15	30	45	60
La Silla	(ns)	15.53	16.24	18.58	23.14	30.72
Paranal	(ns)	15.52	16.23	18.57	23.13	30.71
Armazones	(ns)	15.52	16.23	18.57	23.13	30.71

15.5 Seeing effects on the images

The seeing produces scintillation, smearing and motion of the image. Roddier (Roddier, [1981]) has obtained the following approximate expressions for the calculation of these three effects.

15.5.1 Scintillation

The image scintillation, as a function of C_n^2, in approximation is given by the following formula:

$$\frac{\sigma_I^2}{I} \propto D^{-\frac{7}{3}} \cdot \frac{1}{(cos(\theta_{zen}))^3} \cdot \int C_n^2(z) \cdot z^2 \cdot dz$$

where D is the diameter of the telescope. Scintillation however does not affect the dispersion of the arrival times, and therefore is not taken further into account.

15.5.2 Image Smearing

The light from the point source is spread over an area having a Full Width Half Maximum (FWHM) given by:

$$FWHM = 0.98\frac{\lambda}{r_0}$$

The value is in *arcsec*. The amplitude of this effect is independent of the pupil diameter.

15.5.3 Image Motion

The motion of the image, as a function of λ, telescope diameter (D) and r_0, is given by:

$$\sigma^2(x) = \sigma^2(y) = 0.18 \cdot \lambda^2 \cdot D^{-\frac{1}{3}} \cdot r_0^{-\frac{5}{3}} \tag{15.7}$$

This motion is in *arcsec*, and can be expressed in linear units (*meters*) by means of the formulae:

$$\Delta x = n_1 \cdot OPL \cdot sin\sqrt{\sigma^2(x)}$$

$$\Delta y = n_1 \cdot OPL \cdot sin\sqrt{\sigma^2(y)}$$

The latter effect is very important for the fluctuation of delay times. One can calculate a new optical path as a function of this image motion, and then a new delay time (See Figure 16.1). Figure 16.1 shows the optical path length in vacuum and the graphical representation (not to scale) of its variations. We define $OPL_1 = n_1 \cdot OPL$ and $OPL_2 = n_2 \cdot OPL$, where n_1 is calculated using the Marini-Murray model (see Formula 15.3) and OPL through the Formula 15.4. The difference between the previously calculated time and this new one gives the fluctuation. The total motion is given by the formula:

$$\Delta = \sqrt{\Delta^2 x + \Delta^2 y} \tag{15.8}$$

This motion is $<< OPL$, then we can calculate the new OPL through the formula:

$$OPL_2 = \sqrt{OPL_1^2 + \Delta^2} \tag{15.9}$$

where:

$$OPL_1 = n_1 \cdot OPL.$$

Chapter 16

Geometric and Physical Delay Time Fluctuation

In this chapter we calculate the delay time fluctuation. It is due to two contributions: one correction is due to the change in photon path (geometric), and the other (physical) is due to the fact that the photon is traveling in a medium where the refractive index is changed. The delay time ($t_{2,G}(r_0, D)$) due only to the geometric variation of the OPL is given by:

$$t_{2,G}(r_0, D) = \frac{n_1 \cdot OPL_2}{c} - \frac{OPL}{c}$$

Through this new time we get the geometric fluctuation of the delay time $\Delta t_G(r_0, D)$:

$$\Delta t_G(r_0, D) = |t_{2,G}(r_0, D) - t_1| \tag{16.1}$$

Taking into account that:

$$t_1 = \frac{n_1 \cdot OPL_1}{c} - \frac{OPL}{c}$$

we obtain the following formula:

$$\Delta t_G(r_0, D) = \frac{n_1}{c} \cdot |OPL_2 - OPL_1| \,. \tag{16.2}$$

16.0.4 Physical delay time fluctuation

In this Section, we calculate the delay time ($t_{2,P}(r_0, D)$) due to the physical variation of the atmosphere. In the previous section we saw how the OPL changes due to the atmosphere (image motion). The change in OPL also

induces a change in the refractive index. In fact, fluctuations in optical path length must correspond to refractive angle variations. We can calculate the refractive angle fluctuation assuming the atmosphere uniform distribution:

$$\Delta\theta = arcos\left[\frac{OPL_1}{\sqrt{OPL_1^2 + \Delta^2}}\right] \tag{16.3}$$

The corresponding atmospheric refractive index n_2, obtained by Snell's law, is:

$$n_2(r_0, D) = \frac{n_1 sin\theta_1}{sin(\theta_1 + \Delta\theta)} \tag{16.4}$$

This refractive index is a function of r_0 and the telescope diameter(D).

16.0.5 Calculation of physical delay time fluctuation

With the value of the refractive index n_2 (Equation 16.4) we can calculate a new physical delay time as a function of the r_0 and the telescope diameter (D), through the formula:

$$t_{2,P}(r_0, D) = \frac{n_2 \cdot OPL}{c/n_2} - \frac{OPL}{c}$$

where OPL is given by the Formula 15.4. Then, as in Section 16, we obtain the fluctuation due to this variation $\Delta t_P(r_0, D)$:

$$\Delta t_P(r_0, D) = |t_{2,P}(r_0, D) - t_1| \tag{16.5}$$

where:

$$t_1 = \frac{n_1 \cdot OPL_1}{c} - \frac{OPL}{c}$$

we obtain:

$$\Delta t_P(r_0, D) = \frac{OPL}{c} \cdot \left|n_2^2 - n_1^2\right|. \tag{16.6}$$

Through the Formula 16.6 we can estimate that a delay time fluctuation of 10.0 ps corresponds to a refractive index variation Δn of 3.3×10^{-8}. This gives an idea of the error propagation.

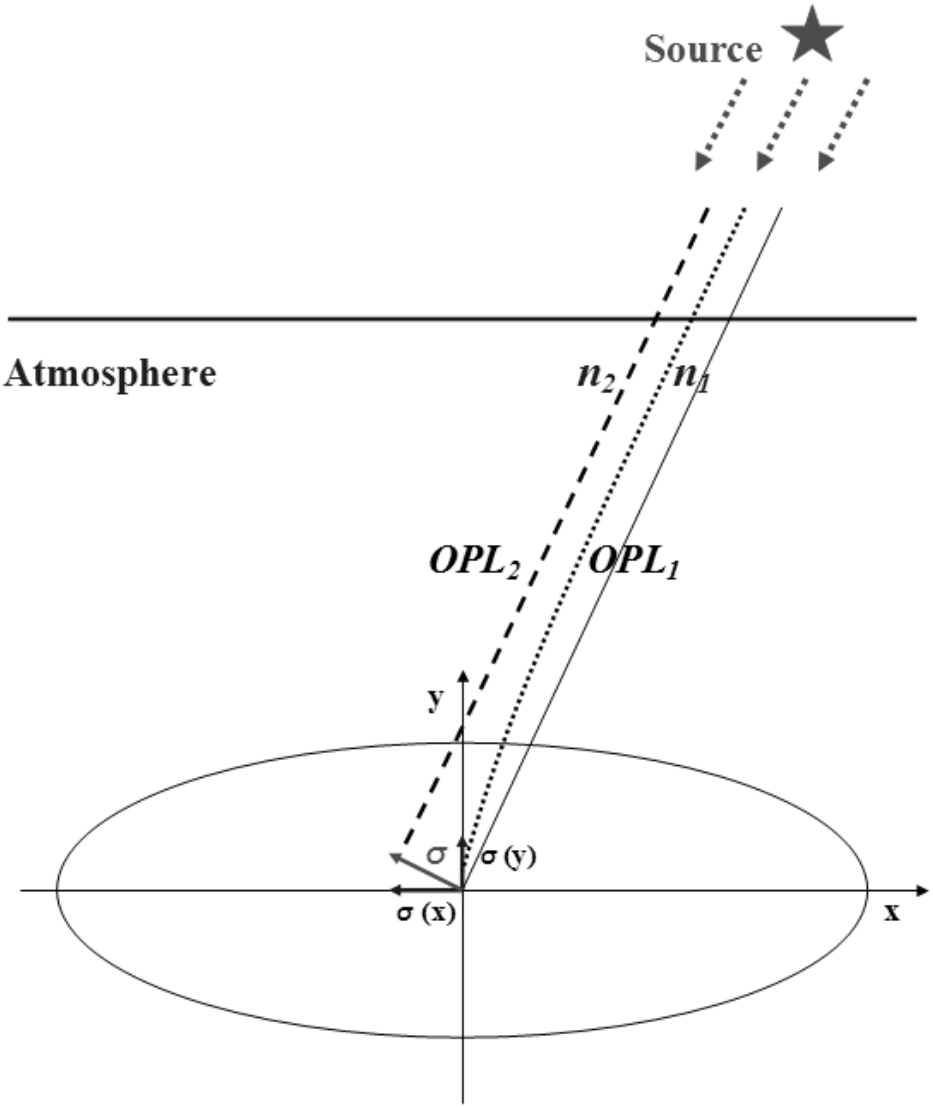

Figure 16.1: Schematic diagram of the OPL variation due to the image motion. Figure shows the optical path length in vacuum and the graphical representation (not to scale) of its variations. We define $OPL_1 = n_1 \cdot OPL$ and $OPL_2 = n_2 \cdot OPL$. Considering the motion of the image $\sigma << r_0$ we can assume that relevant x and y refractive index gradients are unexpected.

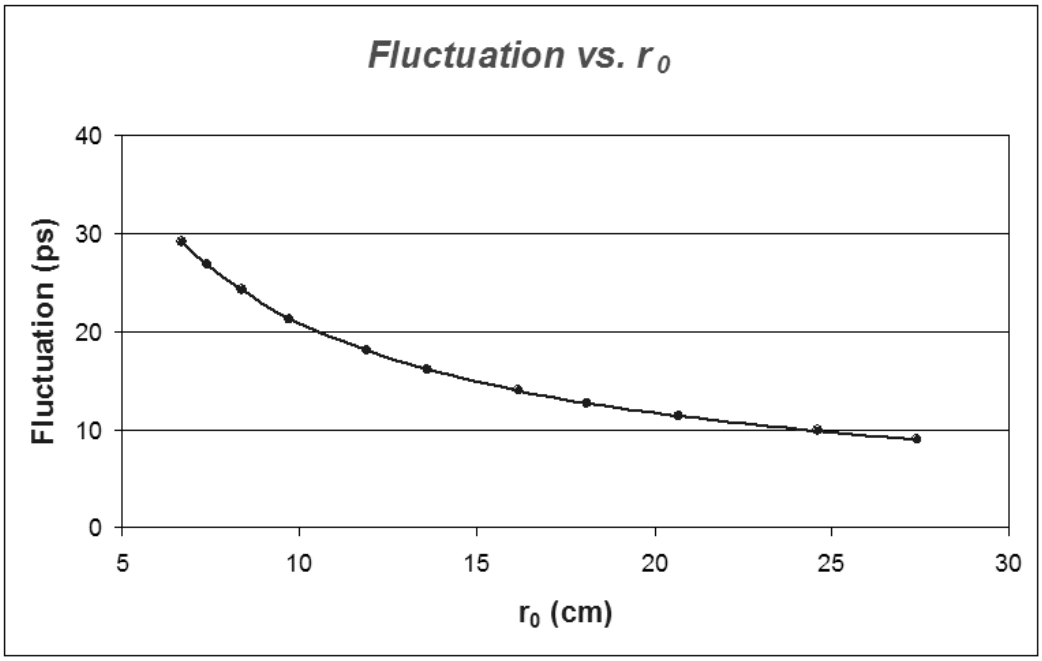

Figure 16.2: Fluctuation delay time as a function of the r_0. This simulation pertains to La Silla ($\lambda = 0.632\mu m$, Zenith angle $= 10°$).

Table 16.1: Fluctuation vs Zenith angle for different sites ($\lambda = 0.632\mu m$, $r_0 = 15cm$).

Zenith Angle	(°)	0	15	30	45	60
La Silla (3.58m)	(ps)	9.8	10.4	12.4	16.9	27.5
Paranal (8.20m)	(ps)	8.2	8.7	10.4	14.2	23.1
Armazones (42.00m)	(ps)	5.8	6.1	7.3	9.9	16.2

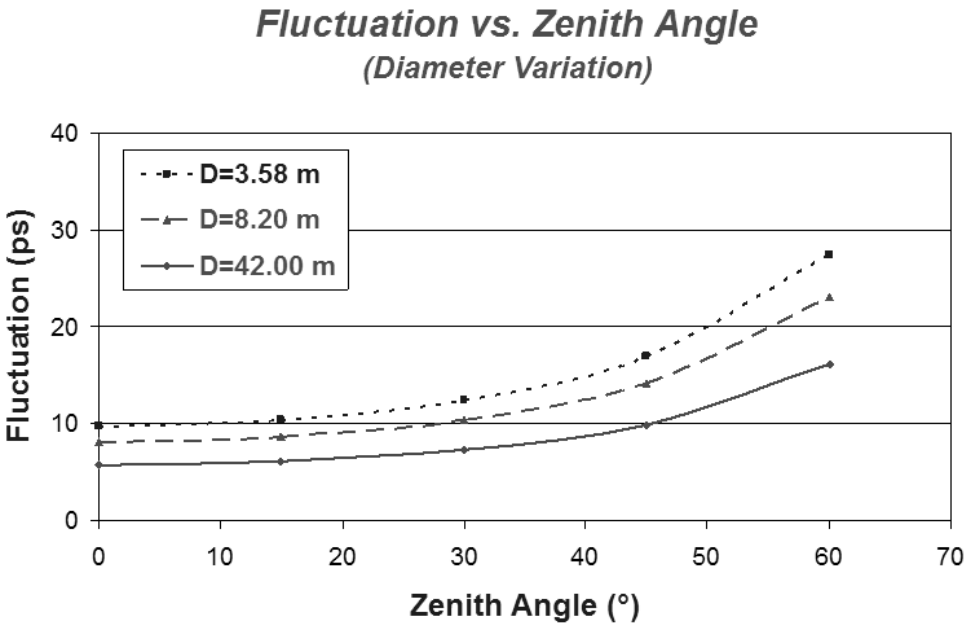

Figure 16.3: Delay time fluctuation as a function of the telescope diameter and the Zenith angle variation ($\lambda = 0.632\mu m$, $r_0 = 15cm$). The simulation compares La Silla (NTT), Paranal (VLT) and Armazones (ELT).

16.1 Calculation of delay time fluctuations

Consequently, the total fluctuation of the delay time is the sum of the geometric and physical component:

$$\Delta t_F = \Delta t_G + \Delta t_P$$

In this sum the physical component is larger than the geometric component of four orders of magnitude. Finally, we express this fluctuation through the extended formula:

$$\Delta t_F(r_0, D) = \frac{n_1^2 \cdot OPL}{c} \left| \sqrt{2} sin \sqrt{K \cdot \lambda^{\epsilon} \cdot D^{-\frac{\alpha}{\beta}} \cdot r_0^{-\frac{\gamma}{\eta}}} - 1 \right| +$$

$$+ \frac{OPL}{c} \cdot \left| \left[\frac{n_1 sin\theta_1}{sin(\theta_1 + \Delta\theta)} \right]^2 - n_1^2 \right| \tag{16.7}$$

where:

$$\Delta\theta = arcos \left[\left(2sin^2 \sqrt{K \cdot \lambda^{\epsilon} \cdot D^{-\frac{\alpha}{\beta}} \cdot r_0^{-\frac{\gamma}{\eta}}} + 1 \right)^{-\frac{1}{2}} \right]$$

Substituting the constants with these values (Roddier, [1981]) $K = 0.18$, $\alpha = 1$, $\beta = 3$, $\gamma = 5$, $\eta = 3$ and $\epsilon = 2$ we obtain the final formula used in the model:

$$\Delta t_F(r_0, D) = \frac{n_1^2 \cdot OPL}{c} \left| \sqrt{2} sin \sqrt{0.18 \cdot \lambda^2 \cdot D^{-\frac{1}{3}} \cdot r_0^{-\frac{5}{3}}} - 1 \right| +$$

$$+ \frac{OPL}{c} \cdot \left| \left[\frac{n_1 sin\theta_1}{sin(\theta_1 + \Delta\theta)} \right]^2 - n_1^2 \right| \tag{16.8}$$

where:

$$\Delta\theta = arcos \left[\left(2sin^2 \sqrt{0.18 \cdot \lambda^2 \cdot D^{-\frac{1}{3}} \cdot r_0^{-\frac{5}{3}}} + 1 \right)^{-\frac{1}{2}} \right].$$

We note that this delay time fluctuation depends on the wavelength and on the telescope diameter. In particular, it also depends on the Fried radius, Figure 16.2 shows the trend of this fluctuation as a r_0 function. The simulation is done for La Silla ($\lambda = 0.632 \mu m$, Zenith angle = $10°$).

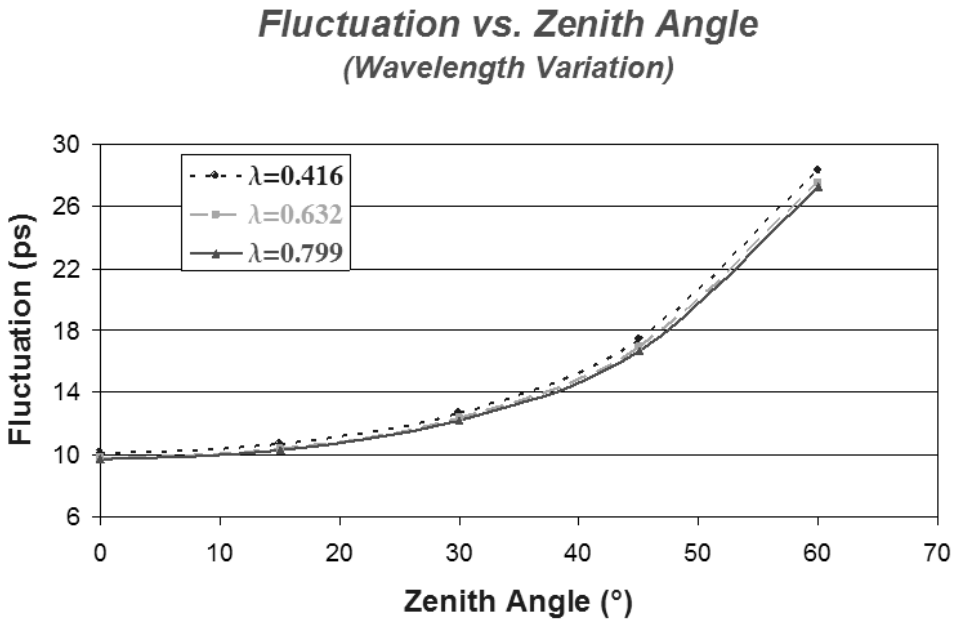

Figure 16.4: Delay time fluctuation as a function of the wavelength and the Zenith angle variation. The simulation pertains to La Silla ($D = 3.58m$, $r_0 = 15cm$).

Table 16.2: Fluctuation vs Zenith angle for different wavelengths, La Silla ($D = 3.58m$, $r_0 = 15cm$).

Zenith Angle	(°)	0	15	30	45	60
$\lambda = 0.416\mu m$	(ps)	10.1	10.7	12.7	17.4	28.3
$\lambda = 0.632\mu m$	(ps)	9.8	10.4	12.4	16.9	27.5
$\lambda = 0.799\mu m$	(ps)	9.7	10.3	12.2	16.7	27.3

16.2 Application of the model to ESO astronomical sites for the delay time fluctuations

In this Section we apply the previously described model to the three Chilean sites of ESO telescopes. We present the results obtained through the Formula 16.8. Table 16.1 shows the simulation results for each site, in particular the fluctuations variation as a function of the telescope diameter. We note that the fluctuation decreases with a larger diameter. In this case, between La Silla and Armazones telescopes the delay time fluctuations decreased of about 40%. Figure 16.3 shows the results of this model for each site as a function of Zenith angle.
Table 16.2 shows the simulation results for three wavelengths. In this case the simulation is done for La Silla. Figure 16.4 shows the Table 16.2 results and Figure 16.5 is the zoom of these trends. In fact, we note that in the range $\lambda = 0.416 - 0.799\mu m$ the fluctuation changes only by 4%.

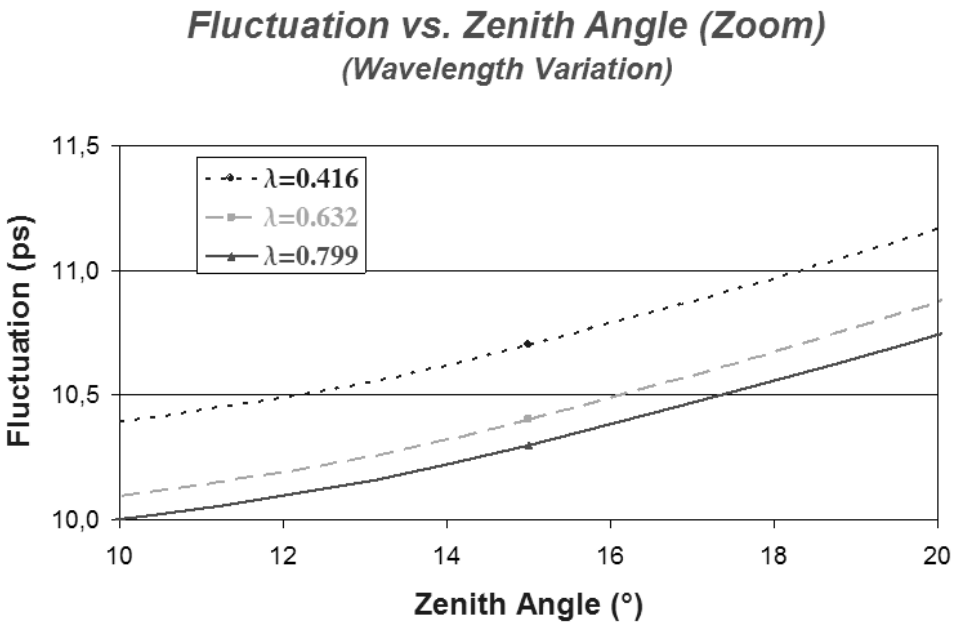

Figure 16.5: Zoom of Figure 16.4.

Chapter 17

Inverting the model to calculate Fried radius

In this chapter, we reverse the Formula 16.8 in order to derive a mathematical expression giving the r_0 value from the study of the delay time fluctuations (see Appendix 17.1). The r_0 value is expressed as a function of the telescope diameter (D), of the wavelength (λ) and of the variable (χ). This variable is obtained through the observation of the delay time fluctuations and the n_1 calculation. The model gives us the following formula for the Fried radius calculation:

$$r_0 = \left| 0.54 \cdot D^{-\frac{1}{5}} \cdot \lambda^{\frac{6}{5}} \cdot arctg^{-\frac{6}{5}}\left(\chi_{1,2}\right) \right| \tag{17.1}$$

where:

$$\chi_{1,2} = \frac{-tg\theta_1 \pm \sqrt{tg^4\theta_1(Z-1) + tg^2\theta_1 \cdot Z}}{Z - tg^2\theta_1}$$

and:

$$Z = \frac{c \cdot \Delta t_F(r_0, D) + n_1^2 \cdot OPL}{n_1^2 \cdot OPL}$$

Through this model we have a new way to calculate the Fried radius as a function of the OPL and average refraction index of the atmosphere. Table 17.1 shows a simulation for La Silla, the mathematical details are given in Section 17.1.

17.1 Reverse mathematical model

We start from Equation 16.8 relating the $\Delta t_F(r_0, D)$ to the Fried parameter r_0:

Table 17.1: Simulation of the r_0 calculation through the delay time fluctuations for La Silla ($\lambda = 0.632\mu m$, telescope diameter $D = 3.58m$).

Delay time fluctuation	Fried radius
$\Delta t_P(r_0, D)$	r_0
ps	cm
27.0	5.0
18.2	10.0
10.2	20.0

$$\Delta t_F(r_0, D) = \frac{n_1^2 \cdot OPL}{c} \left| \sqrt{2} sin \sqrt{0.18 \cdot \lambda^2 \cdot D^{-\frac{1}{3}} \cdot r_0^{-\frac{5}{3}}} - 1 \right| +$$

$$+ \frac{OPL}{c} \cdot \left| \left[\frac{n_1 sin\theta_1}{sin(\theta_1 + \Delta\theta)} \right]^2 - n_1^2 \right|$$

where:

$$\Delta\theta = arcos \left[\left(2sin^2 \sqrt{0.18 \cdot \lambda^2 \cdot D^{-\frac{1}{3}} \cdot r_0^{-\frac{5}{3}}} + 1 \right)^{-\frac{1}{2}} \right] \tag{17.2}$$

In the case of studying the delay time fluctuations for the r_0 calculation, the geometric delay time fluctuation becomes negligible.
Then we consider the formula:

$$\Delta t_F(r_0, D) = \frac{OPL}{c} \cdot \left| \left[\frac{n_1 sin\theta_1}{sin(\theta_1 + \Delta\theta)} \right]^2 - n_1^2 \right| \tag{17.3}$$

we isolate the trigonometric functions:

$$\frac{c \cdot \Delta t_F(r_0, D) + n_1^2 OPL}{n_1^2 OPL} = \frac{sin^2\theta_1}{sin^2(\theta_1 + \Delta\theta)}$$

we substitute:

$$Z = \frac{c \cdot \Delta t_F(r_0, D) + n_1^2 \cdot OPL}{n_1^2 \cdot OPL} \tag{17.4}$$

Using the trigonometric addition formulas and parameters of the *sin* and *cos* functions we get:

$$(Z - tg^2\theta_1)\chi^2 + 2 \cdot Z \cdot tg\theta_1\chi + Z \cdot tg^2\theta_1 - tg^2\theta_1 = 0$$

where:

$$\chi = tg\Delta\theta \tag{17.5}$$

and solving in the same variable we obtain:

$$\chi_{1,2} = \frac{-tg\theta_1 \pm \sqrt{tg^4\theta_1(Z-1) + tg^2\theta_1 \cdot Z}}{Z - tg^2\theta_1}$$

We now consider the equations 17.2 and 17.5 obtaining the following relationship:

$$\Delta\theta = arctg\chi = arcos\left[\left(2sin^2\sqrt{0.18\lambda^2 D^{-\frac{1}{3}} r_0^{-\frac{5}{3}}} + 1\right)^{-\frac{1}{2}}\right] \tag{17.6}$$

Finally, from equation 17.6 we explicitly the r_0 value and we obtain the following formula:

$$r_0 = \left|0.54 \cdot D^{-\frac{1}{5}} \cdot \lambda^{\frac{6}{5}} \cdot arctg^{-\frac{6}{5}}\left(\chi_{1,2}\right)\right|. \tag{17.7}$$

17.2 Discussion of the results

We have shown in this thesis that the delay and dispersion introduced by the terrestrial atmosphere in photon arrival times is significant to the level of tens of nanoseconds and tens of picoseconds respectively.
These values mean a severe degradation of the time tagging performances of modern astronomical detectors such as the Avalanche Photodiode (e.g. Barbieri [2010] and Naletto & Barbieri [2009]). Furthermore, they imply that the very accurate timing signals available e.g. via radio signals by GPS or other Satellite Navigation System are not exploited to their full extent in the astrophysical field, as instead is done in geodetic satellite ranging applications. The scientific results of very high time resolution astrophysics can therefore be degraded by such neglect. In particular, the E-ELT will provide a 25-fold increase of photon flux over existing telescopes thus opening the way to 'quantum' astronomy (e.g. Dravins et al. [2006]). The algorithms expounded in the present thesis overcome these limitations.

In Section 17 we have described a theoretical mathematical model for calculating the Fried radius through the study of delay time fluctuations. Table 17.1 shows the simulation results for La Silla. This is a completely new method for the study of atmospheric turbulence, in future work we want to correlate the delay time fluctuations experimental data with the traditional techniques for the Fried radius calculation. This will allow us a broader view of Earth's atmosphere and its influence on propagation of photons.

Chapter 18

Ground layer Laser Seeing Meter

The seeing calculation and its evolution during the night is a key point for the operation of all new telescopes and adaptive optics systems. Currently there are various instruments able to measure the seeing: for example the DIMM (Differential image motion monitor) and the MASS (Multi Aperture Scintillation Sensor). This thesis describes a new tool for local ground layer seeing measurement.
This has a dual purpose: continuous seeing calculation and a tool able to study the atmosphere in a new way. In particular, we want to derive the Fried parameter r_0 through a laser beam horizontal propagation. This is a new way for the experimental study of low altitude atmospheric turbulence and the physical principles that describe it. Finally, we describe an experiment to be performed at the Asiago Ekar Observatory with its possible applications. The atmospheric turbulence is one of the main limitations of the astronomical observations from the ground. At the moment the physical analysis of this phenomenon is based on the Kolmogorov theory study ([1941]) and its subsequent developments. In astrophysics the study of turbulence is closely related to the phenomena causing perturbations on the incoming wavefronts, generally called "seeing". We now recall one of the main parameters of the astronomical seeing, namely the Fried's radius r_0, which corresponds to the equivalent size of the turbulent cell seen by an optical instrument. It is well known that the astronomical seeing is very often dominated by the turbulence near the ground, mixing layers with a strong thermal gradient. The knowledge of the seeing contribution of these layers is fundamental for the design of modern telescopes and their adaptive optics. It is also important to understand the statistical distribution of the atmospheric parameters, such as the seasonal trends, for the planning of the adaptive optics (AO) systems operations. Up to know there are many studies on the vertical component of the optical turbulence distribution, while

the data on the horizontal distribution are sparse. Masciadri et al. ([2002])) showed the finite size of horizontal turbulence layer. The measurement of the horizontal component is also useful to characterize site hosting telescopes of large area to have continuum monitoring of the layer above the main mirror. The measurement of the horizontal component is also useful to characterize sites hosting large area telescopes through a continuous monitoring of the layers above the main mirror. The instrument described in this thesis is able to obtain r_0, due to the turbulence near the ground through a laser beam propagation. The instrument can be used to obtain a direct measurement of the optical turbulence strength affecting the telescope, to be compared with the r_0 obtained by measuring the temperature gradient fluctuations. The concept of horizontal turbulence is very similar to the vertical turbulence concept. The main physical difference is that the Fried's cell increases its diameter with increasing altitude, while it remains virtually constant along horizontal paths. This makes the instrument highly sensitive to variations of the ground layer. Through the comparison with the seeing calculated by traditional methods, it will be possible to describe a variety of turbulent phenomena, in particular the connexion of the turbulence in the ground layer to the turbulence in the layers at higher altitude. Finally, implementing the instrument with detectors at high temporal resolution we can get useful information even for single photon propagation for both quantum astronomy and new quantum technologies in general. Recent papers have shown that the seeing can be calculated through the photon propagation properties in the atmosphere (see for instance, Cavazzani et al. ([2011])). Knowledge of the temporal behavior of the turbulence can be useful in order to increase the SNR in quantum optical communication (Roberto Corvaja et al. ([2011]) and Ivan Capraro et al. ([2011])).
The main purpose of the instrument remains the physical study of turbulence, in particular the study of seeing.

18.1 Tool description: Laser Seeing Meter

The instrument Laser Seeing Meter (LSM) is conceptually simple. It is formed by two towers with mobile platforms. The height and distance of the towers are indicative for the theoretical description of the instrument. The platforms are aligned with each other: on one a laser transmitter is mounted, and a CCD (Charge Coupled Device) receiver is placed on the other (Fig. 18.1). Two temperature sensors are also mounted on the platforms. This allows the calculation of the Fried's parameter in two different ways. The technological properties are described in detail in the Section 18.9. Finally,

we can equip the instrument with a weather station. This allows us to find any correlation between the seeing and the main weather characteristic. Due to the structural simplicity of the instrument the seeing can be measured in different places of astronomical interest. For example, we can measure the dome-seeing and look for a possible correlation with the ground layer seeing. This study is very useful for the development of new tools for adaptive optics.

18.2 Fried parameter and seeing

Fried has shown (Fried, [1965]), within the limits of validity of the Kolmogoroff law, that r_0 is expressed by the formula:

$$r_0 = \left[0.423 \cdot \frac{4\pi^2}{\lambda^2} \cdot \frac{1}{cos(\theta_{zen})} \int C_n^2 \cdot dz\right]^{-\frac{3}{5}} \tag{18.1}$$

where C_n^2 is the refractive index structure parameter:

$$C_n^2 = \left[80 \cdot 10^{-6} \frac{P}{T^2}\right]^2 \cdot C_T^2$$

where P and T are the atmospheric pressure and temperature, measured in $mBar$ and K. The temperature structure parameter $C_T^2(x)$ is defined through the formula:

$$C_T^2(x) = \frac{\left\langle [T(x) - T(x + \Delta x)]^2 \right\rangle}{\Delta x^{\frac{2}{3}}} \tag{18.2}$$

this parameter is expressed in $(^\circ C)^2 \cdot m^{-\frac{2}{3}}$ and expresses the temperature variations between two locations at a distance Δx. The $\langle\rangle$ indicate an average over time. The seeing produces scintillation, smearing and motion of the image. Roddier (Roddier, [1981]) has obtained the following approximate expressions for the calculation of these three effects. The image scintillation, as a function of C_n^2, in approximation is given by the following formula:

$$\frac{\sigma_I^2}{I} \propto D^{-\frac{7}{3}} \cdot \frac{1}{(cos(\theta_{zen}))^3} \cdot \int C_n^2(z) \cdot z^2 \cdot dz$$

where D is the diameter of the telescope. The motion of the image, as a function of λ, telescope diameter (D) and r_0, is given by:

$$\sigma^2(x) = \sigma^2(y) = 0.18 \cdot \lambda^2 \cdot D^{-\frac{1}{3}} \cdot r_0^{-\frac{5}{3}} \tag{18.3}$$

This motion is in *arcsec*.
The light from the point source is spread over an area having a Full Width Half Maximum (FWHM) given by:

$$FWHM = 0.98\frac{\lambda}{r_0} \tag{18.4}$$

The value is in *arcsec*. The amplitude of this effect for relatively long exposure times is independent of the pupil diameter. We consider the image smearing of a horizontal laser beam to calculate the atmospheric r_0. Then we can calculate the value of the refractive index structure parameter C_n^2.

18.3 Inversion Model to calculate the Fried radius

We recall that the r_0 is an atmospheric integrated measure. In this case it is calculated on the distance between the two instrument's columns. The C_n^2 is then calculated accordingly on the same distance. Through the formula 18.4 we get the radius of the laser spot after the horizontal propagation in the atmosphere:

$$R_{Spot} = d \cdot sin\left(0.98\frac{\lambda}{r_0}\right) \tag{18.5}$$

where d is the distance between the towers. In this case, we assumed a point source. If our laser beam has a diameter D_L the radius of the laser spot after the horizontal propagation in the atmosphere is given by the formula:

$$R_{Spot}(D_L) = d \cdot sin\left(0.98\frac{\lambda}{r_0}\right) + \frac{D_L}{2} \tag{18.6}$$

Reversing the formula 18.6 we get:

$$r_0 = \frac{0.98 \cdot \lambda}{arcsin\left[\frac{R_{Spot}(D_L) - D_L/2}{d}\right]} \tag{18.7}$$

Considering that the r_0 is given by the formula:

$$r_0 = \left[0.423 \cdot \frac{4\pi^2}{\lambda^2} \cdot \frac{1}{cos\phi} \int C_n^2 \cdot dz\right]^{-\frac{3}{5}} \tag{18.8}$$

We can calculate the value of the C_n^2:

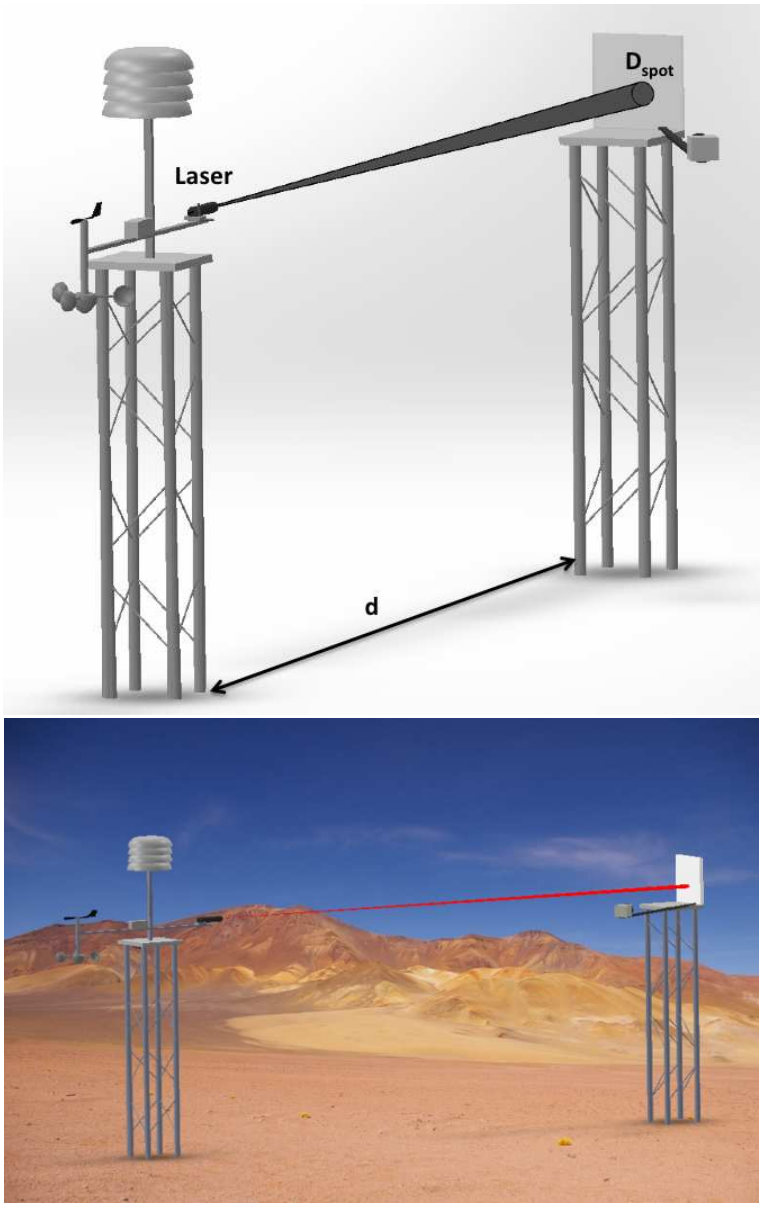

Figure 18.1: The laser seeing meter concept: a laser beam is emitted by the top of $\sim$ 10 m tower toward another platform hosting the detection module. A weather station records the environmental data that are correlated with the beam spot measurement.

$$C_n^2 = 4.73 \cdot \frac{\lambda^2}{4\pi^2} \cdot r_0^{-\frac{5}{3}} \cdot d^{-2} \tag{18.9}$$

We have considered $cos(\phi) = 1$ because we are in a horizontal path.

18.4 Laser beam propagation

Now we have to isolate the contribution due to the propagation characteristics of a laser beam. Any beam propagates in vacuum according to the relation:

$$W(z) = W_0[1 + (z/Z_R)^2]^{1/2} \tag{18.10}$$

where w(z) is the beam radius (to $1/e^2$ of the intensity on axis), W_0 is the beam radius at waist (z=0) and Z_R is the Reyleigh length that defines near and far field respectively when $z < Z_R$ and when $z > Z_R$. The Reyleight range is defined as follows:

$$Z_R = \pi(W_0)^2/\lambda \tag{18.11}$$

and the half angle of divergence of the beam in far field can be obtained from equation 18.10 when $z >> Z_R$ and results $\theta = \lambda/\pi W_0$. The two parameter, λ and W_0 define all the characteristics of the beam.

18.5 Measurement of the Fried radius through the LSM

Considering the Gaussian propagation the equation 18.7 becomes:

$$r_0 = \frac{0.98 \cdot \lambda}{arcsin\left[\frac{R_{Spot}(D_L) - \frac{D_L}{2} \cdot \sqrt{1+\left(\frac{d}{Z_R}\right)^2}}{d}\right]} \tag{18.12}$$

where Z_R is defined by the formula:

$$Z_R = \pi \cdot \frac{(D_L/2)^2}{\lambda}$$

Table 18.1 and Figure 18.2 show the results of a LSM simulation. We calculate the r_0 through the R_{Spot} observation. This simulation is done with the following parameters: transmitter laser diameter $= 1cm$, $d = 200m$ and $d = 50m$, $\lambda = 0.632\mu m$. We note as the r_0 increases with the decrease of the

Table 18.1: Laser seeing meter (LSM) simulation (Transmitter laser diameter = $1cm$, $d = 200m$ and $d = 50m$, $\lambda = 0.632\mu m$). We calculate the Fried radius (r_0) through the laser spot radius (R_{Spot}) observation. We note that if the distance decreases ($d = 200m \rightarrow d = 50m$) also the R_{Spot} variation decreases.

r_0		(cm)	34.77	29.76	24.96	20.10	14.99	10.08	5.00
R_{Spot}	d=200m	(mm)	9.83	9.89	9.97	10.09	10.30	10.71	11.95
R_{Spot}	d=50m	(mm)	5.48	5.49	5.51	5.54	5.60	5.70	6.01

R_{Spot}. We also note as to decrease of the distance (d) between the two towers also decreases the instrument sensitivity. To increase the sensitivity for short distances it is possible to increase the transmitter laser diameter D. Figure 18.3 shows the simulation for two transmitter laser diameter $D = 10cm$ and $D = 5cm$. We note that if we have a larger diameter D it is easier to observe its variations. These trends are related to the theoretical r_0 variation from $5cm$ to $30cm$.

18.6 Calculation of the r_0 through C_T^2

We can calculate the C_T^2 with temperature sensors mounted on the LSM through the equation 18.2. Through the inverse equation 18.2 we can calculate the temperature variation average:

$$\langle [T(x) - T(x + \Delta x)] \rangle = \sqrt{\Delta x^{\frac{2}{3}} \cdot C_T^2(x)}$$

Table 18.2 and Figure 18.4 show the results of a simulation: $d = 200m$, $\lambda = 0.632\mu m$ and $D_L = 1cm$. These values are related to the r_0 variation from $5cm$ to $30cm$. We note that D_L variations of the order of millimeters correspond to variations of the order of $10^{-3}\ ^oC$ degrees. This is an interesting result because it compares for the first time theoretical values of temperature with the induced distortion of a laser beam for fixed r_0 values. Thanks to experimental data of this new type will be possible to understand and explain better turbulent phenomena.

18.7 Fante and Yura Model

If we take into consideration the propagation through a random media such as the turbulent atmosphere we have to modify our model in order to take

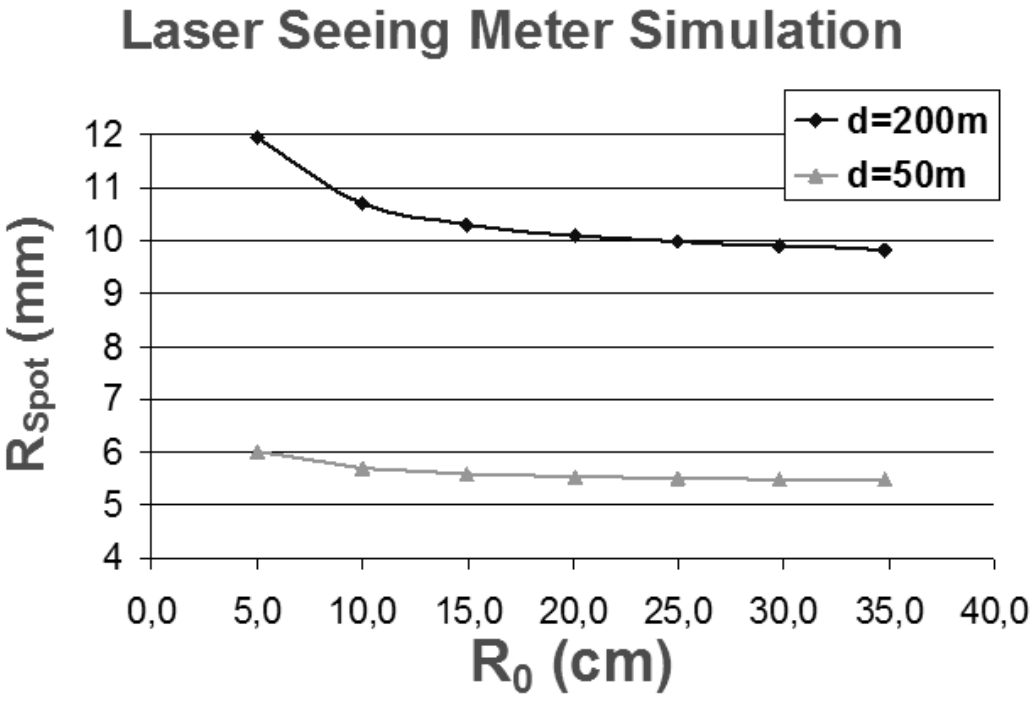

Figure 18.2: Laser seeing meter simulation (Transmitter Laser Diameter = $1cm$, $d = 50m$ and $d = 200m$, $\lambda = 0.632\mu m$). We report the values in Table 18.1. The black line represents the R_{Spot} variation with a distance of $200m$ between the two towers. The gray line represents the R_{Spot} variation with a distance of $50m$ between the two towers. These trends are related to the r_0 variation from $5cm$ to $35cm$.

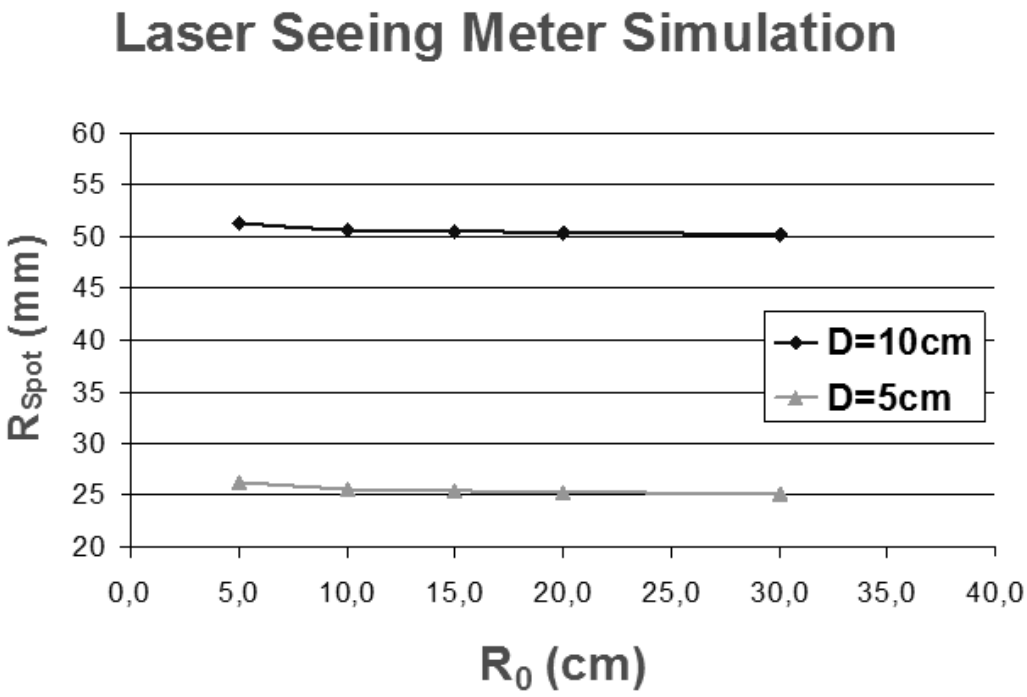

Figure 18.3: Laser seeing meter simulation (Transmitter laser diameter $D = 10cm$ and $D = 5cm$, $d = 100m$, $\lambda = 0.632\mu m$). The black line represents the R_{Spot} variation with a transmitter laser diameter of $10cm$. The gray line represents the R_{Spot} variation with a transmitter laser diameter of $5cm$. These trends are related to the r_0 variation from $5cm$ to $30cm$.

Table 18.2: Comparison between the D_{Spot} variations and ΔT ($^{\circ}mC$) temperature variations: $d = 200m$, $\lambda = 0.632\mu m$ and $D_L = 1cm$. In the first column we have the r_0 fixed values $[cm]$, in the second column we have the D_{Spot} variations $[cm]$ and in the third column we the corresponding ΔT values $[10^{-3} \cdot^{\circ} C]$.

$r_0\ (cm)$	$D_{Spot}\ (cm)$	$\Delta T\ (^{\circ}mC)$
5	2.39	4.5
10	2.14	2.5
10	2.06	1.8
20	2.02	1.4
30	1.98	1.0

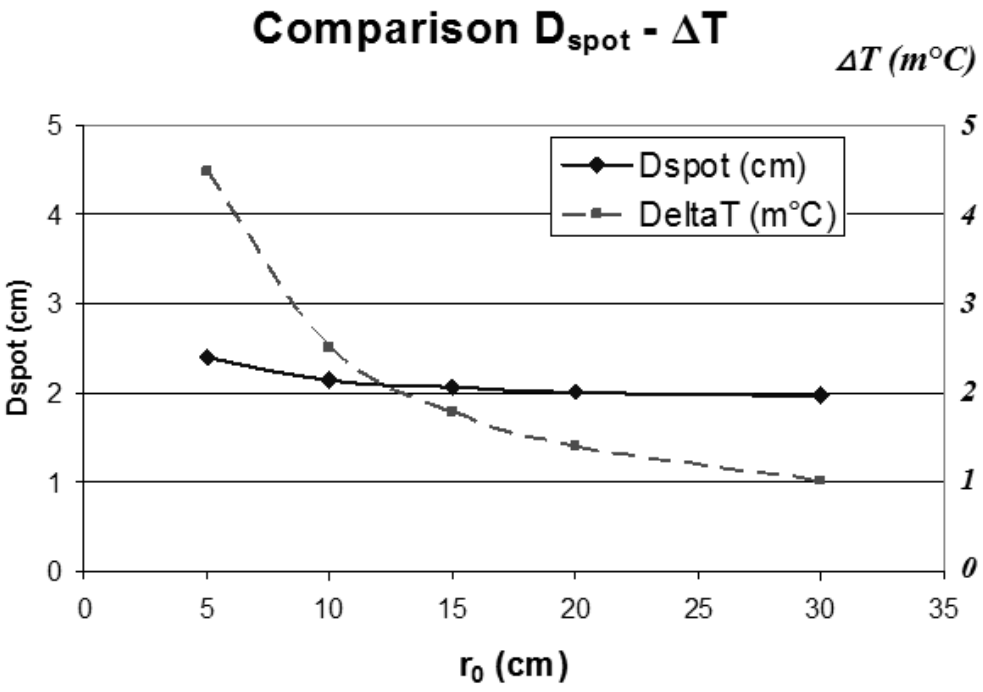

Figure 18.4: Figure shows the trends of the values listed in Table 18.2. The black line represents the D_{Spot} variation (Left axis of ordinates) in function of the r_0. The dashed line represents the ΔT variation (Right axis of ordinates) in function of the r_0.

Table 18.3: Simulation with the three models for different values of the Fried radius: $d = 200m$, $\lambda = 0.632\mu m$ and $D_L = 1cm$.

r_0	(cm)	5	7.5	10	12.5	15	17.5
$R_{Spot}(Fante)$	(mm)	9.74	9.59	9.54	9.52	9.50	9.50
$R_{Spot}(Yura)$	(mm)	9.53	9.49	9.48	9.48	9.47	9.47
$R_{Spot}(Cavazzani)$	(mm)	11.95	11.13	10.71	10.46	10.30	10.18
r_0	(cm)	20	22.5	25	30	35	
$R_{Spot}(Fante)$	(mm)	9.49	9.49	9.48	9.48	9.48	
$R_{Spot}(Yura)$	(mm)	9.47	9.47	9.47	9.47	9.47	
$R_{Spot}(Cavazzani)$	(mm)	10.09	10.02	9.97	9.89	9.83	

this into account. This has been done by Fante ([1975]) and subsequently by Dios et al. ([2004]) where they calculate the long terms (LT) beam radius as a sum of two factors, the normal diffraction one (short term ST) and the one given by the turbulence induced spreading of the beam:

$$W_{LT}^2(z) = W_{ST}^2(z) + 2\langle\beta^2\rangle \tag{18.13}$$

where β^2 is the second order moment of beam displacement. Following the work by Fante this formula yields the following for collimated beams:

$$W_{LT}^2(z=L) = W_0^2\left(1 + \frac{L^2}{Z_R^2}\right) + 2\cdot\left\{\frac{4L}{k_0 r_0}\right\}^2 \tag{18.14}$$

where $k_0 = 2\pi/\lambda$ and r_0 is the Fried coherence length.

Another accepted approximation is related to the work by Yura [1973] for the short-term beam spread:

$$W_{ST}^2 = W_0^2\left(1 + \frac{L^2}{Z_R^2}\right) + 2\left\{\frac{4.2L}{k_0 r_0}\left[1 - 0.26\left(\frac{r_0}{W_0}\right)^{1/3}\right]\right\}^2 \tag{18.15}$$

valid when $0.26(r_0/W_0) \ll 1$.

18.8 Comparison of different models

In this section we compare the models. The calculation of the spot radius is done through the following formulas:

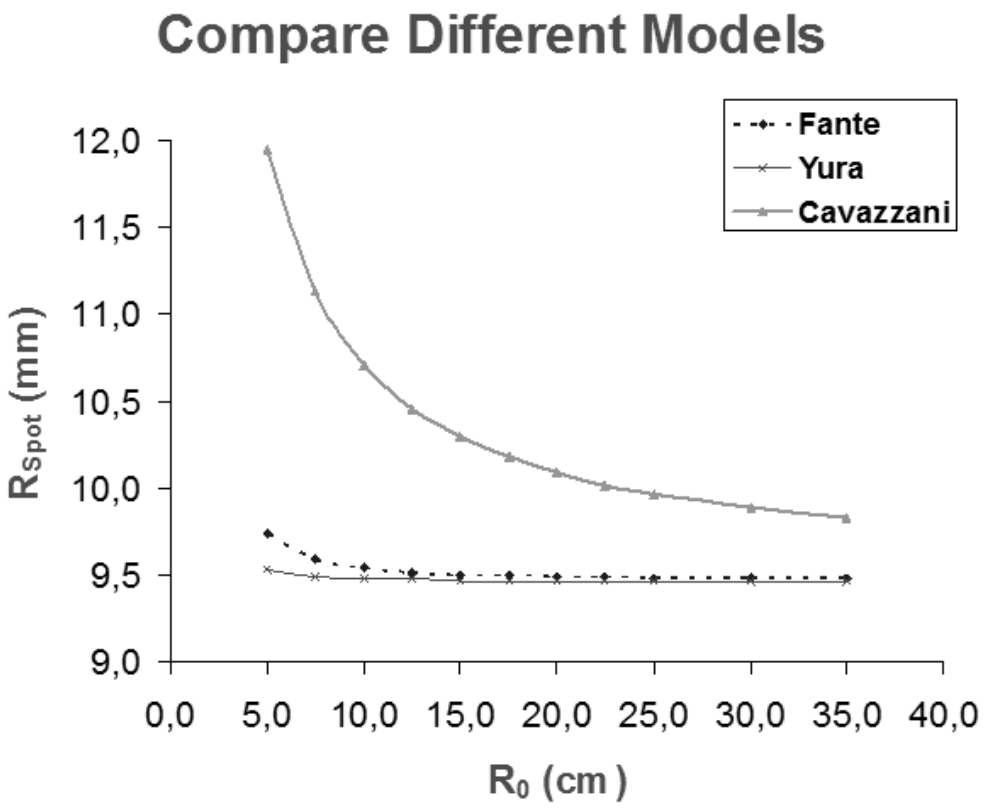

Figure 18.5: Figure shows the trends of the values listed in Table 18.3 ($d = 200m$, $\lambda = 0.632\mu m$ and $D_L = 1cm$). We note that for short distances our model is more sensitive than the Fante's and Yura's models. This difference decreases with the increase of r_0. The gray line with triangles represents the trend of our model, the dashed line with circles represents the trend of Fante model and the black line with crosses represents the trend of Yura model.

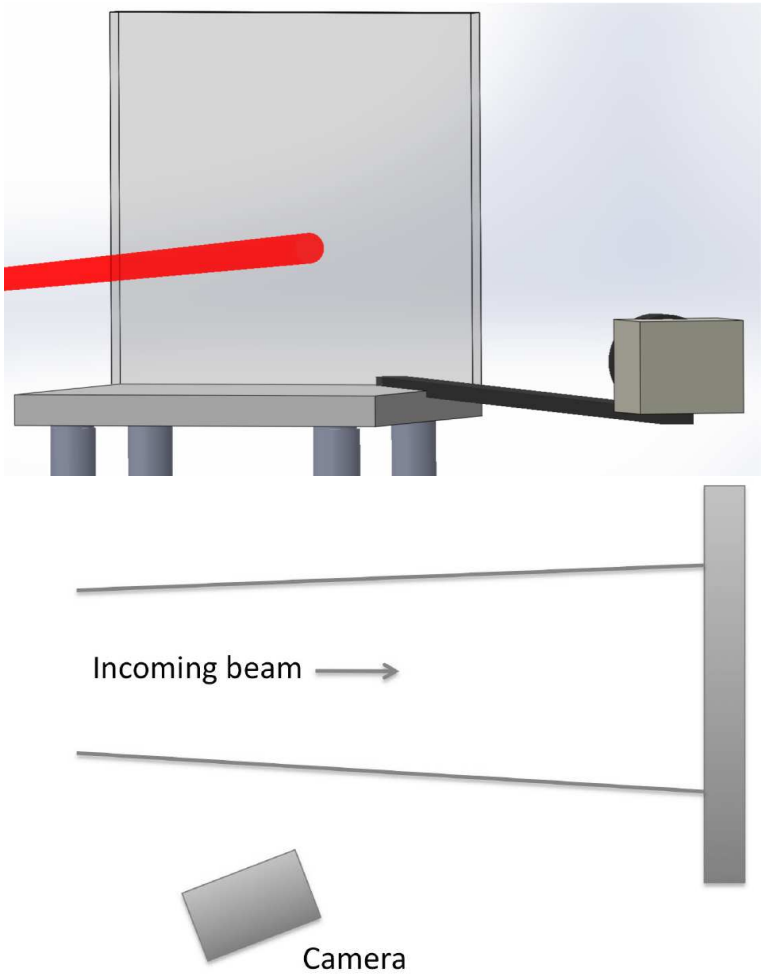

Figure 18.6: LSM detection module with the off-axis camera observing the beam spot on a white screen. A camera is used in order to estimate the beam diameter.

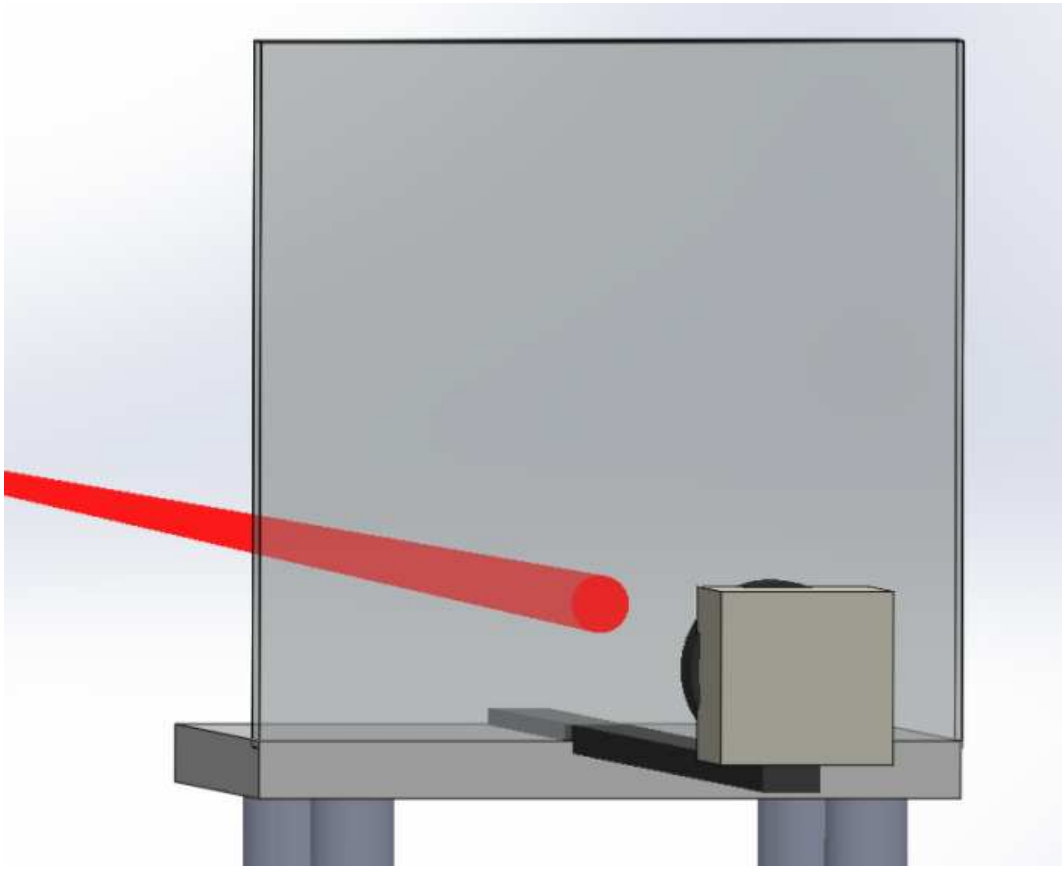

Figure 18.7: Alternative set up with a semi–transparent screen and the on–axis camera observing the transmitted beam spot.

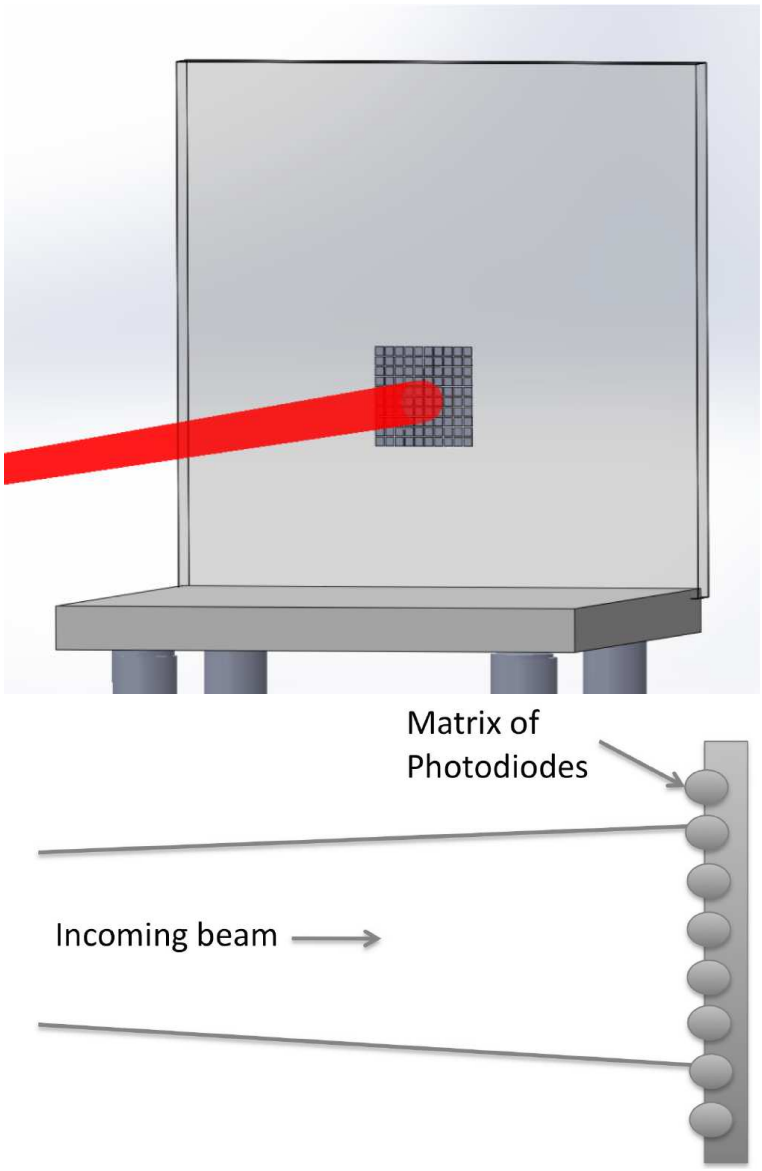

Figure 18.8: LSM detection module equipped with a matrix of photodiodes to detect and sample the impinging laser beam. A matrix of photodiodes is used in order to estimate the beam diameter.

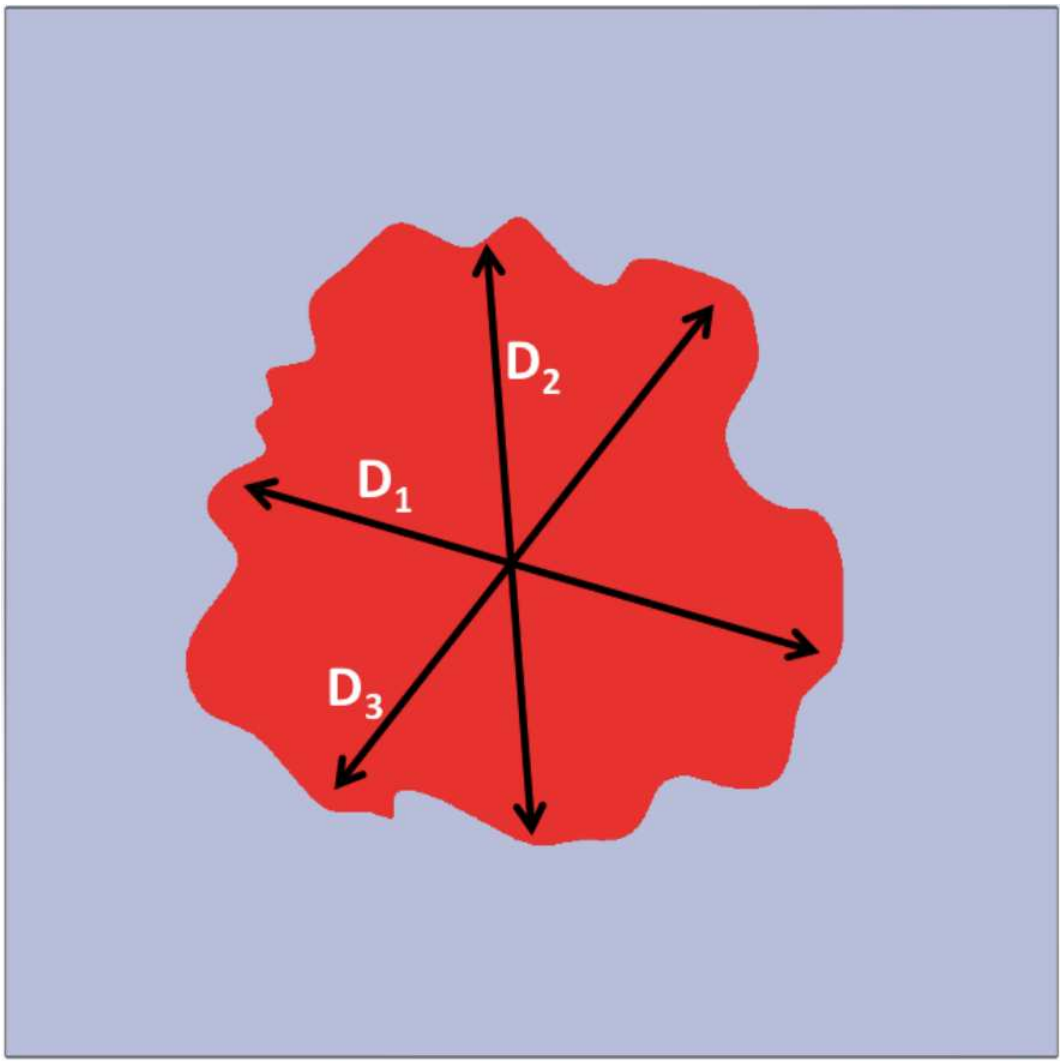

Figure 18.9: The estimation of the beam diameter is based on the average of many spot diameter measurements.

$$R_{Spot}(Fante) = \sqrt{\frac{D_L}{2}^2 \left(1 + \frac{d^2}{Z_R^2}\right) + 2 \cdot \left\{\frac{4d}{k_0 r_0}\right\}^2} \tag{18.16}$$

with the Fante model,

$$R^2_{Spot}(Yura) = \frac{D_L}{2}^2 \left(1 + \frac{d^2}{Z_R^2}\right) +$$

$$+2 \cdot \left\{\frac{4.2 \cdot d}{k_0 r_0}\left[1 - 0.26\left(\frac{r_0}{D_L/2}\right)^{\frac{1}{3}}\right]\right\}^2 \tag{18.17}$$

with the Yura model,

$$R_{Spot}(Cavazzani) = d \cdot sin\left(0.98\frac{\lambda}{r_0}\right) + \frac{D_L}{2} \cdot \sqrt{1 + \left(\frac{d}{Z_R}\right)^2} \tag{18.18}$$

with our model. Table 18.3 and Figure 18.5 show the values of a simulation with the three models for different values of the Fried radius: $d = 200m$, $\lambda = 0.632\mu m$ and $D_L = 1cm$. We note that the model described in this article is much more sensitive than the other models. One possible explanation is that the two previous models are optimized for long distances (of the order of several Kilometers). Our model is extremely sensitive over short distances (e.g. $d = 200m$) and shows a significant difference compared to the Fante's and Yura's models. This difference decreases with the increase of r_0. This important result gives to the instrument a good theoretical sensitivity to the ground layer r_0 variations.

18.9 Detection of Beam Diameter

In a setup where a laser is about 300 m away from a target, one can think several possible way to detect its diameter. Since the system is designed in order to obtain a spot diameter of the order of 3-to 20 cm, it is possible to place a white screen and a calibrated camera in order to get an estimate of the beam diameter as shown in Figure 18.6. The camera can be a standard USB camera, with a frame rate of 30fps and standard exposure times since the laser used can provide enough power on such short distance. The calibration procedure is intended to i) avoid the tridimensional distortion due to the camera position; ii) get the precise scale of the image and iii) get rid of unwanted noise. Based on the exposure time used it is possible to measure

the long exposure diameter or the short time diameter so appreciating also the beam wander effect. The beam diameter is estimated as average of the diameter along each axes centered on the spot centroid (see Section 18.10 and Formula 18.19). The precision of this method can yield results with 0.1 mm precision or more if more statistic is collected.
The advantage of using a camera is the possibility of binning the detector, allowing different spatial sampling and fast exposures. A similar realization, that allows to remove the problem of spot projection is easily implemented by using a tiny smeared out thin glass instead of the white screen. The camera is positioned along the laser beam axis beyond the glass and it observes the transmitted beam spot, see Figure 18.7. Another solution that gives a greater sensitivity is the use of a matrix of photodiodes placed directly on the receiving screen as shown in Figure 18.8. In this way the beam profile could be recovered from the signal of the photodiodes. The acquisition electronic is a little more complicated depending on the desired sampling frequency, but the photodiodes are almost completely free from read–out–noise. The beam diameter is calculated by fitting a gaussian profile on the beam spot retrieved by the photodiodes. The precision is comparable to the previous method as long as the beam that strikes the detectors is truly gaussian. This approach, in addition, would eliminate the projection effect suffered by the previous methods. The main drawback of the photodiodes array is the fix plate scale, that once the photodiodes dimensions are chosen, it can't be changed without the use of optical components in the laser path. This however should be avoided because, especially for large beam spot diameters, the optical components would introduce aberrations and absorption. In terms of costs this solution is more expensive than the set up equipped with a commercial USB camera.

18.10 Measurement of the laser beam diameter

Figure 18.9 shows a schematic example of the beam distortion caused by atmospheric turbulence. In addition to the shape distortion we will also have a phenomenon of scintillation but, for the theoretical model described in this thesis, this phenomenon is irrelevant: the r_0 measurement occurs through the average diameter calculation of the surface on the screen. According to the theory of turbulence the atmosphere keeps constant conditions for about sixty seconds. With this assumption, for the turbulence study, it will be sufficient to have surface measures integrated on the order of seconds, while for quantum applications higher temporal resolutions are needed. We then consider the mean surface of the spot A, the D_{Spot} is calculated using the

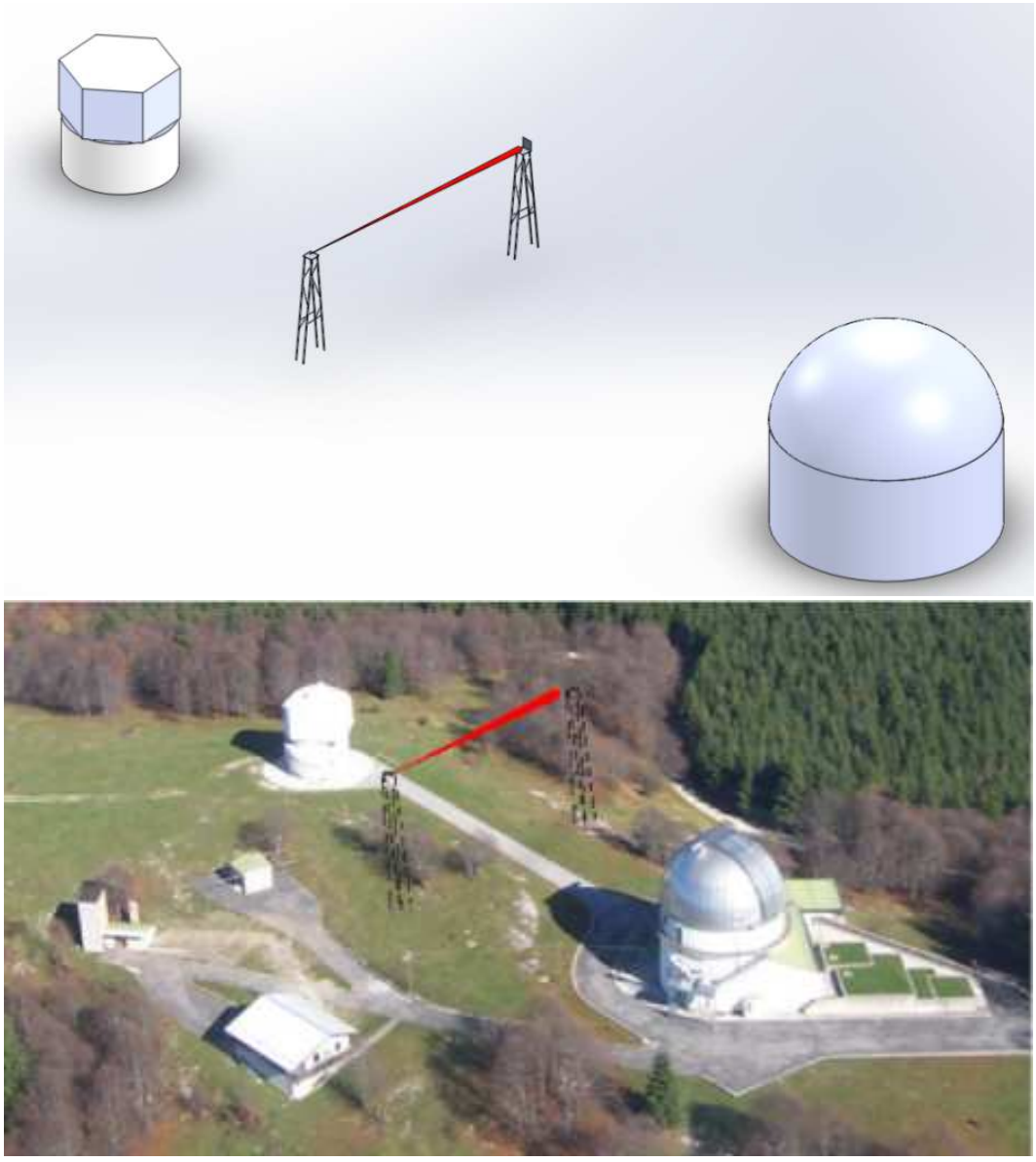

Figure 18.10: Top: conceptual laser seeing meter set up between the Schmidt 67/92 and 182 cm Copernico domes. How it should look like once realized (bottom).

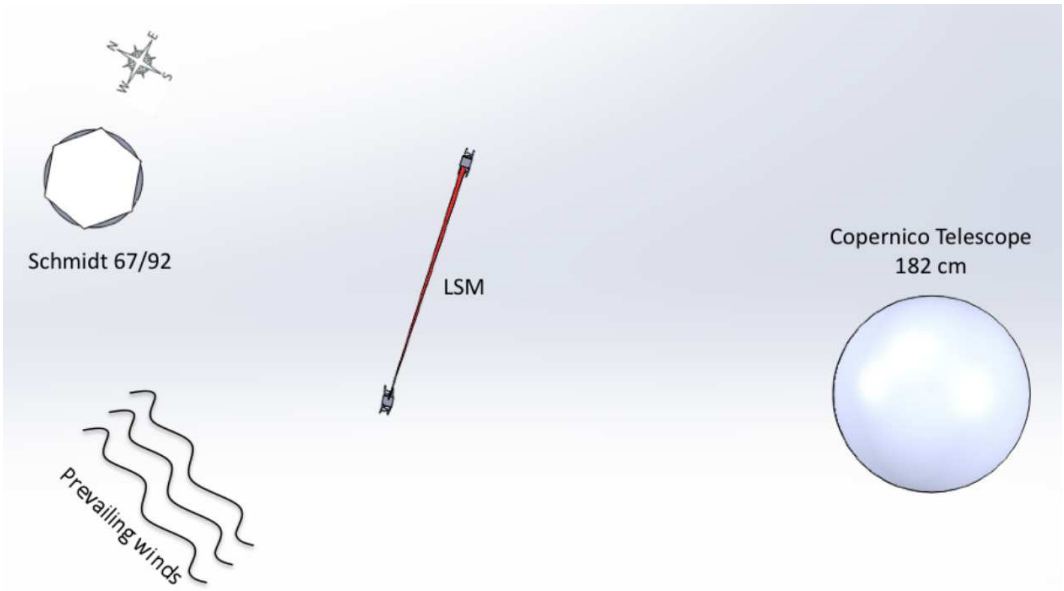

Figure 18.11: Top view of laser seeing meter; the laser beam propagates between the two domes approximately along the East–West direction.

formula:

$$D_{Spot} = 2 \cdot \sqrt{\frac{A}{\pi}} \tag{18.19}$$

The obtained D_{Spot} will be used for the r_0 calculation.

Chapter 19

A Pilot Experiment

With reference to the above presented LSM concept we propose a pilot and cost–effective experiment that could be carried out at the Asiago Ekar Observatory, Longitude $11°34'08.42''E$ – Latitude $45°50'54.5''N$ – Altitude 1366 m, to verify the likelihood of the model introduced in the previous sections. A prototype of the LSM would be installed at Mount Ekar between the Schmidt 67/92 and the 182 cm Copernico telescope domes along the East–West direction. The towers, hosting the transmitter (laser) and the receiver (detector), should be about 10 meters high, in order to sound the portion of the atmosphere's ground layer around the domes. The flat plateau at the top of Mount Ekar in E–W direction is about 30 meters and limits the distance among the two towers to this upper value (see Figure 18.10). The separation can be extended if we accept to increase the altitude of one of the two towers, but since the proposed model is sensitive over short distances, this range seems to be adequate to give rise detectable effects. The height of the two towers prevents the laser beam from crossing spaces where the Observatory personnel operates and it doesn't interfere with the observations of the two telescopes. The orientation of the LSM corresponds approximately to the direction of the prevailing winds (see Figure 18.11). The installation of the LSM at Mount Ekar Observatory would ensure an easy and constant accessibility to the experimental set up for observations and maintenance of the whole system. There is also an interesting consequence in installing the LSM close to an astronomical observatory; the control software of the Schmidt and Copernico telescopes for system tracking and image acquisition performs an estimation of the PSF FWHM at rate of 1 Hz. This continuative PSF sampling could be recorded in a serendipity modality during the nights of parallel astronomical observations and LSM operations. An off–line data analysis of the FWHM of the stars retrieved by the control software of the telescopes, would allow a cross–correlation with the LSM FWHM measure-

ments. In principle, this cross–correlation leads to a comparison between the turbulence regime that develops along the horizontal direction with that orthogonal propagating upward toward the sky. Even if the stars FWHM acquisition is subjected to the scheduled observing program with variable elevations depending on the observed object, the correlation is equally important and meaningfull since it sounds a portion of the atmosphere rather different from that explored by the LSM. In addition, the observatory has a weather station equipped with an all sky camera[1]. These data provide a comprehensive study of turbulence and how this is related to all weather phenomena.

19.1 Conclusion

In this thesis, we have described a new tool for the r_0 calculation for the near ground layers through the propagation of a horizontal laser beam. The instrument is also equipped with high-resolution temperature sensors. This allows in theory a comparison between the two values: the r_0 measured with our model and the r_0 calculated radius with the C_T^2 (see Section 18.5). The value calculated through the temperature gradient is based on discrete data and a theoretical model while the calculated value with the laser is based on continuous data and requires more limited assumptions. This allows a greater sensitivity to fluctuations and lead to a new study of atmospheric turbulence. The platforms are mobile and this allows a laser tomography of the low atmosphere. The thesis also compares two models currently used to study the propagation of a laser beam to our model. Theoretically, our model is more sensitive over short distances, this of course remains to be experimentally tested (see Section 18.8). Finally we propose a LSM prototype to be installed at the Asiago Ekar Observatory in order to test the proposed model (see Section 19). A weather station will allow to study the correlations of the seeing effects with the major atmospheric phenomena: in particular wind and humidity. We plan to improve this model using satellite data. We could compare the data obtained with the LSM beam with satellite data, in particular the seeing values (see for instance, Cavazzani et al. ([2011])). This is a crucial step for the new site testing methodologies. Furthermore this can be very helpful for sky observations as well as for free space communication, in particular for quantum communication where the knowledge of the atmospheric condition can yield to an improvement of the SNR either by postselection of the events that come when there is lower turbulence or by

[1] http://sirius.bu.edu/data/Asiago

using the single detector gate function to prevent the detector to open when turbulence is strong.

Chapter 20

ACKNOWLEDGMENTS

The authors acknowledge dr.Vincenzo Testa, from National Institute for Astrophysics, Roland Gredel, from Heidelberg Max Planck Institute for Astronomy, Antonia M. Varela, from Instituto de Astrofisica de Canarias, Antonio Magazzu from TNG and the former TNG Director Ernesto Oliva for the collaboration.
This activity is supported by the European Community (Framework Programme 7, Preparing for the construction of the European Extremely Large Telescope, Grant Agreement Number 211257) and by Strategic University of Padova funding by title "QUANTUM FUTURE".
Most of data of this thesis are based on the CLASS (Comprehensive Large Array-data Stewardship System).
CLASS is an electronic library of NOAA environmental data.
This web site provides capabilities for finding and obtaining those data, particularly NOAA's Geostationary Operational Environmental Satellite data.
Finally we acknowledge the Liverpool Telescope website staff. Thanks are due to Prof. D. Dravins for useful discussions.

Bibliography

[2007] Acker, J. G. and G. Leptoukh, 2007, Eos Trans. AGU, 88, p.14.

[2010] Barbieri C., Verroi E., Zoccarato P., Germanà C., Naletto G.P, Occhipinti T., Capraro I., Barbieri M., Zampieri L., Gradari S., 2010, Results of Iqueye, A single photon counting very high speed photometer at the ESO 3.5m NTT in 2009. HTRA IV - The Era of Large Telescopes. 5-7 May 2010.

[2011] Capraro, I., Tomaello, A., Dall'Arche, A., and Villoresi, P., 2011, Proc. SPIE 8161, 81610C.

[2011] Cavazzani, S.,Ortolani, S., and Barbieri ,C. 2011, MNRAS, 411, 1271.

[2010] Cavazzani, S., Ortolani, S., Zitelli, V., Maruccia,Y. 2010, MNRAS, 411, 1271

[2011] Cavazzani,S.,Ortolani, S., and Zitelli,V., Maruccia,Y., 2011, MNRAS, 411, 1271.

[1996] Ciddor P. E., 1996, Applied Optics, Vol. 35, Issue 9, pp. 1566-1573.

[2011] Corvaja Roberto et al., Engineering a Long Distance Free-Space Quantum Channel, ACM New York, NY, USA, 2011.

[2011] Dee et al., 2011, Q. J. R. Meteorol Soc., 137, p.553

[2010] Della Valle,A., Maruccia,Y., Ortolani, S., and Zitelli,V., 2010, MNRAS, 401,1904 (Paper III)

[2004] Dios, F., Rubio, J. A., Rodriiguez, A., et al. Scintillation and beam-wander analysis in an optical ground station-satellite uplink. Appl. Opt. 43, (19), 3866-3873.

[2006] Dravins D., Barbieri C., Fosbury R. A. E., Naletto G., Nilsson R., Occhipinti T., Tamburini F., Uthas H., Zampieri L., 2006, Astronomical Quantum Optics with Extremely Large Telescopes, in P.Whitelock, B.Leibundgut, M.Dennefeld, eds. "The Scientific Requirements for Extremely Large Telescopes", IAU Symposium 232, Cambridge University Press, pp.502-505.

[2006] Erasmus,D., van Rooyen,R., 2006, in Stepp, L.M. Ed., Proc. of SPIE Vol. 6267, Ground-based and Airborne Telescopes.

[2002] Erasmus,D., Sarazin,M., 2002, in Vernin J., Benkhaldoun Z., Munoa-Tunon C., eds. Asp Conf.Series, vol.266, p.310.

[2001] Erasmus,D.,& Maartens D., 2001, Final Report to ESO 2001(58311/ODG/99/8362/GWI/LET; garching ESO)

[1975] Fante, R. L., Electromagnetic beam propagation in turbulent media, Proc. IEEE 63, 1669-1692.

[1965] Fried D. L., 1965, Statistics of a Geometric Representation of Wavefront Distortion. Optical Society of America Journal, 55, 1427-1435.

[1983] Frieden B. R., 1983, Unified theory for estimating frequency-of-occurrence laws and optical objects, J. Opt. Soc. Am. 73, 927-938.

[2010] Garcia-Gil, A., Muñoz-Tuñón, C., Varela, A.M., 2010, PASP 122, 1109-1121, Atmosphere Extinction at the ORM on La Palma: A 20 yr Statistical Database Gathered at the Carlsberg Meridian Telescope.

[2005] Graham, E., Sarazin, M., Beniston, M., Collet, C., Hayoz, M., Neun, M. and P. Casals, 2005, Meteorological Applications, 12, pp 77-81.

[2008] Graham,E., Sarazin,M., Kurlandczyk,H., Neun,M., Mätzler,C., ,2008, Proceedings of the SPIE, 7012 (69), 10pp.

[1941] Kolmogorov A. N., 1941, The local structure of turbulence in incompressible viscous fluid for very large Reynolds numbers. Proceedings of the USSR Academy of Sciences 30: 299Ű303.

[2005] Kral L., Prochazka I., and Haman K., 2005, Optics Letters, Vol. 30, 1767-1769.

[2007] Kurlandczyk, H., and Sarazin,M., 2007, proc. of SPIE vol.6745, Remote Sensing of Clouds and the Atmosphere.

[2006] Lombardi,G.,Zitelli,V., Ortolani,S., Pedani,M J., 2006, PASP, 118,1198 (Paper I)

[2007] Lombardi,G., Zitelli,V., Ortolani,S., Pedani,M., 2007, PASP, 119, 292 (Paper II)

[1973] Marini J. W. and C. W. Murray, 1973, NASA Report X-591-73-35.

[2002] Masciadri, E., Avila, R., Sánchez, L. J. Astronomy and Astrophysics, v.382, p.378-388 (2002)

[1985] Murdin,P., 1985, Vista Astron.,28,449

[2009] Naletto G.P., Barbieri C., Occhipinti T., Capraro I., Di Pola A., Facchinetti C., Verroi E., Zoccarato P., Anzolin G., Belluso M., and 13 coauthors, 2009, Iqueye, a single photon-counting photometer applied to the ESO new technology telescope, Astronomy and Astrophysics, Volume 508, Issue 1, 2009, pp.531-539.

[1984] Osmer, P.S., Woos,H.J., 1984, ESOC. 18, 950

[2001] Riepl S., 2001, Report on activities of the Refraction Study Group, Bundesamt für Kartographie und Geodäsie, Germany.

[1981] Roddier F., 1981, The effects of atmospheric turbulence in optical astronomy, Pages 281-376 of: Progress in optics. Volume 19. Amsterdam, North-Holland Publishing Co.

[2008] Rovero A.C., Romero G.E., Allekotte I., Beton X., Colombo E., Etchegoyen A., Garciaa B., Garcia-Lambas D., Levato H., Medina M.C., Muriel H. and Recabarren P., 2008, arXiv 0810.0628v1.

[2010] Sanroma, E., Palle, E., Sanchez-Lorenzo, A., 2010, Environ. Res. Lett. 5 1-6

[2004] Sarazin, M., 2004, The VLT Astronomical Site Monitor (www.eso.org/gen-fac/pubs/astclim/paranal/asm/verif/20years-ClimatologyofParanal-Oct2004.pdf)

[2006] Sarazin, M., Graham, E. and Kurlandczyk, H., 2006, The Messenger, 125, pp 44-47.

[1990] Sarazin, M., Roddier, F., 1990, A&A, 227, 294-300

[2007] Tapia, M., Hiriart, D., Richer, M., and Cruz-Gonzalez, I., 2007, RevMexAA (Series Conf.), 31, 47.

[1992] Tapia, M., 1992, RevMexAA, 24, 179-186.

[2008] Varela, A.M., Bertolin, C., Munoz-Tunon, C., Ortolani, S., and Fuensalida, J.,J., 2008, MNRAS, 391, 507-520.

[2011] Wijaya D., Brunner F., 2011, Journal of Geodesy, Atmospheric range correction for two-frequency SLR measurements, pp. 1-13, doi:10.1007/s00190-011-0469-8.

[1973] Yura, H. T., Short-term average optical-beam spread in a turbulent medium, J. Opt. Soc. Am. 63, 567D57.